Investigation of CeO2 doped with multi-valent cations for mixed ionic and electronic conducting solid oxide fuel cell electrodes

趙, 亮

https://doi.org/10.15017/1500729

出版情報：九州大学, 2014, 博士（工学）, 課程博士
バージョン：

固体酸化物形燃料電池用の多価元素添加セリア系の混合導電性電極材料に関する研究

Investigation of CeO_2 doped with multi-valent cations for mixed ionic and electronic conducting solid oxide fuel cell electrodes

博士論文

九州大学大学院工学府

水素エネルギーシステム専攻

趙　亮

Abstract

Solid oxide fuel cells (SOFCs) have been attracting great attention because they promise to provide clean, environmentally compatible power generation by directly converting chemical energy into electrical energy with high energy conversion efficiency and high fuel flexibility. One of the key challenges to commercialization of SOFCs is to lower their operating temperature. However, reducing the operating temperature decreases the conductivity of the electrolyte and the electrode kinetics resulting in large ohmic and polarization resistances. By using thin film electrolytes, the ohmic resistance can be reduced significantly. In this case, the overall cell performance is determined by the polarization losses of the electrochemical reactions at anodes and cathodes, and the key technical challenge is finding methods to minimize electrode polarization losses at lower operating temperatures. By using mixed ionic electronic conductors (MIECs), the polarization resistance of the electrode materials can be decreased. In this work, the electrical properties of Mn, Fe or Eu doped ceria were investigated for application as mixed ionic and electronic conducting solid oxide fuel cell electrodes. Additionally, the long-term durability of electrode performance is as important as initial performance, and impurities in the operating environment (e.g. in feed gases or in the cell materials) are well known to contribute to long-term degradation. Therefore, the long term durability of oxygen exchange rate of Pr-CeO_2, a potential MIEC SOFC cathode, was investigated.

This thesis is divided into seven chapters:

Chapter 1 reviews the principles of SOFC operation and current status of materials. Defect equilibrium diagrams of pure and doped ceria are discussed. Techniques for studying defect equilibria and transport, the key challenges for SOFC materials, and approach in this thesis are introduced.

Chapter 2 describes the experimental techniques used in this work, including sample preparation method and material characterization techniques (i.e. SEM, XRD, Raman spectroscopy, XPS, electrochemical measurement methods, thermogravimetric Analysis (TGA), and optical transmission relaxation (OTR) measurements).

In Chapter 3, the electrical conductivity of 20 mol% Eu-doped ceria ($Ce_{0.8}Eu_{0.2}O_{2-\delta}$), measured by impedance spectroscopy, is reported. 20 mol% Eu-doped ceria showed similar conductivity behavior in reducing and oxidizing conditions as Gd-doped ceria, previously reported in the literature. No evidence for multivalency of Eu was observed in electrical conductivity measurements over the studied range. Either the electron mobility of Eu small polarons is too low or Eu is not displaying multivalency in the studied range.

In Chapter 4, x mol% Mn-CeO_2 and x mol% Fe-CeO_2 (x=3-50) powders were synthesized and characterized by XRD and Raman. Raman spectroscopy and lattice parameter analysis revealed that the solubility limit of Mn or Fe in CeO_2 is lower than 3 mol% for the present preparation conditions. The solubility of Mn was increased by co-doping La into Mn-CeO_2. Based on assumptions from the change of lattice parameter, for 10 mol% Mn-CeO_2, the Mn solubility was increased to 2.9 mol% with 10 mol% La dopant. Conductivity of 20 mol%-CeO_2 was measured by impedance spectroscopy and showed a pure ceria like pO_2 dependence at higher temperature and an acceptor doped ceria like one at lower temperature. Additionally, it agreement of reduction enthalpy derived from conductivity was found with undoped ceria. The activation energy calculated from an Arrhenius plot of conductivity is 1.1 eV. Comparing this activation energy with other acceptor doped compositions, the Mn solubility was estimated to be about 0.1~1 mol% in agreement with the low solubility observed by XRD and Raman results.

In Chapter 5, oxygen exchange kinetics of Pr-CeO_2 (PCO), measured by optical transmission relaxation (OTR), are reported. A significant degradation in kinetics was found after aging at high temperature for tens of hours, and identified to arise from accumulation of a siliceous phase on the PCO film surface. Deposition of La oxide or Sm oxide on the aged film surface was found to fully recover oxygen exchange kinetics in aged films and a film intentionally coated with siliceous phase. Surface treatments with other oxides (Nb, Al, Ti, and Zn) were not found to recover oxygen exchange kinetics. La and Sm likely react with Si to form a porous silicate layer allowing gas transfer to the PCO surface, whereas other studied materials are unlikely to form silicates. La oxide was also deposited on aged $SrTi_{0.65}Fe_{0.35}O_{3-\delta}$, prone to degradation via Sr segregation (as opposed to siliceous phases), and no improvement was found, further indicating La reacts with Si and is not leading to a significant catalytic effect.

Chapter 6 and 7 summarize the conclusions and suggested future topics to be investigated.

Contents

List of Figures

Chapter 1 Introduction

1.1 Solid oxide fuel cell

Fuel cells, devices which convert chemical energy to electrical energy with a higher efficiency than heat based power generators, are considered to be a promising technology. The solid oxide fuel cell (SOFC) is an all solid-state device that converts the chemical energy of gaseous fuels such as hydrogen and natural gas to electricity through electrochemical processes. SOFC, being an electrochemical device, has unique advantages over the traditional power generation technologies. The efficiency of SOFC is inherently high as it is not limited by the Carnot cycle of a heat engine. The greenhouse gas emissions per kilowatt-hour from an SOFC are therefore much lower than those emitted from conventional power plants. Due to the high operating temperature, SOFCs can be used in co-generation systems to produce hot water or steam and to couple with microturbines or gas turbines to produce electrical power, both of which enhance the system efficiency and the range of applications. The momentum of the intensive research and development of SOFC technology started in the middle seventies with the Westinghouse (later, Siemens-Westinghouse) tubular SOFC development program (*1*). Minh, over two decades ago in 1993, gave a comprehensive overview on the whole spectra of the SOFC technologies (*2*). Key advantages of SOFC technology are summarized in the following list.

- Fuel flexibility
- Use of non-precious metal catalysts
- Coupling with high quality waste heat for cogeneration applications
- Solid structure (electrolyte) prevents the electrolyte from being volatilized resulting in high reliability and durability
- High efficiency and power density relative to other energy technologies
- High operating temperature allows for direct internal processing of fuel without the use of reformer resulting in a less complicated system. Ability to combine with cogeneration schemes using the generated waste heat in which the efficiency could be increased from 50-60% up to 90%

The operating temperature for a conventional SOFC is 800~1000 °C, however this high temperature results in high cost, high degradation rates and long start-up and shut-down times. In order to achieve a long service life, as well as shorter start-up and shut-down time, the operating temperature should be decreased. SOFCs operating at around 700 °C are called intermediate temperature SOFCs (ITSOFCs), and at less than 600 °C are called low temperature SOFCs (LTSOFCs). The challenges for ITSOFCs and LTSOFCs are discussed at the end of this chapter.

The schematic diagram of solid oxide fuel cell system is shown in Fig. 1.1. At the cathode, oxygen diffuses to the electrode surface, is then reduced into an oxide ion that moves to the anode through the solid electrolyte. Meanwhile, at the anode, hydrogen or hydrocarbon fuel reacts with the oxide

ions that cross over the electrolyte/anode interface. The products from this reaction are water and electrons. Water is driven out as exhaust gas whereas electrons are driven through the external circuit loop generating electricity.

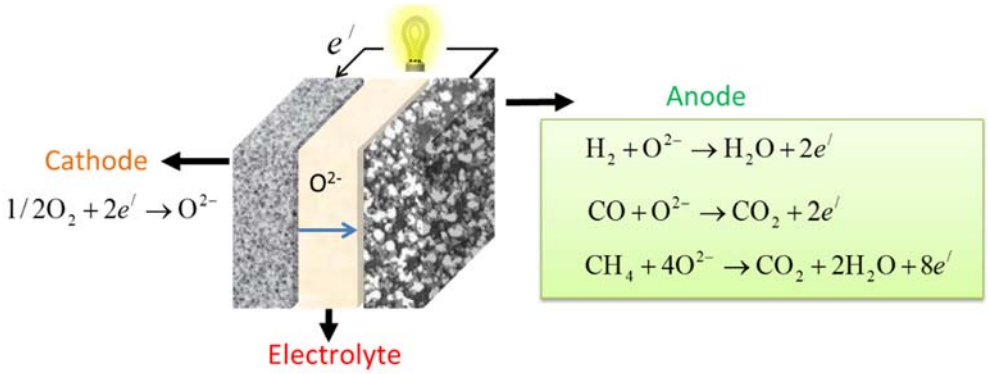

Figure 1-1 Schematic diagram of a solid oxide fuel cell

The ideal fuel cell open circuit performance can be theoretically calculated using the following Nernst equation (*3*).

$$E_0 = \left(\frac{RT}{4F}\right)\ln\left(\frac{p_{O2,c}}{p_{O2,a}}\right) \qquad 1\text{-}1$$

where $p_{O2,c}$ and $p_{O2,a}$ refer to the oxygen partial pressures in the cathode air and anode fuel electrodes, respectively. This implies that the theoretical electromotive force is dependent on the difference between the oxygen partial pressures at the two electrodes and temperature. Actual cell performance is affected by losses from various electrochemical processes, as demonstrated by Equation 1-2

$$V = E_0 - IR - \eta_{cathode} - \eta_{anode} \qquad 1\text{-}2$$

where E_0 is the Nernst potential of the reactants, I is the current, R is the ohmic resistance and $\eta_{cathode}$ and η_{anode} are the cathodic and anodic polarization losses.

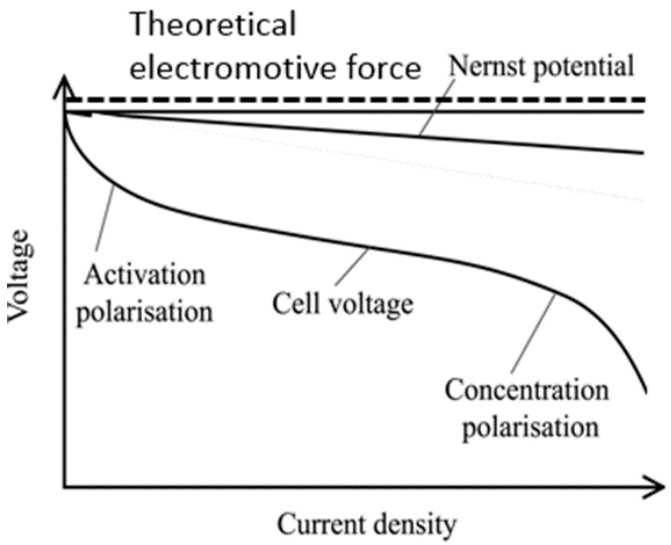

Figure 1-2 Typical voltage versus current density curve for an SOFC (*3*).

As shown in Figure **1-2** the voltage loss can be broken down into various resistances caused by activation polarization, ohmic polarization and concentration polarization. The characteristics of each polarization are described as follows:

Activation polarization: dominates at low current density region. It is the voltage loss accounting for the activation required for charge transfer during reactions incurring at the electrodes. The dominant reaction rate is of cathodic reaction which is, at very low current densities, linearly proportional to the net current density. Activation polarization includes both the anodic and cathodic reactions and the reaction may dominate by the reaction rate or the electron/ion transfer. It is usually considered that the activation polarization on the cathode is much higher than the one on the anode. Because the cathode needs to dissociate the oxygen molecules to ad atoms and then oxygen ions and transport the oxygen ion, simultaneously. Activation polarization can be reduced by: (a) using material with higher catalytic activity, (b) Modifying the microstructure (increasing the triple phase boundary (TPB)), increasing the concentration of active sites, (c) increasing the concentration and pressure of reactant, and (d) increasing the temperature. Therefore, due to their lower operation temperature, activation polarization is one of the most important voltage losses for intermediate temperature SOFC (IT-SOFC).

Ohmic polarization: accounts for the resistance to the motion of electrical charge which can be described by Ohm's law. It is the product of current (I) and the sum of ohmic resistance as expressed in the following equation.

$$\eta_{ohm} = I(R_{el} + R_i + R_c) \qquad 1\text{-}3$$

where R_{el}, R_i and R_c represents resistance of the electrodes, the solid electrolyte and the electrode-electrolyte contact, respectively. Among them, electrolyte resistance typically dominates the ohmic resistance because ionic resistivity is much greater than the electronic resistivity of both electrodes. Consequently, the ohmic polarization can be decreased by reducing the thickness of the electrolyte or using an electrolyte with higher ionic conductivity. In addition, the ohmic resistance decreases with a rise in operating temperature.

Concentration polarization: refers to the voltage loss accounting for the physical resistance to transport caused by diffusion of reactant species (e.g. O_2 and H_2) to and product species from the reaction sites. The concentration polarization from the cathode is much higher than that of the anode because the anode's binary diffusivity is four to five times greater than that of the cathode and the typical partial pressure of hydrogen in the fuel is much larger than that of oxygen in the oxidant. A thick cathode may also increases the difficulty for oxygen transport and, therefore, give rise to concentration polarization. The concentration polarization is typically reduced by increasing the gas flow rate or optimizing the microstructure of the electrode.

1.2 Materials for SOFCs

1.2.1 Electrolyte materials

Electrolyte materials must have the following characteristics.

- Stability: Electrolyte must have chemical, crystal and mechanical stability from room temperature to operating temperature and in both oxidizing and reducing atmospheres.
- Ionic conductivity: Electrolyte must have sufficient ionic conductivity and negligible electronic conductivity
- Compatibility with other materials: At both fabrication temperature and operating temperature, electrolyte should be compatible with other components of SOFC.
- Thermal expansion coefficient (TEC) match to other components: Electrolyte should have a similar TEC with electrode materials to avoid cracking or distortion.
- Gas tightness: Electrolyte should be dense enough that neither oxygen nor fuel gas cannot go through at any conditions.
- Low cost

The most widely used material for the electrolyte is zirconia (ZrO_2) usually stabilized with yttrium and known as yttrium stabilized zirconia (YSZ). It almost completely matches all the characteristics that an electrolyte material needs. The only disadvantage of YSZ is its ionic conductivity dramatically decreases with decreasing temperature. Thus for IT and LT-SOFCs, performance is limited by large ohmic loss from YSZ. Scandia (Sc_2O_3) doped ZrO_2 has a higher ionic conductivity than YSZ since the ionic radius of Sc^{3+} is closest to the radius of Zr^{4+} resulting in less lattice distortion and thus a smaller energy for oxygen migration. Fig 1-3 shows the ionic conductivity of YSZ and Sc stabilized zirconia (ScSZ) prepared by different methods. The disadvantage of ScSZ is its higher cost and long term phase instability.

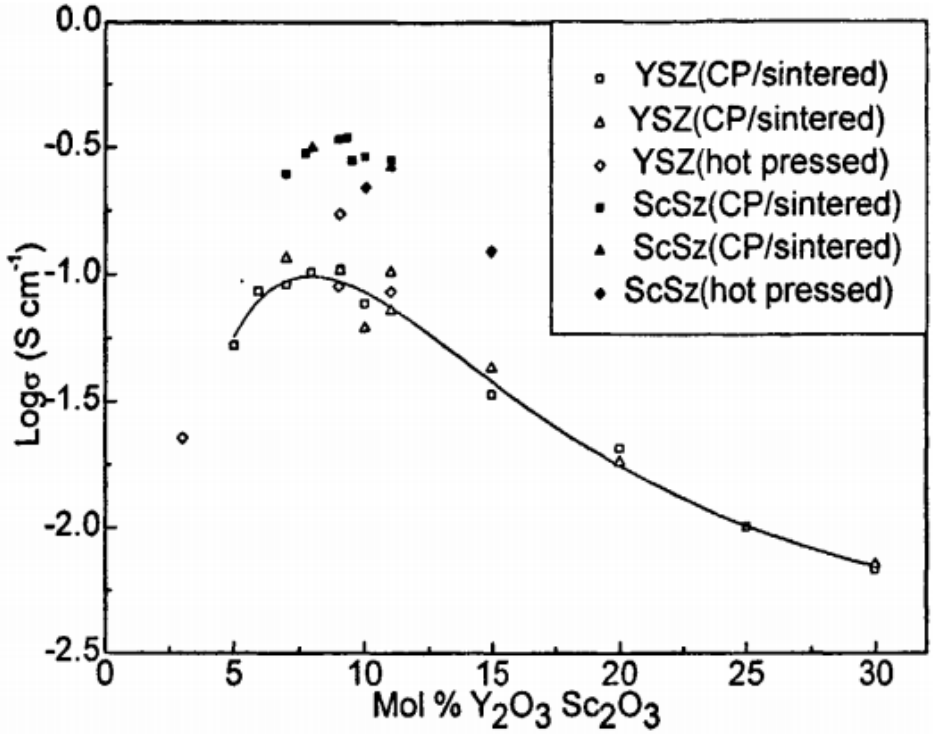

Figure 1-3 the ionic conductivity of YSZ and ScSZ at 1000 °C prepared by different methods (figure obtained from reference (*4*))

Acceptor doped ceria is also commonly considered as an SOFC electrolyte, and has the same fluorite structure as YSZ. Ceria has a much higher conductivity than YSZ due to its lower activation energy for oxide ion migration. Figure 1-4 shows the ionic conductivity of doped ceria at 1073 K

against the radius of dopant cation. The conductivity starts increasing with the increasing of dopant ionic radius and reach the highest point with Sm and decreasing with the larger ionic radius dopants. Kim proposed that the highest ionic conductivity would to be obtained in lattice with no strain which means that the dopant causes no change in lattice parameter compared to pure ceria. The radius of this dopant is called the critical radius. The critical radii, r_c, for divalent and trivalent cations as dopants in ceria are calculated as 0.1106 and 0.1038 nm. Gd^{3+} and Sm^{3+} doped ceria has the highest ionic conductivity because they have the closest match to r_c (*5*)

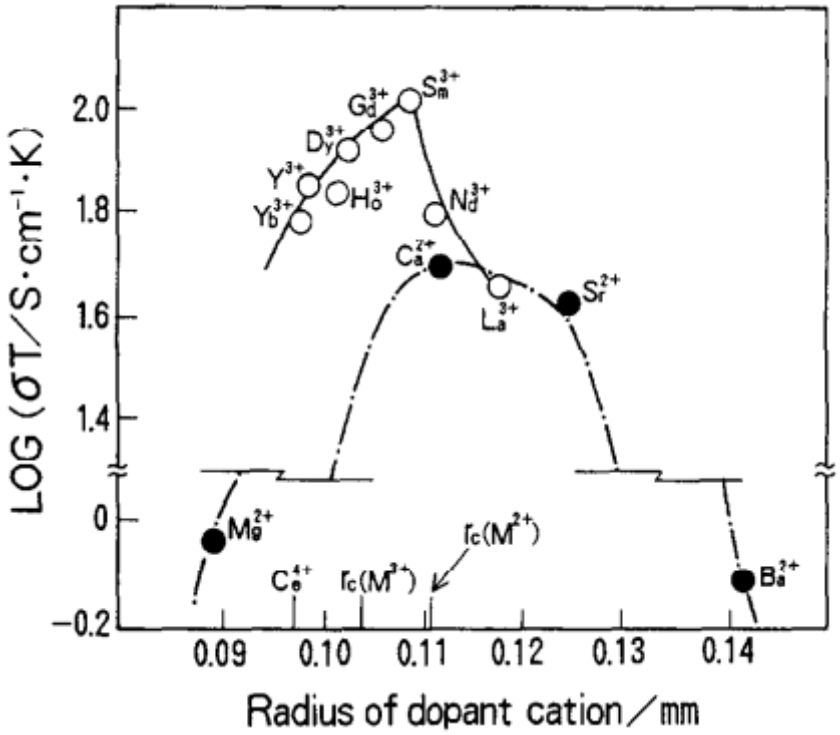

Figure 1-4 Ionic conductivity of doped ceria at 1073 K against the radius of dopant cation (figure obtained from reference (*6*))

The amount of dopant also has effect on the conductivity of doped ceria. Fig. 1-5 shows the concentration dependence of conductivities for Sm doped ceria. The conductivity increases with dopant concentration up to 10% after which it goes through a broad maximum and decreases again above ca. 20%. This behavior occurs because increasing the dopant concentration increases the oxygen vacancy concentration, but at high concentrations, point defects begin to interact and oxygen vacancies have more difficulty moving.

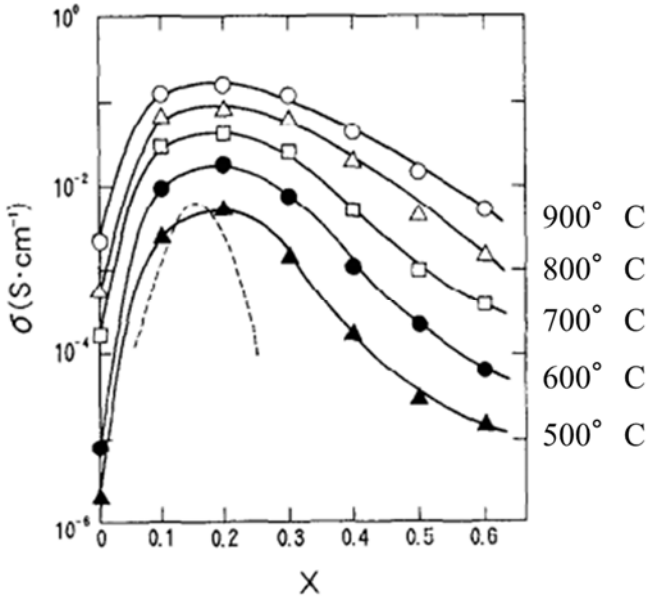

Figure 1-5 Concentration dependence of ionic conductivity for $(CeO_2)_{1-x}(SmO_{1.5})_x$ at different temperatures. Dashed line (---) is $(ZrO_2)_{1-x}(CaO)_x$, at 800 °C.(*7*)

A key issue when considering doped ceria as an electrolyte material is that Ce will partially reduce from 4+ to 3+ in reducing atmosphere, particularly at high temperatures, resulting in electronic conductivity. Steele el al. considered that electronic conductivity of $Ce_{0.9}Gd_{0.1}O_{1.95}$ can be ignored below 500 °C (*8*). Despite the instability in reducing conditions, doped ceria has an advantage for chemical stability relative to other materials, such as $La_{1-x}Sr_xFe_{1-y}Co_yO_3$ (LSCF), where YSZ is found to react. Therefore GDC is often used as the buffer layer between YSZ and cathode materials to prevent reaction.

Another electrolyte material, Sr^{2+}, Mg^{2+} doped $LaGaO_3$ (LSGM) has higher conductivity than YSZ and GDC or SDC (*9*). However, the formation of a second phase such as $LaSrGa_3O_7$ or $LaSrGaO_4$ is always observed (*10*). In order to obtain a single phase LSGM, great attention is required in its preparation. Additionally, there is chemical instability associated with Ga evaporation in reducing atmosphere.

1.2.2 Cathode materials

Several of the basic requirements that a cathode must satisfy are shown by the following list.

- High electronic conductivity (preferably more than 100 S cm^{-1} under oxidizing atmosphere)
- A matched thermal expansion coefficient (TEC) and chemical compatibility with the electrolyte and interconnect materials
- Adequate porosity to allow gaseous oxygen to readily diffuse through the cathode to the cathode/electrolyte interface
- Stability under an oxidizing atmosphere during fabrication and operation;
- High catalytic activity for the oxygen reduction reaction (ORR)
- Low cost

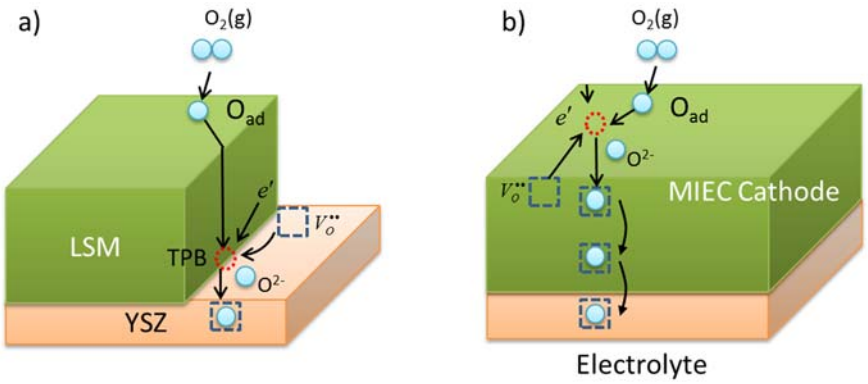

Figure 1-6 Oxygen reduction reaction strategies for cathode a) single-phase electronically conductive oxide such as LSM, and b) single-phase MIEC (e.g. LSCF).

The cathode can be a pure electronic conductor, a mixed ionic and electronic conductor (MIEC), or a composite of either type with an ionic conductor (e.g. electrolyte). For the electronic conductor, a typical choice is (La,Sr)$MnO_{3-\delta}$ (LSM) combined as a composite with YSZ. LSM material has high electronic conductivity, high catalytic activity, good chemical stability and a close TEC match with YSZ at high temperature (> 800 ºC). However, the absence of oxygen vacancies in LSM restricts the reduction of oxygen to the three-phase boundary regions as shown in Figure 1-6a. At lower temperatures (< 750 ºC), LSM does not have acceptable performance due to extreme degradation of its catalytic activity.

Figure 1-6b shows the oxygen reduction reaction strategy for an MIEC material. By having both ionic and electronic conductivity in the same phase, the reaction occurs over the whole surface of the cathode and the surface exchange rate increases. (La,Sr)$CoO_{3-\delta}$ has been identified as possessing perhaps the best transport properties in terms of both ionic and electronic conductivity. However, this material has a high TEC. Substituting iron for cobalt can lower the TEC of LSC. $La_{1-x}Sr_xFe_{1-y}Co_yO_{3-\delta}$ (LSCF) shows good electrical conductivity, a high oxygen surface exchange coefficient, and a good oxygen self-diffusion coefficient at intermediate temperature. LSCF is generally incompatible with YSZ electrolytes due to interfacial reactions. Therefore, as mentioned above, a Gd doped ceria (GDC) layer is used to prevent the interface reaction. The ionic conductivity of LSCF is not high enough, so a GDC/LSCF composite is usually used to reduce the polarization resistance. Also, high degradation rates in electrochemical performance for cells with LSCF cathodes have been observed and are due to diffusion of strontium out of LSCF. Sr-doped samarium cobaltite ($Sm_{1-x}Sr_xCoO_{3-\delta}$, SSC) is another widely studied cathode material for IT-SOFCs. The electrical conductivity of this composition shows metallic-like behavior and reaches up to 103 Scm^{-1} in the temperature range of 800–1100 °C. Its relatively high thermal expansion coefficient (greater than $20\times10^{-6}K^{-1}$(*11*) compared to 11.8 for LSM and 10.8 for YSZ(*12*)) could produce stresses at the interface during thermal cycling. In addition, reactivity tests of SSC with YSZ show that SSC is only stable below 800 °C because $SrZrO_3$ is formed at higher temperatures (*13*). The electrical conductivity and TEC of common perovskite cathode materials are shown in Table1-1 (*14*).

As described later in this introduction, $Pr_xCe_{1-x}O_{2-\delta}$ (PCO) is a fluorite structured oxide with mixed ionic electronic conductivity (Figure 1-7) and high oxygen exchange coefficient in cathode conditions (*15-17*). Like LSC, its TEC is relatively high.

Table 1-1. Perovskite-type oxide materials: thermal expansion coefficient (TEC), electronic (σ_e), and ionic conductivities (σ_i) in air, reproduced from (*14*).

Composition	TEC ($\times 10^{-6} K^{-1}$)	T (°C)	σ_e (Scm^{-1})	σ_i (Scm^{-1})
$La_{0.8}Sr_{0.2}MnO_3$	11.8	900	300	5.93×10^{-7}
$La_{0.7}Sr_{0.3}MnO_3$	11.7	800	240	–
$La_{0.6}Sr_{0.4}MnO_3$	13	800	130	–
$Pr_{0.6}Sr_{0.4}MnO_3$	12	950	220	–
$La_{0.8}Sr_{0.2}CoO_3$	19.1	800	1,220	–
$La_{0.6}Sr_{0.4}CoO_3$	20.5	800	1,600	0.22
$La_{0.8}Sr_{0.2}FeO_3$	12.2	750	155	–
$La_{0.5}Sr_{0.5}FeO_3$	–	550	352	–
	–	800	369	0.205
$La_{0.6}Sr_{0.4}FeO_3$	16.3	800	129	5.6×10^{-3}
$Pr_{0.5}Sr_{0.5}FeO_3$	13.2	550	300	–
$Pr_{0.8}Sr_{0.2}FeO_3$	12.1	800	78	–
$La_{0.7}Sr_{0.3}Fe_{0.8}Ni_{0.2}O_3$	13.7	750	290	–
$La_{0.8}Sr_{0.2}Co_{0.8}Fe_{0.2}O_3$	20.1	600	1,050	–
$La_{0.8}Sr_{0.2}Co_{0.2}Fe_{0.8}O_3$	15.4	600	125	–
$La_{0.6}Sr_{0.4}Co_{0.8}Mn_{0.2}O_3$	18.1	500	1,400	–
$La_{0.6}Sr_{0.4}Co_{0.8}Fe_{0.2}O_3$	21.4	800	269	0.058
$La_{0.6}Sr_{0.4}Co_{0.2}Fe_{0.8}O_3$	15.3	600	330	8×10^{-3}
$La_{0.4}Sr_{0.6}Co_{0.2}Fe_{0.8}O_3$	16.8	600	–	–
$La_{0.8}Sr_{0.2}Co_{0.2}Fe_{0.8}O_3$	14.8	800	87	2.2×10^{-3}
$La_{0.8}Sr_{0.2}Co_{0.8}Fe_{0.2}O_3$	19.3	800	1,000	4×10^{-2}
$La_{0.6}Sr_{0.4}Co_{0.9}Cu_{0.1}O_3$	19.2	700	1,400	–
$Pr_{0.8}Sr_{0.2}Co_{0.2}Fe_{0.8}O_3$	12.8	800	76	1.5×10^{-3}
$Pr_{0.7}Sr_{0.3}Co_{0.2}Mn_{0.8}O_3$	11.1	800	200	4.4×10^{-5}
$Pr_{0.6}Sr_{0.4}Co_{0.8}Fe_{0.2}O_3$	19.69	550	950	–
$Pr_{0.4}Sr_{0.6}Co_{0.8}Fe_{0.2}O_3$	21.33	550	600	–
$Pr_{0.7}Sr_{0.3}Co_{0.9}Cu_{0.1}O_3$	–	700	1236	–
$Ba_{0.5}Sr_{0.5}Co_{0.8}Fe_{0.2}O_3$	20	500	30	–
$Sm_{0.5}Sr_{0.5}CoO_3$	20.5	700~900	>1,000	–
$LaNi_{0.6}Fe_{0.4}O_3$	11.4	800	580	–
$Sr_{0.9}Ce_{0.1}Fe_{0.8}Ni_{0.2}O_3$	18.9	800	87	0.04

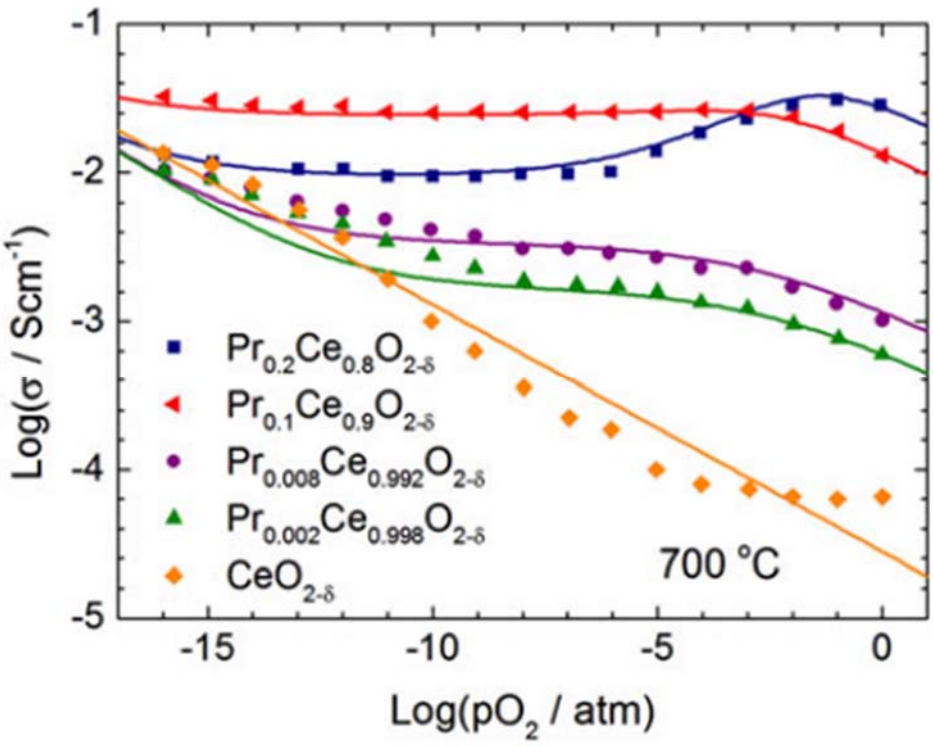

Figure 1-7 Log σ versus logPO_2 for a series of compositions in the system $Pr_xCe_{1-x}O_{2-\delta}$ (x=0, 0.002, 0.008, 0.1, 0.20) measured at 700 °C(*17*).

1.2.1 Anode materials

The following are a number of criteria to be considered when choosing an anode.

- High electronic conductivity
- Catalytic activity for fuel oxidation/combustion
- High ionic conductivity
- Stability on successive reducing and oxidizing (redox) cycles
- Thermal stability
- Chemical stability to contacting components
- Matched thermal expansion coefficient (TEC) to contacting components
- Low cost

The composite anode, Ni/YSZ has high electronic conductivity, reasonable ionic conductivity and high catalytic activity for hydrogen oxidation. This material fulfils most of the requirements of the anode. However, it has problems such as carbon deposition when using hydrocarbon fuels, susceptibility to sulphur poisoning, long-term nickel agglomeration, and the Ni is not redox stable. Redox instability was found to occur upon anodic re-oxidation and was a result of the expansion of Ni to NiO, which produced stresses at the anode-electrolyte interface. (*18*)

As an alternative, CeO_2 based materials exhibit mixed ionic and electronic conductivity in a reducing atmosphere due to reduction of Ce^{4+} to Ce^{3+}. The Ce^{4+}/Ce^{3+}redox couple has been shown to be catalytically active for CO and hydrocarbon oxidation (*19*). Additionally, GDC or SDC with Ni were found to have increased performance compared to Ni/YSZ when methane was used as a fuel (*20*). Wan et al. reported that with a La-doped ceria (LDC)/Ni anode with an LDC buffer layer

exhibited a power density as high as 1.4 W cm^{-2} at 800 ◦C in H_2 (*21*). Pure and doped ceria have also been found to promote catalytic activity for hydrocarbon oxidation reactions without coking (*22*). Marina et al. (*23*) and Livermore et al. (*24*) have reported a high activity to methane oxidation without carbon deposition with a Ni/GDC cermet anode. Although with doped or undoped ceria, the carbon deposition can be reduced, Ni is still required to provide the electronic conductivity, and thus the composite still suffers from nickel agglomeration and redox instability. Gorte et al. reported that ceria based ceramic anodes with small amounts of metal additives such as Cu or Pd performs reliably for hydrocarbon fuels. Moreover, the ceria-based anodes with Cu exhibit a high tolerance to sulfur poisoning. (*25*)

1.3 Defect equilibrium

The Brouwer approximation, has been used to delineate regions in the isothermal plot of defect concentration versus pO_2, resulting in the defect equilibrium diagram for undoped ceria and doped ceria, shown in Figures 1-7,8,9 and discussed below.

Undoped ceria

The reduction of undoped ceria when exposed to reducing atmospheres at elevated temperatures can be described by the following defect reaction.

$$O_O^{\times} \leftrightarrow V_O^{\bullet\bullet} + 2e^{/} + 1/2O_2(g) \qquad 1\text{-}4$$

where $O_o^{\times}$, $V_O^{\bullet\bullet}$ and e' refer to oxygen on a normal lattice site, oxygen vacancies and electrons, respectively. Brackets, i.e. $[V_O^{\bullet\bullet}]$ and n (=$[e']$), refer to the concentrations of oxygen vacancies and electrons. The electroneutrality condition is expressed by

$$[e'] = 2[V_O^{\bullet\bullet}] \qquad 1\text{-}5$$

with the corresponding equilibrium constant (K_R) defined by

$$K_R = [V_O^{\bullet\bullet}] \cdot n^2 \cdot pO_2^{1/2} = K_0 \exp\frac{-H_r}{kT} \qquad 1\text{-}6$$

where K_0 is a pre-exponential factor (containing vibrational entropy), H_r is the reduction enthalpy for the reaction, and k is the Boltzmann constant. Equation1-6 is simplified by substitution with Equation 1-5, yielding

$$n = pO_2^{-1/6}(2K_R)^{1/3} \qquad 1\text{-}7$$

This pO_2 dependence for the concentration of e' (from Equation 1-7) and $V_O^{\bullet\bullet}$ (from Equation 1-5) is shown in Figure 1-8

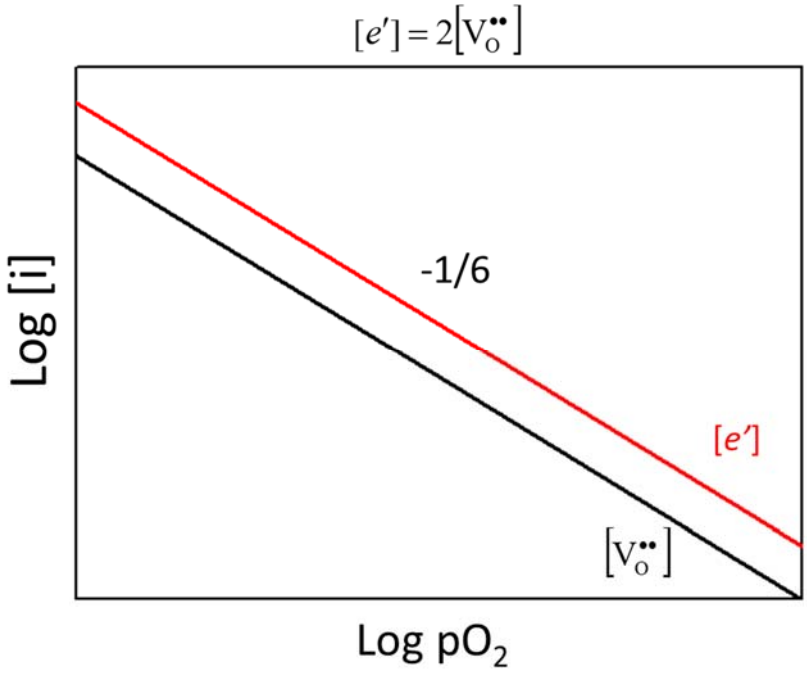

Figure 1-8 Defect equilibrium diagram for undoped ceria.

Fixed valent acceptor (i.e. Gd) doped ceria

In the case of a fixed valent acceptor dopant (A) doped ceria, the doping reaction is written as

$$Gd_2O_3 \rightarrow 2Gd'_{Ce} + 3O_O^{\times} + V_O^{\cdot\cdot} \qquad 1\text{-}8$$

In the ionic region of doped ceria (region I), the concentration of electronic charge carriers is negligible and the concentration of oxygen ion vacancies is fixed by the acceptor dopant concentration.

$$[A'_{Ce}] \approx 2[V_O^{\bullet\bullet}] \approx \text{const.} \qquad 1\text{-}9$$

This result can be substituted into Equation 1-6 as shown by the following equation.

$$n = pO_2^{-1/4}\left(\frac{2K_R}{[A'_{Ce}]}\right)^{1/2} \qquad 1\text{-}10$$

From this equation, one observes the -1/4 power law for the dependence of e' concentration on oxygen partial pressure, shown in region I of Figure 1-9. At lower pO_2 (region II of Figure 1-9), Ce^{4+} is reduced to Ce^{3+}, reaction as Equation 1-4 is dominant, therefore, $V_O^{\bullet\bullet}$ and e' follow a $pO_2^{-1/6}$ dependence

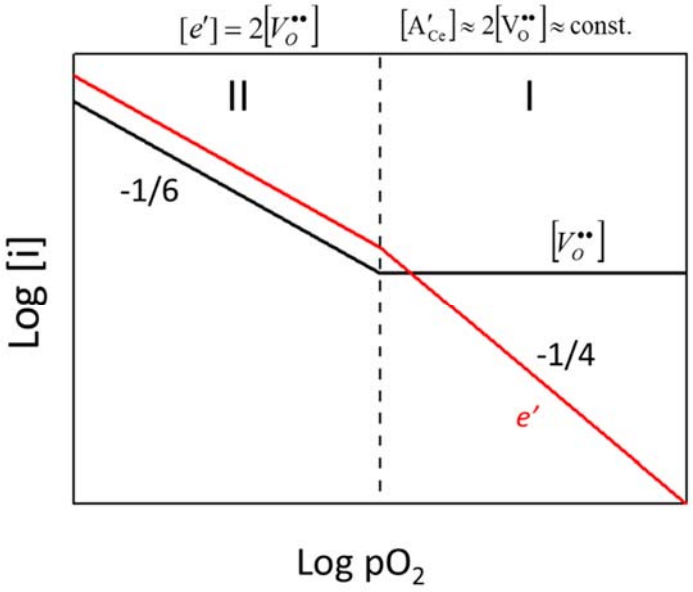

Figure 1-9 Defect equilibrium diagram for a fixed valent acceptor dopant (A) doped ceria

Multivalent acceptor (i.e. Pr) doped ceria

In the case of a multivalent acceptor (M) doped ceria, defect reactions and equilibrium equations are shown in Table 1-2. In the example, for sufficiently high pO_2, most of the M takes on the +4 state, then $[M_{Ce}^{\times}] \approx$ const. Therefore, Equation 1-13 can be substituted into Equation 1-12 to yield $1/2[M'_{Ce}] \approx [V_O^{\bullet\bullet}] \propto pO_2^{-1/6}$, which is shown in region I of Figure 1-10. In the intermediate pO_2 region (region II of Figure 1-10), M atoms are nearly all reduced to trivalent, according to Equation 1-13, then $1/2[M'_{Ce}] \approx [V_O^{\bullet\bullet}] \approx$ const., similar to the case for fixed valent acceptor doped ceria in high pO_2. By using Equation 1-12, one can predict $[M_{Ce}^{\times}] \propto pO_2^{1/4}$, and by Equation 1-6, $n \propto pO_2^{-1/4}$. With further decreasing pO_2, Ce^{4+} begins to be reduced, $V_O^{\bullet\bullet}$ and e' follow a $pO_2^{-1/6}$ dependence, as was shown in Figures 1-6 and 1-7.

Table 1-2 Defect reactions and equilibrium equations for a multivalent acceptor dopant (M) doped ceria

$2M_{Ce}^{\times} + O_O^{\times} \leftrightarrow 2M'_{Ce} + V_O^{\bullet\bullet} + 1/2O_2(g)$	1-11
$K_R = \frac{[M'_{Ce}]^2[V_O^{\bullet\bullet}] \cdot P_{O_2}^{1/2}}{[M_{Ce}^{\times}]^2[O_O^{\times}]}$	1-12
$[M'_{Ce}] \approx 2[V_O^{\bullet\bullet}]$	1-13
$[M'_{Ce}] + [M_{Ce}^{\times}] = x[M_xCe_{1-x}O_2]$	1-14

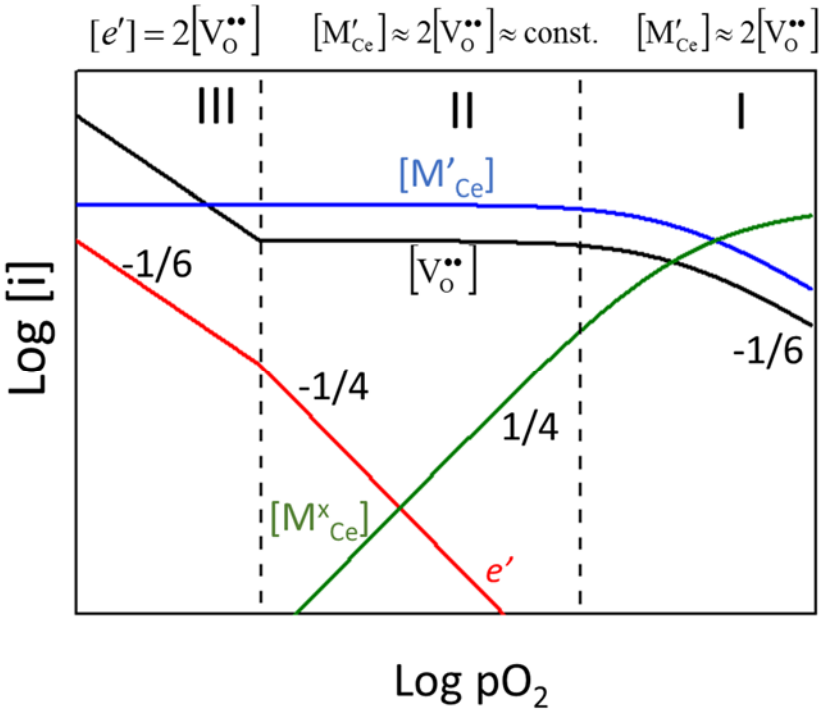

Figure 1-10 Defect equilibrium diagram for a multivalent acceptor dopant (i.e. Pr) doped ceria

Electrical Conductivity

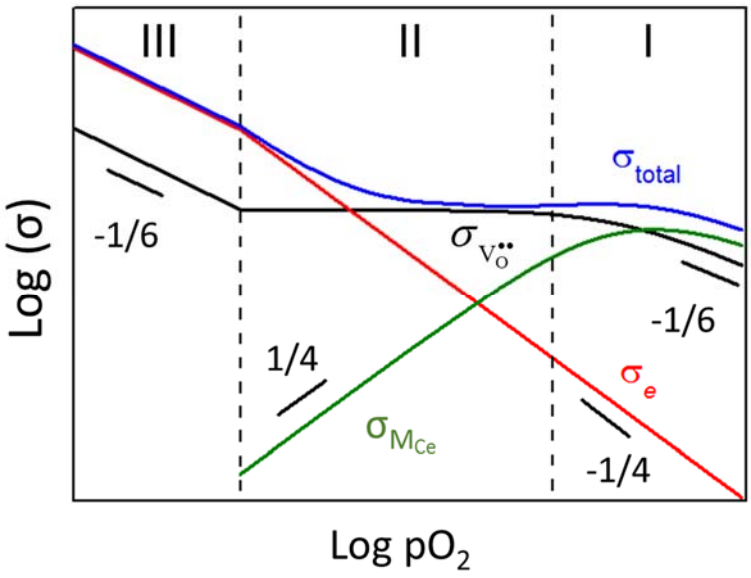

Figure 1-11 Conductivity for a multivalent acceptor dopant (i.e. Pr) doped ceria

The total electrical conductivity is the sum of electronic conductivity (σ_e) and ionic conductivity

(σ_i), as shown below (assuming n-type electronic conduction).

$$\sigma_{tot} = \sigma_e + \sigma_i \quad \text{1-15}$$

where σ_e and σ_i are defined as

$$\sigma_i = 2q\mu_i[V_O^{\bullet\bullet}] \quad \text{1-16}$$

$$\sigma_e = q\mu_e n \quad \text{1-17}$$

where q, μ_i, n, μ_e, are the elementary charge of an electron, oxygen vacancy mobility, concentration of electrons, and electronic mobility, respectively. The mobility of an oxygen vacancy and an electron are defined as:

$$\mu_i = \frac{\mu_{o,V}}{T}\exp(-\frac{H_{m,V}}{kT}) \quad \text{1-18}$$

$$\mu_e = \frac{\mu_{o,e}}{T}\exp(-\frac{H_{m,e}}{kT}) \quad \text{1-19}$$

where $\mu_{o,V}$, $\mu_{o,e}$, $H_{m,V}$, and $H_{m,e}$ are the mobility pre-exponential and enthalpy of migration for oxygen vacancies and electrons, respectively. Therefore, at the same temperature the mobility is constant and σ_i and σ_e follow the same pO_2 dependence with $V_O^{\bullet\bullet}$ and e' shown in Figure 1-10 and Figure 1-11.

In the high pO_2 (region I of Figure 1-11), electrons on M^{3+} sites can hop to an adjacent M^{4+} site, and this electronic conductivity is expressed as $\sigma_{M_{Ce}}$. With decreasing pO_2 in region I, $\sigma_{M_{Ce}}$ initially increases with increasing $[M'_{Ce}]$. With a further decrease in pO_2, there is not enough M^{4+} for electrons to hop to, and conductivity begins to decrease. Following Equation 14, the maximum of $\sigma_{M_{Ce}}$ is expected when $[M'_{Ce}] = [M^{\times}_{Ce}]$ and is thus proportional to $[M'_{Ce}][M^{\times}_{Ce}]$.

1.4 Techniques for study of defect equilibria and transport

In the above section, we discussed the theory of defect equilibrium and transport of undoped and doped ceria. In this section we will briefly describe techniques for studying the defect equilibrium and transport: thermogravimetric analysis (TGA), electro-chemical impedance spectroscopy (EIS), and optical transmission relaxation (OTR).

1.4.1 Thermogravimetric Analysis (TGA)

TGA measures the amount of weight change of a material, either as a function of temperature or

pO_2 or time. Almost any class of materials, inorganic materials, metals, polymers and plastics, ceramics, glasses, and composite materials can and have been analyzed by TGA. A thermogravimentric analyzer is normally composed of a microbalance, a furnace, a temperature programmer, a sample holder, an enclosure for establishing the required atmosphere, and a means of recording and displaying the data.

TGA can be used for

- Material characterization, to identify materials or to determine the purity of materials.
- As a reactor to analyze the change in mass with oxidation (i.e. oxygen uptake), or other reactions with gases including decomposition reactions or change of water content.
- Kinetic studies of weight loss or gain

For doped ceria, the reaction for oxygen uptake or loss can be expressed by Equation 1-4 and 1-11. In this work, TGA has been used to measure the oxygen loss or gain as a function of temperature and pO_2 to calculate the change in oxygen nonstoichiometry of Mn doped ceria. The same method has been used for GDC and PCO (*16, 26*). In order to determine the solubility of Mn in ceria, a phase diagram of Mn oxides was determined by TGA.

1.4.2 Electrical impedance spectroscopy (EIS)

A typical impedance spectrum for conductivity measurement is shown in Figure 1-12. Typically, the diameter of the arc is sample resistance, the imaginary part represents capacitive components and the real part represents resistance. Electrodes, at which charged species tend to equilibrate, are called non-blocking and those where there is no immediate equilibration of charged species are called blocking electrodes. For a non-blocking electrode, the initial potential will frequently be the equilibrium potential, i.e. the initial current will in this case be zero. Often a non or partially-blocking electrode will behave like a resistance R and capacitance C in parallel. This leads to a semicircle in the impedance plane. At the maximum of the semicircle, the angular frequency is designated as ω_{max}; then $RC=1/\omega_{max}$. (*27*). In the case of electrodes with significantly different RC values, the arcs are clearly non overlapping as shown as Figure 1-12.

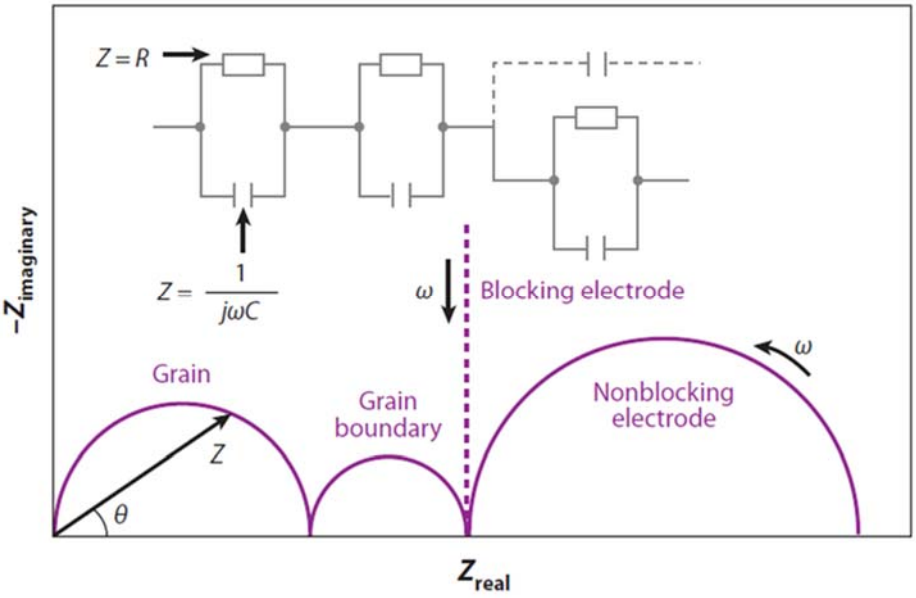

Figure 1-12 Typical impedance spectra for conductivity measurement.

Figure 1-12 shows an ideal EIS spectra. Since it is a frequency based technique, EIS can be used to separate the grain, grain boundary and electrode resistance. Z, ω, C are the symbols for impedance, frequency and capacitance.

EIS has been used to measure the conductivity of Eu-CeO_2 and Mn-CeO_2 in this work.

1.4.1 Optical transmission relaxation (OTR)

OTR can be used to measure the non-stoichiometry and oxygen exchange coefficient of samples, and the electrode electrochemical durability during long term measurements. The advantage of OTR is there is no need of other treatment or measurement (as in the case of tracer measurements) and no need for a current collector (as in area specific resistance measurements) allowing better control of surface morphology.

However, a drawback this optical based technique is that it requires optically active defect centers For example, in PCO, the excitation of an electron from the valence band into a Pr^{4+} level leading to a reddish color which is decreased with increasing Pr^{3+} concentration.

1.5 Challenges of SOFC and study in this thesis

1.5.1 Challenges

The main barriers to SOFC wide commercialization are high cell costs, long start-up and shut-down cycle times, and low durability due in part to reaction between component materials and chemical/mechanical/thermal shocks. Lowering the operating temperature can suppress degradation of components and extend the range of acceptable materials and reduce the startup / shutdown time. However, reducing the operating temperature decreases the conductivity of the electrolyte and the

slowing of electrode kinetics, resulting in a large ohmic and polarization resistances. By using a thin film electrolyte, the ohmic resistance can be reduced significantly. Therefore, the overall cell performance is determined by the polarization losses of the electrochemical reactions at the anodes and cathodes, and the key technical challenge is how to minimize electrode polarization losses at lower operating temperatures.

Furthermore, the long-term durability of electrode performance is as important as initial performance. Impurities in the operating environment (e.g. in feed gases or in the cell materials) are well known to contribute to long-term degradation in performance of SOFCs, therefore, in part, hindering widespread SOFC commercialization. For example, Si based phases (siliceous material) have been found to block the active sites to oxygen exchange at the gas/solid interface on yttria-stabilized zirconia (YSZ),(*28-30*) Gd doped ceria (GDC),(*31*) (La,Sr)(Co,Fe)$O_{3-\delta}$ (LSCF),(*32-34*) and (La,Sr)$CoO_{3-\delta}$ (LSC)(*35*) electrode materials. In larger quantities, siliceous material can also cover the interface between electrode and electrolyte, thereby reducing the highly active triple phase boundary length between gas and NiO/YSZ(*36-39*) and LSM/YSZ(*40-42*) composite electrodes. Si is ubiquitous in ceramics processing and testing; for example, it can come from furnace refractories during high temperature sintering,(*43*) or even from the silicone grease used in the apparatus to establish input gas mixtures for fuel cell test assemblies.(*28*)

1.5.2 Research approach in this thesis

In order to lower the polarization resistance of the electrode, a favorable electronic and ionic conductivity as well as a high catalytic activity for oxygen reduction must be maintained. A strategy is to use mixed ionic electronic conductor (MIEC) materials. For typical electronic conducting electrode materials, the reaction can only occur at the triple-phase boundary (TPB) (i.e., gas–electrolyte–electrode), requiring an extended porous composite electrode structure for gas, ion, and electron transport. With MIEC materials, the reaction sites extend from TPB to the two-phase boundary (gas–cathode surface) allowing oxygen exchange over the entire electrode surface. Additionally, MIEC materials can also lower the energy barrier of oxygen exchange reaction.

Pure ceria is a fluorite structured oxide and exhibits MIEC in a reducing atmosphere due to reduction of Ce^{4+} to Ce^{3+} with simultaneous formation of oxygen vacancies(*44*). In addition, ceria is known as a good catalyst for the oxidation of hydrocarbons stemming from its ready oxygen exchange with the atmosphere associated with the reversible CeO_2–Ce_2O_3 transition (*45*). Dopants can be introduced into ceria to control certain electrical properties, for example, the oxygen vacancy concentration, and consequent ionic conductivity, can be dramatically increased by substitution of Gd^{3+} or Sm^{3+} for Ce, thereby facilitating its use as an electrolyte in solid oxide fuel cells (SOFCs). Similarly, by doping with multivalent acceptor dopant (e.g. Mn^{3+}), the oxygen vacancy concentration may be increased. Additionally, mixed-valence Mn in ceria may enhance the electronic conductivity due to reduction of Mn^{3+} to Mn^{2+} in low partial pressures of oxygen, thus acting as an additional redox couple besides Ce^{4+}/Ce^{3+}. Such MIEC behavior is known to improve cathode oxygen exchange kinetics in SOFCs (*46*).

Previous reports have shown that Ce–Fe mixed oxides have high catalytic activity for the oxidation of CO or hydrocarbons (*47-49*). Lv et al. also found that Fe doped ceria is a promising candidate an SOFC anode operating on methane fuel (*50*). Ce–Mn mixed oxides have high catalytic activity for the oxidation of hydrocarbons or ethanol (*51-53*). Maupoey et al. reported that Eu^{3+} can be reduced

to Eu^{2+} in $Sr_2EuNb_{1-x}Ti_xO_6$ at pO_2 as high as 10^{-10} atm (*54*). Fabbri et al. considered that the electronic conductivity observed in $SrCe_{0.9}Eu_{0.1}O_3$ an d $BaCe_{0.9}Eu_{0.1}O_3$ under oxidizing conditions is the result of the dopant redox couple Eu^{3+}/Eu^{2+} (*55*).

Therefore, Mn, Fe or Eu doped ceria are potential MIEC electrode materials. In this study, Mn, Fe and Eu-doped ceria were prepared, and the electrical properties were studied as a function of temperature and oxygen partial pressure using impedance spectroscopy. The solubility of Mn or Fe dopant in ceria was also investigated.

For the long-term degradation due to siliceous impurities, past researchers have spent significant effort and cost to reduce siliceous impurities through clean processing (*56, 57*). Previously, others have found that La may getter Si impurities at grain boundaries of (GDC);(*58*) additionally, early studies have shown that La added to the surface of GDC improved its oxygen exchange rate by >10 x which may arise from a possible cleaning effect.(*59*) In this work, optical transmission relaxation (OTR) is used in combination with deposition of second phase oxides using pulsed laser deposition (PLD) on the surface of PCO to systematically identify materials that will improve the redox kinetics of aged films (degraded by the presence of impurities). The present work builds substantially on this latter earlier finding by systematically identifying other oxide surface treatments that dramatically enhance redox kinetics after aging of PCO films and further aiding in establishing the mechanism for enhancement. Additionally, by simply integrating La into the PCO electrode in a solid solution, a more impurity-tolerant electrode amenable to industrial processing is demonstrated with positive initial results.

Reference

1. K. Hassmann, SOFC Power Plants, the Siemens-Westinghouse Approach. *Fuel Cells* **1**, 78-84 (2001).
2. N. Q. Minh, Ceramic Fuel-Cells. *Journal of the American Ceramic Society* **76**, 563-588 (1993).
3. E. Ivers-Tiffée, A. V. Virkar, in *High Temperature and Solid Oxide Fuel Cells,* S. C. Singhal, K. Kendal, Eds. (Elsevier Science, Amsterdam, 2003), pp. 229-260.
4. J. W. Fergus, Ceramic and polymeric solid electrolytes for lithium-ion batteries. *Journal of Power Sources* **195**, 4554-4569 (2010).
5. D. J. Kim, Lattice-Parameters, Ionic Conductivities, and Solubility Limits in Fluorite-Structure $Hf^{-4+}O_2$, $Zr^{-4+}O_2$, $Ce^{-4+}O_2$, $Th^{-4+}O_2$, $V^{-4+}O_2$ Oxide Solid-Solutions. *Journal of the American Ceramic Society* **72**, 1415-1421 (1989).
6. H. Inaba, H. Tagawa, Ceria-based solid electrolytes - Review. *Solid State Ion.* **83**, 1-16 (1996).
7. H. Yahiro, Y. Eguchi, K. Eguchi, H. Arai, Oxygen Ion Conductivity of the Ceria Samarium Oxide System with Fluorite Structure. *J Appl Electrochem* **18**, 527-531 (1988).
8. B. C. H. Steele, Appraisal of $Ce_{1-y}Gd_yO_{2-y/2}$ electrolytes for IT-SOFC operation at 500 degrees C. *Solid State Ion.* **129**, 95-110 (2000).
9. K. Q. Huang, R. Tichy, J. B. Goodenough, Superior perovskite oxide-ion conductor; strontium- and magnesium-doped LaGaO3: III, Performance tests of single ceramic fuel cells. *Journal of the American Ceramic Society* **81**, 2581-2585 (1998).
10. T. Ishihara, Development of new fast oxide ion conductor and application for intermediate temperature solid oxide fuel cells. *Bull. Chem. Soc. Jpn.* **79**, 1155-1166 (2006).
11. T. Ishihara, M. Honda, T. Shibayama, H. Minami, H. Nishiguchi, Y. Takita, Intermediate temperature solid oxide fuel cells using a new $LaGaO_3$ based oxide ion conductor - I. Doped $SmCoO_3$ as a new cathode material. *Journal of the Electrochemical Society* **145**, 3177-3183 (1998).
12. A. J. Jacobson, Materials for Solid Oxide Fuel Cells. *Chem. Mat.* **22**, 660-674 (2010).
13. H. Y. Tu, Y. Takeda, N. Imanishi, O. Yamamoto, Ln(1-x)Sr(x)CoO(3) (Ln=Sm, Dy) for the electrode of solid oxide fuel cells. *Solid State Ion.* **100**, 283-288 (1997).
14. C. W. Sun, R. Hui, J. Roller, Cathode materials for solid oxide fuel cells: a review. *J Solid State Electr* **14**, 1125-1144 (2010).
15. D. Chen, S. R. Bishop, H. L. Tuller, Praseodymium-cerium oxide thin film cathodes: Study of oxygen reduction reaction kinetics. *J Electroceram* **28**, 62-69 (2012).
16. S. R. Bishop, T. S. Stefanik, H. L. Tuller, Electrical conductivity and defect equilibria of $Pr_{0.1}Ce_{0.9}O_{2-\delta}$. *Phys Chem Chem Phys* **13**, 10165-10173 (2011).
17. S. R. Bishop, T. S. Stefanik, H. L. Tuller, Defects and transport in PrxCe1-xO2-delta: Composition trends. *J Mater Res* **27**, 2009-2016 (2012).
18. A. Faes, A. Nakajo, A. Hessler-Wyser, D. Dubois, A. Brisse, S. Modena, J. Van Herle, RedOx study of anode-supported solid oxide fuel cell. *Journal of Power Sources* **193**, 55-64 (2009).
19. A. Bieberle, L. J. Gauckler, Ni-based SOFC anodes: Microstructure and electrochemistry. *Z Metallkd* **92**, 796-802 (2001).

20. T. Hibino, A. Hashimoto, M. Yano, M. Suzuki, M. Sano, Ru-catalyzed anode materials for direct hydrocarbon SOFCs. *Electrochimica Acta* **48**, 2531-2537 (2003).
21. J. H. Wan, J. Q. Yan, J. B. Goodenough, LSGM-based solid oxide fuel cell with 1.4 W/cm(2) power density and 30 day long-term stability. *Journal of the Electrochemical Society* **152**, A1511-A1515 (2005).
22. S. Xu, X. L. Wang, Highly active and coking resistant Ni/CeO_2-ZrO_2 catalyst for partial oxidation of methane. *Fuel* **84**, 563-567 (2005).
23. O. A. Marina, C. Bagger, S. Primdahl, M. Mogensen, A solid oxide fuel cell with a gadolinia-doped ceria anode: preparation and performance. *Solid State Ion.* **123**, 199-208 (1999).
24. S. J. A. Livermore, J. W. Cotton, R. M. Ormerod, Fuel reforming and electrical performance studies in intermediate temperature ceria-gadolinia-based SOFCs. *Journal of Power Sources* **86**, 411-416 (2000).
25. H. P. He, R. J. Gorte, J. M. Vohs, Highly sulfur tolerant Cu-ceria anodes for SOFCs. *Electrochem. Solid State Lett.* **8**, A279-A280 (2005).
26. S. R. Bishop, K. L. Duncan, E. D. Wachsman, Defect equilibria and chemical expansion in non-stoichiometric undoped and gadolinium-doped cerium oxide. *Electrochimica Acta* **54**, 1436-1443 (2009).
27. P. G. Bruce, *Solid State Electrochemistry*.
28. M. de Ridder, A. G. J. Vervoort, R. G. van Welzenis, H. H. Brongersma, The limiting factor for oxygen exchange at the surface of fuel cell electrolytes. *Solid State Ion.* **156**, 255-262 (2003).
29. J. L. Hertz, A. Rothschild, H. L. Tuller, Highly enhanced electrochemical performance of silicon-free platinum-yttria stabilized zirconia interfaces. *J Electroceram* **22**, 428-435 (2009).
30. E. Mutoro, N. Baumann, J. Janek, Janus-Faced SiO2: Activation and Passivation in the Electrode System Platinum/Yttria-Stabilized Zirconia. *J. Phys. Chem. Lett.* **1**, 2322-2326 (2010).
31. J. M. Bae, B. C. H. Steele, Properties of $La_{0.6}Sr_{0.4}Co_{0.2}Fe_{0.8}O_{3-\delta}$(LSCF) double layer cathodes on gadolinium-doped cerium oxide (CGO) electrolytes - I. Role of SiO_2. *Solid State Ion.* **106**, 247-253 (1998).
32. E. Bucher, W. Sitte, F. Klauser, E. Bertel, Oxygen exchange kinetics of $La_{0.58}Sr_{0.4}Co_{0.2}Fe_{0.8}O_3$ at 600 degrees C in dry and humid atmospheres. *Solid State Ion.* **191**, 61-67 (2011).
33. E. Bucher, C. Gspan, F. Hofer, W. Sitte, Post-test analysis of silicon poisoning and phase decomposition in the SOFC cathode material La0.58Sr0.4Co0.2Fe0.8O3-delta by transmission electron microscopy. *Solid State Ion.* **230**, 7-11 (2013).
34. M. M. Viitanen, R. G. von Welzenis, H. H. Brongersma, F. P. F. van Berkel, Silica poisoning of oxygen membranes. *Solid State Ion.* **150**, 223-228 (2002).
35. E. Bucher, W. Sitte, F. Klauser, E. Bertel, Impact of humid atmospheres on oxygen exchange properties, surface-near elemental composition, and surface morphology of $La(0.6)Sr(0.4)CoO_{3-\delta}$. *Solid State Ion.* **208**, 43-51 (2012).
36. S. D. Ebbesen, C. Graves, A. Hauch, S. H. Jensen, M. Mogensen, Poisoning of Solid Oxide Electrolysis Cells by Impurities. *Journal of the Electrochemical Society* **157**, B1419-B1429 (2010).
37. A. Hauch, S. H. Jensen, J. B. Bilde-Sorensen, M. Mogensen, Silica segregation in the Ni/YSZ electrode. *Journal of the Electrochemical Society* **154**, A619-A626 (2007).
38. K. V. Jensen, R. Wallenberg, I. Chorkendorff, M. Mogensen, Effect of impurities on structural

and electrochemical properties of the Ni-YSZ interface. *Solid State Ion.* **160**, 27-37 (2003).
39. Y. L. Liu, C. G. Jiao, Microstructure degradation of an anode/electrolyte interface in SOFC studied by transmission electron microscopy. *Solid State Ion.* **176**, 435-442 (2005).
40. J. A. Schuler, Z. Wuillemin, A. Hessler-Wyser, J. Van Herle, Glass-Forming Exogenous Silicon Contamination in Solid Oxide Fuel Cell Cathodes. *Electrochem. Solid State Lett.* **14**, B20-B22 (2011).
41. A. Hagen, Y. L. Liu, R. Barfod, P. V. Hendriksen, Assessment of the cathode contribution to the degradation of anode-supported solid oxide fuel cells. *Journal of the Electrochemical Society* **155**, B1047-B1052 (2008).
42. M. Backhaus-Ricoult, SOFC - A playground for solid state chemistry. *Solid State Sci* **10**, 670-688 (2008).
43. http://www.zircarceramics.com/.
44. H. L. Tuller, A. S. Nowick, SMALL POLARON ELECTRON-TRANSPORT IN REDUCED CEO2 SINGLE-CRYSTALS. *J. Phys. Chem. Solids* **38**, 859-867 (1977).
45. C. W. Sun, J. Sun, G. L. Xiao, H. R. Zhang, X. P. Qiu, H. Li, L. Q. Chen, Mesoscale organization of nearly monodisperse flowerlike ceria microspheres. *J. Phys. Chem. B* **110**, 13445-13452 (2006).
46. S. B. Adler, Factors governing oxygen reduction in solid oxide fuel cell cathodes. *Chem. Rev.* **104**, 4791-4843 (2004).
47. K. Z. Li, H. Wang, Y. G. Wei, D. X. Yan, Transformation of methane into synthesis gas using the redox property of Ce-Fe mixed oxides: Effect of calcination temperature. *Int. J. Hydrog. Energy* **36**, 3471-3482 (2011).
48. P. Singh, M. S. Hegde, Sonochemical synthesis of $Ce_{1-x}Fe_xO_{2-\delta}$ ($0 <= x <= 0.45$) and $Ce_{0.65}Fe_{0.33}Pd_{0.02}O_{2-\delta}$ nanocrystallites: oxygen storage material, CO oxidation and water gas shift catalyst. *Dalton Trans.* **39**, 10768-10780 (2010).
49. F. J. Perez-Alonso, M. L. Granados, M. Ojeda, P. Terreros, S. Rojas, T. Herranz, J. L. G. Fierro, M. Gracia, J. R. Gancedo, Chemical structures of coprecipitated Fe-Ce mixed oxides. *Chem. Mat.* **17**, 2329-2339 (2005).
50. H. Lv, D. J. Yang, X. M. Pan, J. S. Zheng, C. M. Zhang, W. Zhou, J. X. Ma, K. A. Hu, Performance of Ce/Fe oxide anodes for SOFC operating on methane fuel. *Mater. Res. Bull.* **44**, 1244-1248 (2009).
51. J. Xu, P. Li, X. F. Song, C. H. He, J. G. Yu, Y. F. Han, Operando Raman Spectroscopy for Determining the Active Phase in One-Dimensional $Mn_{1-x}Ce_xO_{2-\delta}$ Nanorod Catalysts during Methane Combustion. *J. Phys. Chem. Lett.* **1**, 1648-1654 (2010).
52. G. Zhou, P. R. Shah, R. J. Gorte, A study of cerium-manganese mixed oxides for oxidation catalysis. *Catal. Lett.* **120**, 191-197 (2008).
53. H. J. Li, G. S. Qi, Tana, X. J. Zhang, X. M. Huang, W. Li, W. J. Shen, Low-temperature oxidation of ethanol over a $Mn_{0.6}Ce_{0.4}O_2$ mixed oxide. *Appl. Catal. B-Environ.* **103**, 54-61 (2011).
54. Z. Maupoey, M. T. Azcondo, U. Amador, A. Kuhn, J. C. Perez-Flores, J. R. de Paz, N. Bonanos, F. Garcia-Alvarado, The role of the Eu^{3+}/Eu^{2+} redox-pair in the electrical properties of $Sr_2EuNb_{1-x}Ti_xO_{6-\delta}$ oxides. *J Mater Chem* **22**, 18033-18042 (2012).
55. E. Fabbri, T. K. Oh, S. Licoccia, E. Traversa, E. D. Wachsman, Mixed Protonic/Electronic Conductor Cathodes for Intermediate Temperature SOFCs Based on Proton Conducting Electrolytes. *Journal of the Electrochemical Society* **156**, B38-B45 (2009).

56. T. Andersen, K. V. Hansen, I. Chorkendorff, M. Mogensen, Strontium zirconate as silicon and aluminum scavenger in yttria stabilized zirconia. *Solid State Ion.* **190**, 82-87 (2011).
57. L. Ge, R. F. Li, S. C. He, H. Chen, L. C. Guo, Enhanced grain-boundary conduction in polycrystalline $Ce_{0.8}Gd_{0.2}O_{1.9}$ by zinc oxide doping: Scavenging of resistive impurities. *Journal of Power Sources* **230**, 161-168 (2013).
58. D. Ivanova, A. Kovalevsky, V. V. Kharton, F. M. B. Marques, Silica-scavenging effects in ceria-based solid electrolytes. *Bol Soc Esp Ceram V* **47**, 201-206 (2008).
59. J. Druce, J. A. Kilner, Improvement of Oxygen Surface Exchange Kinetics for CGO with Surface Treatment. *Journal of The Electrochemical Society* **161**, F99-F104 (2014).

Chapter 2 Experimental

2.1 Sample preparation

2.1.1 Powders

x mol% M-CeO_2 (M= Mn, Fe, Eu, Pr) powders were synthesized by modified Pechini method. This method uses citric acid as a chelating agent to create a gel of intimately mixed cations, thus aiding in creating a homogeneous composition (*1*). The flow chart of the method is shown in Figure 2-1. The metal nitrate, cerium nitrate, ethylene glycol, and citric acid were mixed into an aqueous solution and stirred. The molar ratio of metal cations: citric acid: ethylene glycol was 1: 2: 1, respectively. The mixture was heated to approximately 80 °C until a gel formed. After drying in an oven at 110 °C, the resulting powder was calcined at 650 °C for 5 hours to remove carbon and then calcined at 1200 °C for 3 hours.

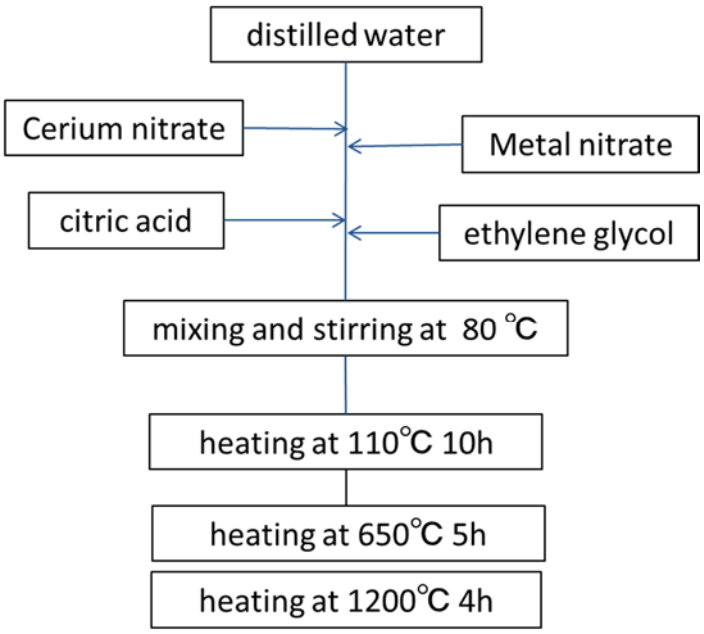

Figure 2-1 Flow chart for preparing M-CeO_2 (M= Mn, Fe, Eu, Pr) by modified Pechini method (all heat treatments shown were performed in air.)

The following starting materials were used: $Eu(NO_3)_3 \cdot 6H_2O$ (99.9%), $Mn(NO_3)_3 \cdot 6H_2O$ (99%) $Fe(NO_3)_3 \cdot 9H_2O$ (99%), $Ce(NO_3)_3 \cdot 6H_2O$ (98%), ethylene glycol (99.5%), citric acid (99.5%) (Kishida. Chemical Co. Ltd.), $Pr(NO_3)_3 \cdot 6H_2O$ (99.9%) (Mitsuwa), (99.99%) $Ce(NO_3)_3 \cdot 6H_2O$ (Sigma Aldrich).

To investigate the role of a reduction treatment on Mn or Fe solubility, some powders were also annealed in flowing H_2 bubbled through room temperature water at 1100 °C. In a separate, control experiment, Mn_3O_4 (98%) (Kishida. Chemical Co. Ltd.) and CeO_2 (99.9%) (Mitsuwa`s Pure

Chemicals) powders were mixed and milled by mortar and pestle with no heat treatment.

2.1.1 Pellets

The powders were made into pellets for electrical conductivity measurement and for use as targets for film deposition. First, powders were pressed uniaxially under dry conditions at 10 MPa, followed by isostatic pressing at 300 MPa. The resulting pellet was sintered at 1500 °C in air for 3 hours. The pellet for electrical conductivity measurement was cut to a bar. For SEM observation, the pellets were polished with SiC papers of decreasing roughness and diamond paste.

2.1.2 Films

PCO thin films were prepared by pulsed laser deposition (PLD) from the PCO targets. The films were deposited onto one side of two sides polished, oriented single crystal substrates: Al_2O_3 (0001), 8 mol% Y_2O_3stabilized zirconia (YSZ) (110), MgO (001), SiO_2 (X-cut) (10 × 10 × 0.5 mm^3; Keri Optoelectronic Tech., Dalian, China). The PCO films were deposited by a PLD machine (Pascal STD-PLD) with an excimer laser beam at a wavelength of 248 nm (COMPEX Pro 50F, Coherent). ~100 mJ direct output energy was focused to a spot size <0.5 cm^2 on a rotating target. The PCO films were deposited on substrates at 700 °C, 2 Pa O_2 with a repetition rate of 5 Hz for 20 minutes. The distance between the target and substrate during PLD was 5 cm. For surface treatments, 200 laser shots of La_2O_3, Gd_2O_3, Sm_2O_3, TiO_2; 300 shots of ZnO, Nb_2O_5; or 10 shots Al_2O_3 were deposited on the surface of as-prepared or aged PCO films. Targets were prepared from oxide powders: Gd_2O_3 (99.99%) (Kishida. Chemical), La_2O_3 (99.5%), Sm_2O_3 (99.9%), Nb_2O_5 (99.9%), TiO_2 (99.9%), Al_2O_3 (99.7%), or ZnO (99%) (Wako). For the surface treatments, the deposition was performed at room temperature under 2 Pa O_2 with a repetition rate of 5 Hz.

2.2 Characterization

X-ray diffraction (XRD)

The obtained powders were characterized by X-ray diffraction (XRD) using Cu-Kα radiation (Rigaku RINT-UltimaⅢ, 40kV/40mA). For accurate lattice parameter determination, the powders were measured by the parallel beam method with a 2.5 degree incident Soller slit, 1 mm divergence slit and 0.114 degree parallel slit analyzer to avoid most of the systematic errors. Also, silicon powder (NIST-640c) was used as an external standard in separate measurements. Lattice parameters were determined from the (422), (333), (440), (531), and (620) reflections which were located in the angular region of 80 to 130 degrees 2θ, wherein the effects of axial divergence are minimal. Lattice parameters were refined for fluorite ceria using the XRD data after stripping Kα-2 and background radiation using Jade 7 (Materials Data Incorporated).

For the film sample, X-ray diffraction (XRD; Rigaku Smartlab 9kw AMK Cu-Kα radiation) was performed using 2θ-ω coupled scans (Parallel beam/Parallel slit analyzer) (PB/PSA mode) with a 5 degree incident Soller slit and 0.114 degree parallel slit analyzer for phase and texture identification. The step size was 0.01 degree and speed was 1 degree per minute.

Raman spectroscopy

For Mn-CeO_2 and Fe-CeO_2, the secondary phases were also investigated by Raman spectroscopy using a 648 nm laser excitation source (HORIBA, HR-800).

Scanning electron and transmission microscopy (SEM/TEM)

In order to determine the secondary phases and grain size of the samples a scanning electron microscopy (SEM) (Hitachi S-5200) and Energy-dispersive X-ray spectroscopy (EDS) were used. The pellet sample was polished and thermally etched (1300 °C for 1 h) to observe the grain boundary clearly.

For a La_2O_3-treated PCO film, a cross-section was lifted out by a focused ion beam system/ SEM (FEI, Quanta™ 3D DualBeam™), and studied with energy-dispersive X-ray spectroscopy (EDS) by a scanning transmission electron microscope (STEM, JEOL, JEM-ARM200F).

X-ray Photoelectron Spectroscopy (XPS)

The surface compositions of film samples were determined by X-ray Photoelectron Spectroscopy (XPS, ULVAC-PHI, PHI5000 Versaprobe). A monochromated aluminum X-ray source of 1486.6 eV was used at a power of 25.34 W. A pass energy of 58.7 eV was used for survey scans of 5 cycles. Binding energy values were calibrated by setting the energy of the adventitious C 1s peak at 284.8 eV. The O 1s spectra of Si were fitted using Multipack software (Vlvac – Phi. Lnc.)

2.3 Electrochemical measurement

Impedance spectra were measured using an impedance analyzer (Novocontrol Technologies) from 0.1 Hz to 40 MHz with 60 logarithmically spaced data points and analyzed using Zview2 equivalent circuit modeling software (Scribner Associates, Inc.). The sample bars were wound with Pt wires coated with Pt paste to make two electrodes. Oxygen partial pressure was controlled by various dry N_2/O_2, CO/CO_2, and humidified N_2/H_2 gas mixtures with pO_2 monitored using an *in situ* Nernst-type zirconia oxygen sensor. A schematic of the experimental setup is shown in Figure 2-2.

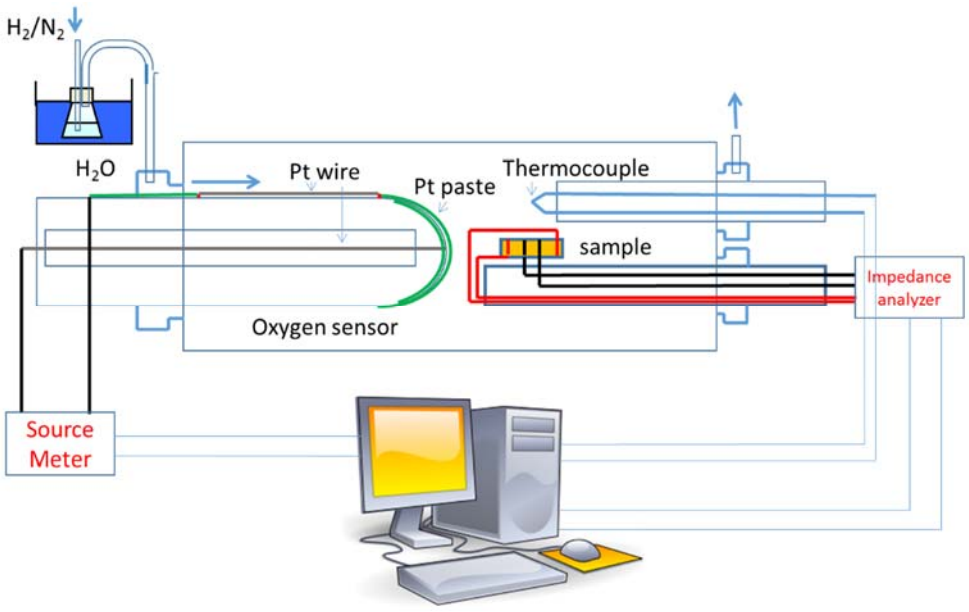

Figure 2-2 Schematic of the experimental setup for EIS

2.4 Thermogravimetric Analysis (TGA)

As shown in Figure 2-3, TGA was performed by suspending the samples from a microbalance (Excellence XP model, Mettler Toledo) within an alumina cup hanging from a Pt wire at elevated temperature (400 ~ 900 °C), in controlled atmospheres (N_2/O_2, CO/CO_2, humidified N_2/H_2 mixture). Balance sensitivity is around 0.01 mg, with a total capacity of a few grams. Samples were analyzed in the form of powder or small pieces. A Nernst-type zirconia oxygen sensor was inserted to allow for *in situ* pO_2 measurements. During a typical experiment, at constant temperature, pO_2 was changed in steps following the mass reaching equilibrium. pO_2 was typically first stepped down and then stepped back up to check reversibility.

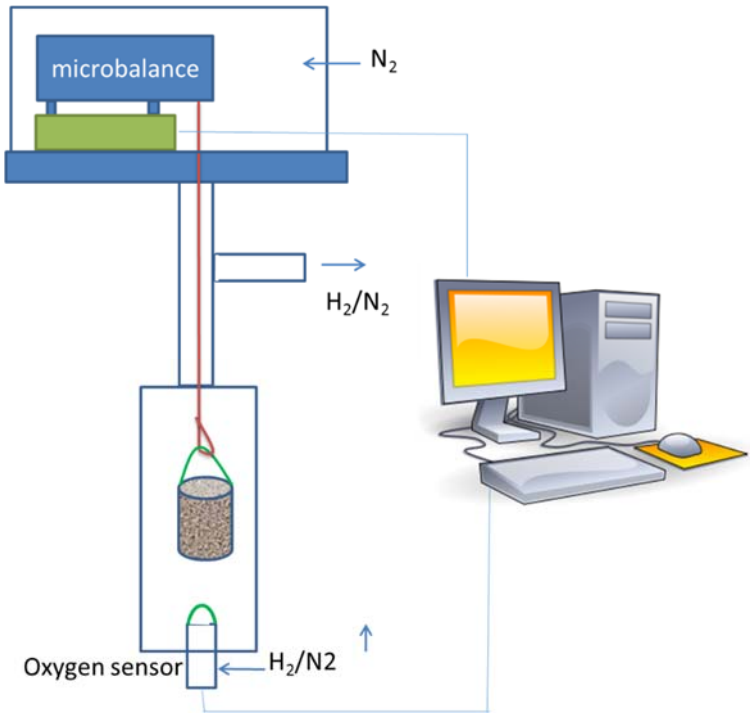

Figure 2-3 Schematic of the experimental setup for TGA

2.5 Optical transmission relaxation (OTR) measurement

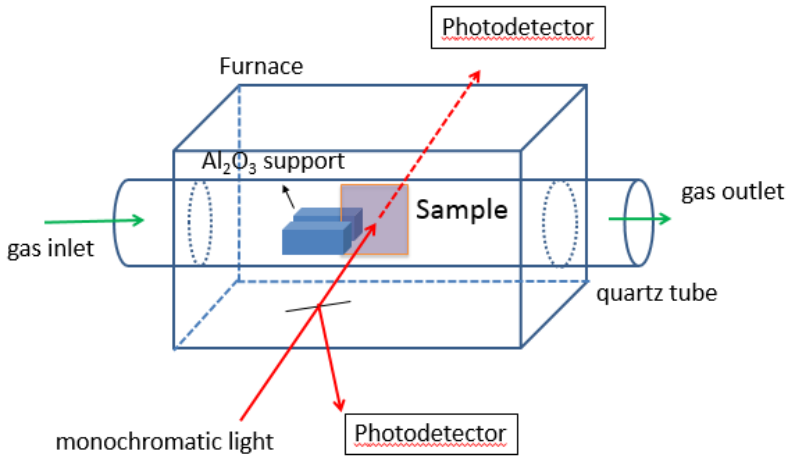

Figure 2-4 Schematic of the experimental setup for *in situ* optical transmission relaxation (OTR) measurements

A schematic diagram of the experimental setup for the *in situ* optical transmission measurement is shown in Fig.1. A beam of monochromated light (532 nm) was passed through the substrate and film which was vertically held in a quartz tube in a modified furnace, allowing the light beam to pass through the sample uninterrupted. Part of the beam was reflected and measured before passing through the film to remove ambient effects. Oxygen partial pressure was controlled by the use of N_2/O_2 gas mixtures. Changes in pO_2 were monitored with a residual gas analyzer recording the output gas of the setup(*2, 3*).

Reference

1. M. Pechini, Method of preparing lead and alkaline earth titanates and niobates and coating method using the same to form a capacitor. *United States Patent* (1969).
2. S. R. Bishop, J. J. Kim, N. Thompson, H. L. Tuller, Probing redox kinetics in Pr doped ceria mixed ionic electronic conducting thin films by in-situ optical absorption measurements *ECS Transactions* **45**, 491-495 (2012).
3. J. J. Kim, S. R. Bishop, N. J. Thompson, D. Chen, H. L. Tuller, Investigation of Nonstoichiometry in Oxide Thin Films by Simultaneous in Situ Optical Absorption and Chemical Capacitance Measurements: Pr-Doped Ceria, a Case Study. *Chem. Mat.* **26**, 1374-1379 (2014).

Chapter 3 Electrical property of Eu-CeO_2

3.1 Introduction

In this work, the potential for MIEC in $Eu_{0.2}Ce_{0.8}O_{2-\delta}$ has been examined. Maupoey *et al.* reported that Eu^{3+} can be reduced to Eu^{2+} in $Sr_2EuNb_{1-x}Ti_xO_6$ at pO_2 as high as 10^{-10} atm (*1*). Fabbri *et al.* considered that the electronic conductivity observed in $SrCe_{0.9}Eu_{0.1}O_3$ and $BaCe_{0.9}Eu_{0.1}O_3$ under oxidizing conditions is the result of the dopant redox couple Eu^{3+}/Eu^{2+} (*2*). While the synthesis and structure of Eu-doped ceria (ECO) have been studied in relation to the use of ECO as a luminescent material and a SOFC electrolyte in oxidizing conditions (*3*) (*4*), the electrical properties of ECO in reducing atmospheres have not been studied. In the present work, 20 mol% Eu-doped ceria (20ECO) was prepared, and the electrical properties were studied as a function of temperature and oxygen partial pressure using impedance spectroscopy.

As shown in section 1-3, for low pO_2 ceria releases oxygen by the following reduction reaction.

$$O_O^{\times} \leftrightarrow V_O^{\bullet\bullet} + 2e' + 1/2O_2(g) \qquad 3\text{-}1$$

In the case of Eu-doped ceria, Eu is reported to be trivalent for typical processing in oxidizing conditions (*5*). For reduction of Eu^{3+} to Eu^{2+}, the reduction reaction is written as

$$2Eu'_{Ce} + O_O^{\times} \leftrightarrow 2Eu''_{Ce} + V_O^{\bullet\bullet} + 1/2O_2(g) \qquad 3\text{-}2$$

As discussed in section 1-3 for electrical conductivity of multivalent acceptor doped ceria, for a mobility of electrons hopping on Eu cations (μ_{Eu}) that is similar to that for Ce (μ_{Ce}), an additional electronic conductivity (via small polaron hopping on Eu cations) will be observed in the intermediate pO_2 region (e.g. 10^{-10} atm – 10^{-20} atm) for a smaller enthalpy of reduction in Eq. 3-2 than that in Eq. 3-1, and thus serve to indicate the presence of multivalent Eu (3). In contrast, if $\mu_{Eu} >> \mu_{Ce}$, evidence for multivalency of Eu would be observed even if reduction is easier via Eq. 3-1. Lastly, if $\mu_{Eu} << \mu_{Ce}$, electrical conductivity arising from multivalency of Eu may not be observable.

3.2 Results and discussion

The XRD pattern of $Eu_{0.2}Ce_{0.8}O_{2-\delta}$ (20ECO) powder (Figure 3-1) confirms a single phase cubic fluorite structure. The lattice parameter is 5.429 ± 0.00014 Å, which is larger than that of pure ceria (5.411 Å) [JCPDS, 43-1002] and expected due to the larger ionic radius of Eu^{3+} (1.066 Å) as compared to Ce^{4+} (0.97 Å) (*6*).

Figure 3-2 shows the SEM micrograph of the surface of the 20ECO pellet with an average grain size about 1.6 ±0.2 μm estimated using the linear intercept method.

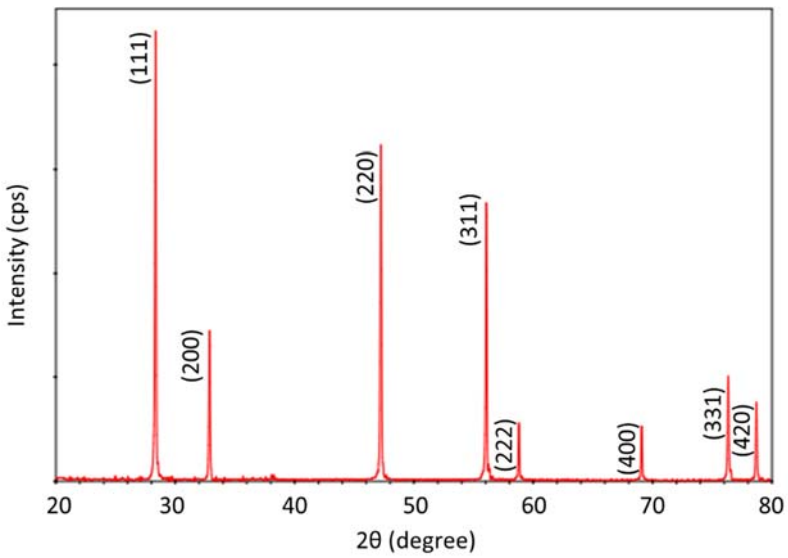

Figure 3-1 XRD pattern of $Ce_{0.8}Eu_{0.2}O_{1.95-\delta}$ powder measured using Cu-Kα radiation. Indices for the cubic fluorite structure are indicated.

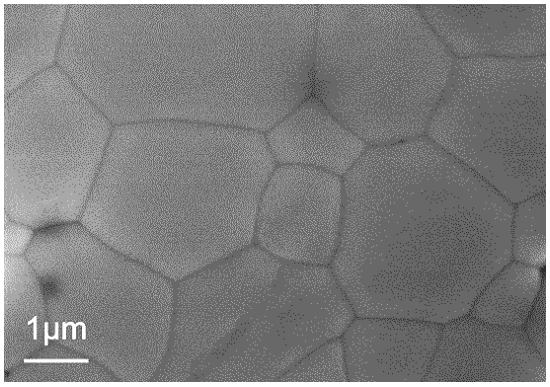

Figure 3-2 Scanning electron micrograph of the surface of the 20ECO pellet

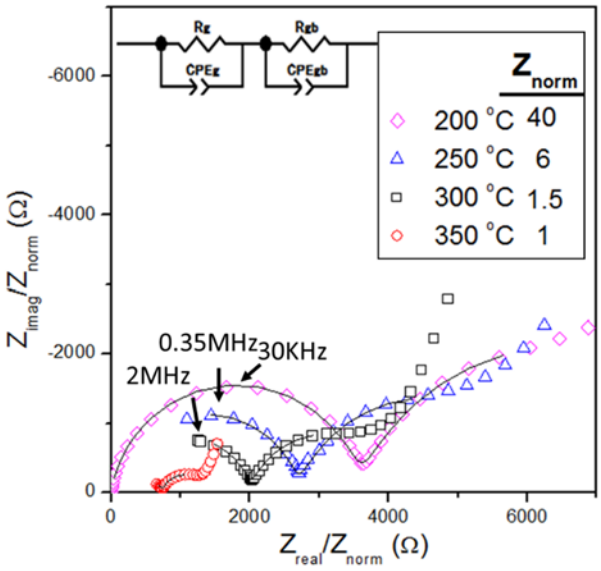

Figure 3-3 Impedance spectra of 20ECO (sample 2) in air at 200 – 350 °C (points) with the result of equivalent circuit fitting to high and intermediate frequency data also shown (solid lines). To facilitate

viewing of all spectra, the data are normalized by the factor shown in the legend.

Impedance spectra, measured at 200 °C – 350 °C in air for sample 2, are shown in Figure 3-3. Three arcs are observed, at high, intermediate, and low frequency. The impedance spectra for high and intermediate frequency arcs were fitted using the equivalent circuit model, consisting of resistors (R) in parallel with constant phase elements (CPE) approximating capacitors, as shown by the inset in the figure. The capacitance was determined from the fitted CPE parameters of Q and n using the following definition. Values of n were 0.9, close to 1, indicating close to ideal capacitance.

$$\mathrm{C} = (R^{1-n}Q)^{1/n} \qquad 3\text{-}3$$

Since the measured samples were not fully dense, a correction for porosity was used to estimate the conductivity for a fully dense sample. The following equation was used to determine resistance of a fully dense sample from the measured resistance of the pore/ECO composite sample (*7*),

$$R^{\mathrm{dense}} = R^{\mathrm{composite}}(1-f)^{m_f} \qquad 3\text{-}4$$

where f is the volume fraction of pores (11%) with $m_f = 3/2$ (*8*). The capacitance was corrected for porosity by assuming that the time constant of the impedance arc, RC, remained unchanged by the porosity correction, as performed in reference (*7*). The correction resulted in a 16% decrease of resistance and 19% increase of capacitance. In the following, values of capacitance, resistance, and conductivity are reported for a dense sample.

$$\tau = R^{\mathrm{dense}}C^{\mathrm{dense}} = R^{\mathrm{composite}}C^{\mathrm{composite}} \qquad 3\text{-}5$$

On the basis of the ratio of the capacitances, the high- and intermediate- frequency arcs in Fig. 3.3 are attributed to grain and grain boundary processes, respectively, as is typically observed in similar impedance measurements on large-grained samples (*9*). After correcting for the "stray capacitance" in the system (derived by measuring capacitance of setup with a known RC circuit), the capacitances of the high and low frequency arc were found to be on the order of 10^{-11} and 10^{-8} F, respectively. The former is in agreement with the expected capacitance from the relative permittivity of bulk acceptor-doped ceria (7-48 in this paper compared to ~55 in (*7*)) and the latter indicates the capacitance associated with the much thinner grain boundaries (*10*). Therefore, the high and intermediate frequency arcs in Fig. 3 are associated with grain and grain boundary conductivity, respectively. The low frequency arc, on the other hand, is most likely associated with electrode impedance expected for these two electrode measurements (*11*). The range in calculated values for grain permittivity may result from significant error associated with the estimate of stray capacitance. Therefore, a capacitance for a grain relative permittivity of 48 (the high end of the present results, and in best agreement with the literature) was used for the following calculations. The ratio of capacitance of grain and grain boundary can be expressed as:

$$\frac{C_g}{C_{gb}} = \frac{\varepsilon_g d}{\varepsilon_{gb} D} \qquad 3\text{-}6$$

where D is the grain size, d is the grain boundary thickness, and ε_g and ε_{gb} are dielectric constant

of grain and grain boundary (*12*). Assuming that the dielectric constants in the grain and grain boundary are the same, the thickness of the grain boundary is found to be 1.4 ± 0.2 nm which is similar with the results Souza *et al.* reported (~ 2 nm) (*13*).

With increasing temperature, the high frequency impedance decreases, with the corresponding time constant (RC) also decreasing. Thus, above ~350 °C, the high and intermediate frequency arcs are outside of the measurement frequency range capability of the instrument. However, the total sample resistance (sum of grain and grain boundary resistance) can be derived from the intercept of the high frequency part of the impedance spectra with the x-axis on the complex plane plot. For these higher temperature measurements, the reported conductivities are thus derived from the total sample resistance. The grain and total electrical conductivities, σ, were calculated using the following equation:

$$\sigma_g = \frac{1}{R} \times \frac{l}{A} \qquad 3\text{-}7$$

where *l* and A are the distance between the electrodes and the area of the electrodes, respectively. The grain boundary conductivity was then calculated from the following equation.

$$\frac{R_g}{R_{gb}} = \frac{\sigma_{gb} D}{\sigma_g d} \qquad 3\text{-}8$$

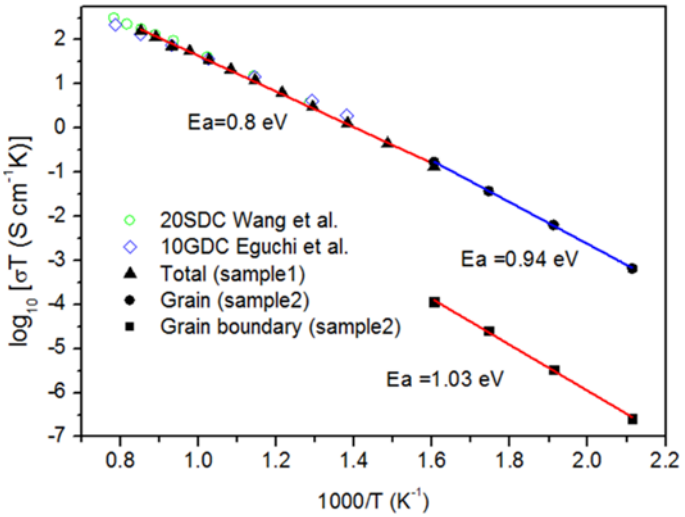

Figure 3-4 Arrhenius plot of grain, grain boundary and total conductivity for 20ECO samples 1 and 2, and compared with total conductivity of $Sm_{0.2}Ce_{0.8}O_{1.9}$ (20SDC) and $Gd_{0.1}Ce_{0.9}O_{1.95}$ (10GDC) (*14, 15*).

An Arrhenius plot of the grain, grain boundary, and total conductivity of 20ECO is shown in Figure 3-4. There is good agreement between literature and the present values for total conductivity, confirming that ionic conductivity is predominant in this high pO_2 region (*14, 15*). The temperature dependence of ionic conductivity is typically expressed by:

$$\sigma_i = \frac{\sigma_\circ}{T}\exp\left(-\frac{E_a}{kT}\right) \qquad 3\text{-}9$$

where σ_o is a constant and E_a is the activation energy including migration and dissociation enthalpy of oxygen vacancies. The activation energy for the total conductivity, derived from the slope of the plot in Figure 3-4, is also reported in the figure. E_a, for the grain conductivity (sample 2) is larger than that found for Gd and Sm doped ceria (~0.7 eV) (*13, 14*), despite their similar ionic radius with Eu. However, it is well known that at lower temperatures, defect interactions may occur which increase the migration energy, and is likely the case here. In fact, at higher temperatures, E_a for the total conductivity is lower (0.8 ± 0.01 eV), in agreement with reduced defect interactions with increasing temperature (*16*). Lastly, the much lower conductivity observed for grain boundaries as compared to grains is expected due to the former's typically ion-blocking nature (*17*).

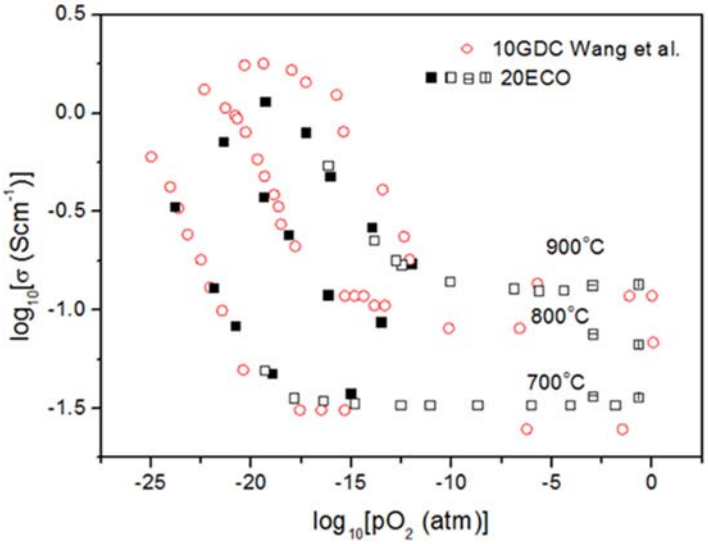

Figure 3-5 Temperature and pO_2 dependence of total conductivity of 20ECO (sample 1) compared with literature data for $Gd_{0.1}Ce_{0.9}O_{1.95}$ (10GDC) (*14*).

The total conductivity as a function of oxygen partial pressure is shown in Figure 3-5. As expected, the conductivity is almost constant with respect to changing pO_2 in high pO_2, consistent with ionic conductivity from fixed valence acceptor doping. With decreasing pO_2 (i.e. $< 9\times10^{-16}$ atm, at 700 °C), conductivity increases. In this region, the electron concentration increases following one of the reduction reactions, Equation 3-1 or 3-2, with a consequent increase in electron conductivity due to their much greater mobility as compared to oxygen vacancies. Assuming oxygen vacancy concentration is largely constant (i.e., constant ionic conductivity) over the pO_2 range in this work, the electronic conductivity can be obtained by subtracting the ionic contribution from the total conductivity (see Equation 3-10). The resulting oxygen partial pressure dependence of the electronic conductivity at 700 – 900 °C is shown in Figure 3-6

Equations shown in Table 3-1 were defined in section 1-3

Table 3-1 Definition of total conductivity σ_{tot}, electronic conductivity σ_e, electronic mobility μ_e, concentration of electrons n, equilibrium constant K_R

$\sigma_{tot} = \sigma_e + \sigma_i$	3-10

$\sigma_e = q\mu_e n$	3-11
$\mu_e = \frac{\mu_{o,e}}{T}\exp(-\frac{H_{m,e}}{kT})$	3-12
$n = \mathrm{pO_2^{-1/4}}\left(\frac{2K_R}{[\mathrm{A'_{Ce}}]}\right)^{1/2}$	3-13
$K_\mathrm{R} = [\mathrm{V_O^{\bullet\bullet}}]\cdot n^2\cdot \mathrm{pO_2}^{1/2} = K_0 \exp\frac{-H_\mathrm{r}}{kT}$	3-14

By substituting Equation 3-12, 13, 14 into Equation 3-11 and rearranging, the following dependence of electronic conductivity on pO_2 is obtained:

$$\log\sigma_e = \log C + (-1/4)\log P_{O_2} \qquad 3\text{-}15$$

Taking the thermally activated nature of small polaron hopping (*10*), *C* is an isothermal constant defined by

$$C = \frac{C'}{T}\exp\left(-\frac{H_{m,e}}{kT} - \frac{H_r}{2kT}\right) \qquad 3\text{-}16$$

where *C'* is a constant and $H_{m,e}$ is the electron migration enthalpy. A -1/4 slope is clearly observed in Figure 3-6, consistent with Equation 3-15 and the corresponding discussion of Equation 3-12. From fitting the data in Figure 3-6 with a slope of -1/4, the intercept of the plot, *C,* is obtained as shown by the inset in Fig. 3.6. From Equation 3-16, the activation energy for *C* is equal to $-\frac{H_{m,e}}{k} - \frac{H_r}{2k}$. Assuming that $H_{m,e}$ of 20ECO is the same as for ceria (0.4 eV) (10), an enthalpy of reduction of 4.2 ± 0.16 eV is obtained, a value within error to that of 15SDC (4.18 eV) reported by Lai et al. (18) and similar to 20GDC (4.0 eV) by Wang et al.(14). Additionally, the total conductivity dependence on pO_2 and temperature for 20ECO in Figure 3-5 is similar to the behavior of Gd doped ceria. The lack of an additional electronic contribution to conductivity expected for the reduction reaction of Eu (Equation 3-2), indicates that either the Eu electron hopping mobility is very low and/or Eu is not displaying significant multivalent behavior within the studied conditions of this work.

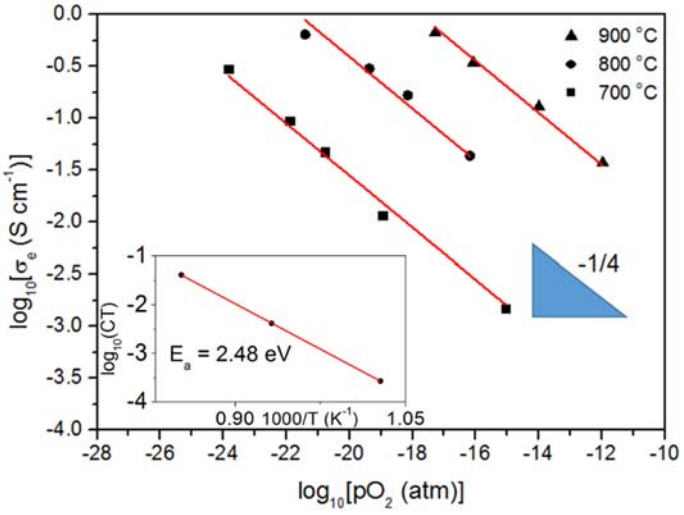

Figure 3-6 Electronic conductivity of 20ECO from 700 – 900 ºC as a function of pO_2 with -1/4 slopes, consistent with Equation 3-15, fit to the data. Inset reports the activation energy for intercept values (C) of the model fits.

3.3 Conclusion

20 mol% Eu-doped ceria ($Ce_{0.8}Eu_{0.2}O_{2-\delta}$) was prepared by a modified Pechini method. The electrical conductivity was studied by impedance spectroscopy at temperatures in the range 200 – 900 ºC and under controlled pO_2. Impedance spectroscopy was used to separate grain and grain boundary conductivity below 350 ºC. Eu-doped ceria showed a similar activation energy for electrical conductivity in reducing conditions to Sm- doped ceria reported in the literature. No evidence for multivalency of Eu was observed in electrical conductivity measurements over the studied range. Either the electron mobility of Eu small polarons is too low or Eu is not displaying multivalency in the studied range.

Reference

1. Z. Maupoey, M. T. Azcondo, U. Amador, A. Kuhn, J. C. Perez-Flores, J. R. de Paz, N. Bonanos, F. Garcia-Alvarado, The role of the Eu^{3+}/Eu^{2+} redox-pair in the electrical properties of $Sr_2EuNb_{1-x}Ti_xO_{6-\delta}$ oxides. *J Mater Chem* **22**, 18033-18042 (2012).
2. E. Fabbri, T. K. Oh, S. Licoccia, E. Traversa, E. D. Wachsman, Mixed Protonic/Electronic Conductor Cathodes for Intermediate Temperature SOFCs Based on Proton Conducting Electrolytes. *Journal of the Electrochemical Society* **156**, B38-B45 (2009).
3. Z. Wang, Z. Quan, J. Lin, Remarkable changes in the optical properties of CeO_2 nanocrystals induced by lanthanide ions doping. *Inorg Chem* **46**, 5237-5242 (2007).
4. A. K. Baral, V. Sankaranarayanan, Ionic Transport Properties in Nanocrystalline $Ce_{0.8}A_{0.2}O_{2-\delta}$ (with A = Eu, Gd, Dy, and Ho) Materials. *Nanoscale research letters* **5**, 637-643 (2010).
5. W. Y. Hernandez, O. H. Laguna, M. A. Centeno, J. A. Odriozola, Structural and catalytic properties of lanthanide (La, Eu, Gd) doped ceria. *J. Solid State Chem.* **184**, 3014-3020 (2011).
6. R. D. Shannon, Revised effective ionic-radii and systematic studies of interatomic distances in halides and chalcogenides. *Acta Crystallogr. Sect. A* **32**, 751-767 (1976).
7. N. H. Perry, T. C. Yeh, T. O. Mason, Temperature Dependence of Effective Grain Core/Single Crystal Dielectric Constants for Acceptor-Doped Oxygen Ion Conductors. *Journal of the American Ceramic Society* **94**, 508-515 (2011).
8. D. S. Mclachlan, M. Blaszkiewicz, R. E. Newnham, Electrical-Resistivity of Composites. *Journal of the American Ceramic Society* **73**, 2187-2203 (1990).
9. H. L. Tuller, S. R. Bishop, Point Defects in Oxides: Tailoring Materials Through Defect Engineering. *Annu Rev Mater Res* **41**, 369-398 (2011).
10. H. L. Tuller, A. S. Nowick, Small polaron electron-transport in reduced CeO_2 single-crystals. *J. Phys. Chem. Solids* **38**, 859-867 (1977).
11. J. E. Bauerle, Study of Solid Electrolyte Polarization by a Complex Admittance Method. *J. Phys. Chem. Solids* **30**, 2657-& (1969).
12. N. J. Kidner, N. H. Perry, T. O. Mason, E. J. Garboczi, The brick layer model revisited: introducing the nano-grain composite model. *Journal of the American Ceramic Society* **91**, 1733-1746 (2008).
13. E. C. C. Souza, W. C. Chueh, W. Jung, E. N. S. Muccillo, S. M. Haile, Ionic and Electronic Conductivity of Nanostructured, Samaria-Doped Ceria. *Journal of the Electrochemical Society* **159**, K127-K135 (2012).
14. S. R. Wang, T. Kobayashi, M. Dokiya, T. Hashimoto, Electrical and ionic conductivity of Gd-doped ceria. *Journal of the Electrochemical Society* **147**, 3606-3609 (2000).
15. K. Eguchi, T. Setoguchi, T. Inoue, H. Arai, Electrical-Properties of Ceria-Based Oxides and Their Application to Solid Oxide Fuel-Cells. *Solid State Ion.* **52**, 165-172 (1992).
16. M. Mogensen, N. M. Sammes, G. A. Tompsett, Physical, chemical and electrochemical properties of pure and doped ceria. *Solid State Ion.* **129**, 63-94 (2000).
17. X. Guo, J. Maier, Grain boundary blocking effect in zirconia: A Schottky barrier analysis. *Journal of the Electrochemical Society* **148**, E121-E126 (2001).
18. W. Lai, S. M. Haile, Impedance spectroscopy as a tool for chemical and electrochemical analysis of mixed conductors: A case study of ceria. *Journal of the American Ceramic Society*

88, 2979-2997 (2005).

Chapter 4 Characterization of Mn-CeO_2 and Fe-CeO_2

4.1 Introduction

By doping ceria with transition metal ions (e.g. Fe^{3+}, Mn^{3+}), the oxygen vacancy concentration may be increased. Additionally, mixed-valence Fe or Mn in ceria may enhance the electronic conductivity due to reduction of Fe^{3+} to Fe^{2+} or Mn^{3+} to Mn^{2+} in low partial pressures of oxygen, thus acting as an additional redox couple besides $Ce^{4+/}Ce^{3+}$. Such MIEC behavior is known to improve cathode oxygen exchange kinetics in SOFCs (*1*) and previous reports have shown that Ce–Fe mixed oxides have high catalytic activity for the oxidation of CO or hydrocarbons (*2-4*). Lv et al. also found that Fe doped ceria is a promising candidate an SOFC anode operating on methane fuel (*5*). Shin reported by using $Ce_{0.6}Mn_{0.3}Fe_{0.1}O_2$ (CMF) and $La_{0.}6Sr_{0.4}Fe_{0.9}Mn_{0.1}O_3$ as the anode, the power density was as high as $1Wcm^{-2}$ at 800 °C by flowing C_3H_8 or $C_4H_{10.(6)}$

As shown in Figure 1-7 for Pr doped ceria, the increase of electronic conductivity is dependent on the concentration of Pr dopant. Since the properties and applications of Mn-CeO_2 are expected to be heavily influenced by dopant concentration and corresponding defect chemistry, the solubility limit of Mn in CeO_2 must be investigated. There are mixed reports of the Mn or Fe solubility limit, as investigated for different processing methods as shown in Table 2.1 and 2.2. Perez-Omil et al. (*7*), Machida et al. (*8*), Delimaris et al. (*9*) have reported a relatively high solubility limit of Mn and Li et al. (*10*), Singh et al. (*11*), Lv et al. (*12*) have reported a relatively high solubility limit of Fe in CeO_2 using a low calcination temperature. However, for its application as an SOFC anode material, phase stability at high temperature is very important, where typical SOFC fabrication temperatures exceed 1000 °C. In addition, for powders calcined at low temperature, XRD patterns are not highly reliable due to the low signal to noise ratio and with potential overlap of broad peaks with secondary phase peaks. Zhou et al. (*13*) and Jia et al. (*14*) fabricated samples by the Pechini method at 700 °C and 900 °C and found the solubility limit of Mn in CeO_2 to be between 10% to 20%. Kang et al. reported the solubility limit to be between 5% and 10%, after a high calcination temperature (*15*). However, their work was limited to phase analysis by XRD, which may be limited in detecting small amounts of second phases. Zhang et al. (*16*) reported there is insignificant solubility of Fe in CeO_2 for calcining at 1200 °C, and less than 1% for a 1500 °C calcination by the solid-state reaction method. Though the solid-state reaction method is widely used for the preparation of ceramic compounds, because of its low cost and simplicity, poor compositional homogeneity may occur leading to formation of secondary phases. The Pechini method, which uses citric acid as a chelating agent in combination with ethylene glycol, can preserve a highly homogeneous distribution of metal ions in calcined precursors as well as producing high purity material. For example, Shi et al. found that single phase $La_{0.85}Sr_{0.15}Ga_{0.8}Mg_{0.2}O_{2.825}$ powder could be synthesized by the Pechini method, but not by the solid-state reaction method (*17*). In the present work, the solubility limit of Mn or Fe in ceria was investigated using powders synthesized by the Pechini method, calcined at 1200 °C, and characterized

by XRD and Raman spectroscopy.

Table 4.1 Solubility limit of Mn in CeO_2 by various methods and calcination temperature

Solubility limit	Synthesis method	Calcination temperature (℃)	Refs.
<20%	Pechini	700	(*13*)
>15%	Coprecipitation	500	(*7*)
50-75%	Coprecipitation	450	(*8*)
5-10%	Coprecipitation	1300	(*15*)
>10%	Pechini	900	(*14*)
25%	Urea-nitrate combustion	500	(*9*)

Table 4.2 Solubility limit of Fe in CeO_2 by various method and calcination temperature

Solubility limit	Synthesis method	Calcination temperature (℃)	Refs.
15%	Hydrothermal	220	(*10*)
33%	Sonication	600	(*3*)
>20%	Citrate	600	(*12*)
<30%	Coprecipitation	600-900	(*2*)
0	Solid-state reaction	1200	(*16*)
<1%	Solid-state reaction	1500	(*16*)

4.2 Results and discussion

4.2.1 XRD and Raman

Figure 4-1 and Figure 4-2 show the XRD patterns for x mol% fraction of Mn and Fe to CeO_2 (x=3-50) powders prepared in this study. For $x \geq 10\%$, two phase mixtures of Mn_3O_4 /CeO_2 and Fe_2O_3 /CeO_2 were clearly observed. Figure 4-3 shows the XRD pattern of x mol% of Mn_3O_4 mixed with CeO_2 and very similar with the patterns of the powders prepared by the Pechini method. This indicates that the sensitivity limit of XRD is about 10 mol% Mn which also explain why Kang et al. observed the solubility of Mn in CeO_2 to be 5-10% (*15*). In Figure 4-4 and Figure 4-5, the lattice parameter of CeO_2 does not exhibit any dependence on Mn or Fe concentration within error, indicating low solubility of Mn or Fe in the measured range, as discussed below.

The sensitivity of Raman spectroscopy to bond strength and crystal symmetry provides an additional tool for structural analysis. Cubic fluorite structure metal oxides have only a single allowed Raman mode equal to 465 cm^{-1} for CeO_2 (*18*). In Figure 4-6, peaks at 313.1, 369.6, 654.8 cm^{-1} which belong to Mn_3O_4 were observed for all the Mn containing powders (*19*). Fe_2O_3, on the other hand, belongs to the D^6_{3d} crystal space group with seven Raman modes (225, 247, 293, 299, 412, 498, and 613 cm^{-1}), a reflection of its much lower symmetry (*20*). In Figure 4-7, peaks of Fe_2O_3 at approximately 225, 247, 293, 412, and 613 cm^{-1} were observed for all the Fe containing powders. The expected peaks at 299 and 498 cm^{-1} were not clearly observed because of overlap with the much stronger 293 and 465 cm^{-1} peaks, respectively.

The above results clearly demonstrate that the solubility of Mn or Fe in CeO_2 is less than the minimum studied Fe and Mn contents, 3 mol%, for the studied conditions as discussed below. Though the XRD data in Figure 4-1 and Figure 4-2 did not show a second phase for less than 10 mol% Mn or Fe, this low concentration of Mn or Fe appears to be below the detection limit for the instrument. Due to the difference in ionic radius between Mn^{3+} (0.645 Å) and Ce^{4+} (0.97 Å), the lattice parameters in Figure 4-4 and Figure 4-5 are expected to dramatically decrease upon Mn or Fe substitution for Ce (*21*). This is clearly not the case, indicating little to no solubility of Mn or Fe in CeO_2 and the addition of Fe did not increase the solubility limit of Mn in CeO_2. The existence of Mn_3O_4 and Fe_2O_3 second phase by Raman spectroscopy provides additional, clear confirmation of low Mn solubility in CeO_2. A key point to mention here is that the use of a relatively long wavelength laser helped to avoid light absorption by the reddish Mn_3O_4 or Fe_2O_3, thereby maintaining a significant response. Lastly, the characteristic oxygen vacancy peak at approximately 570 cm^{-1} for CeO_2 (*18*) was not observed here, indicating a very low oxygen vacancy concentration, expected for undoped ceria heat treated in air.

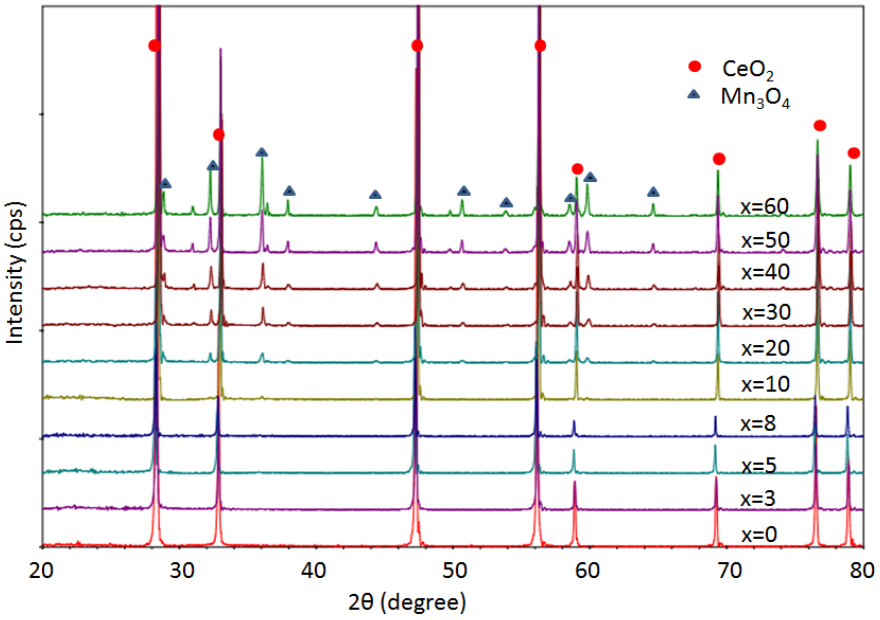

Figure 4-1 XRD patterns of x mol% Mn-CeO_2 (x=3-60) powder. Peaks for fluorite structured CeO_2 [PDF 00-034-0394 (RDB)] and hausmannite (Mn_3O_4) [PDF 01-089-4837 (RDB)] are indicated.

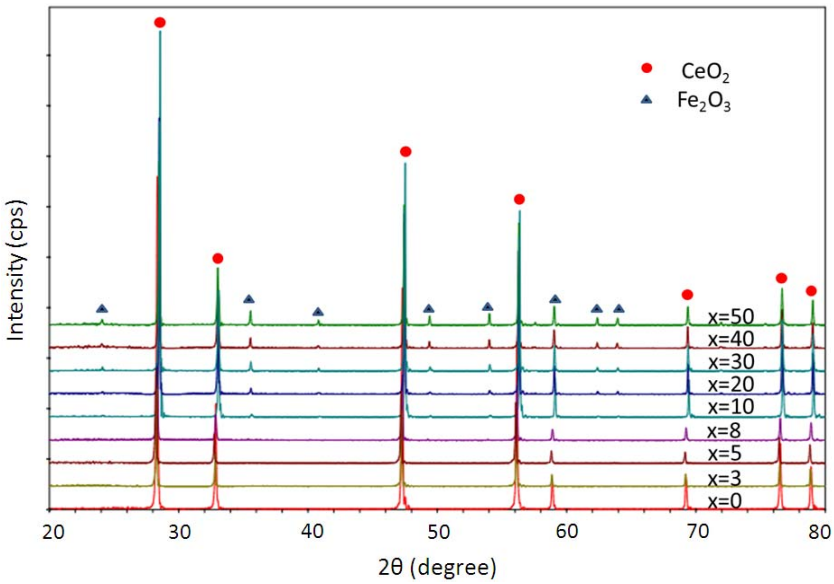

Figure 4-2 XRD patterns of x mol% Fe-CeO_2 (x=3-50) powder. Peaks for fluorite structured CeO_2 [PDF 00-034-0394 (RDB)] and hematite structured Fe_2O_3 [PDF 01-084-0306 (RDB)] are indicated.

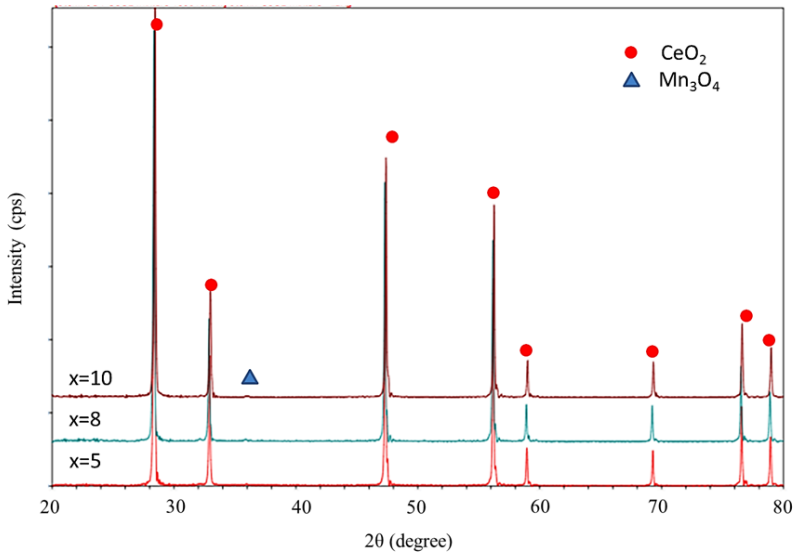

Figure 4-3 XRD patterns of x mol% Mn_3O_4 and CeO_2 (x=5-8) mixed powder (no calcination treatment). Peaks for fluorite structured CeO_2 [PDF 00-034-0394 (RDB)] and hausmannite (Mn_3O_4) [PDF 01-089-4837 (RDB)] are indicated.

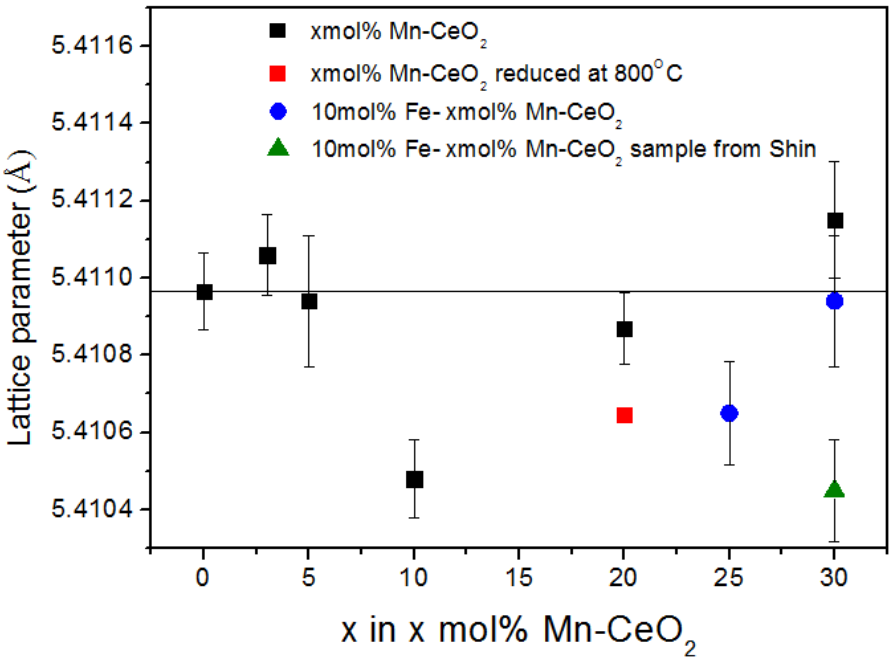

Figure 4-4. Lattice parameter of Mn-CeO_2 and Fe-Mn-CeO_2 derived from XRD versus Mn concentration. The lattice parameter does not show any trend with Mn content, note the very small range of lattice parameter on the y-axis. Red square: reduced in 0.2% H_2 at 800 °C, green triangle: 10mol% Fe-30mol% Mn-CeO_2 sample from Shin at Ishihara`s lab.

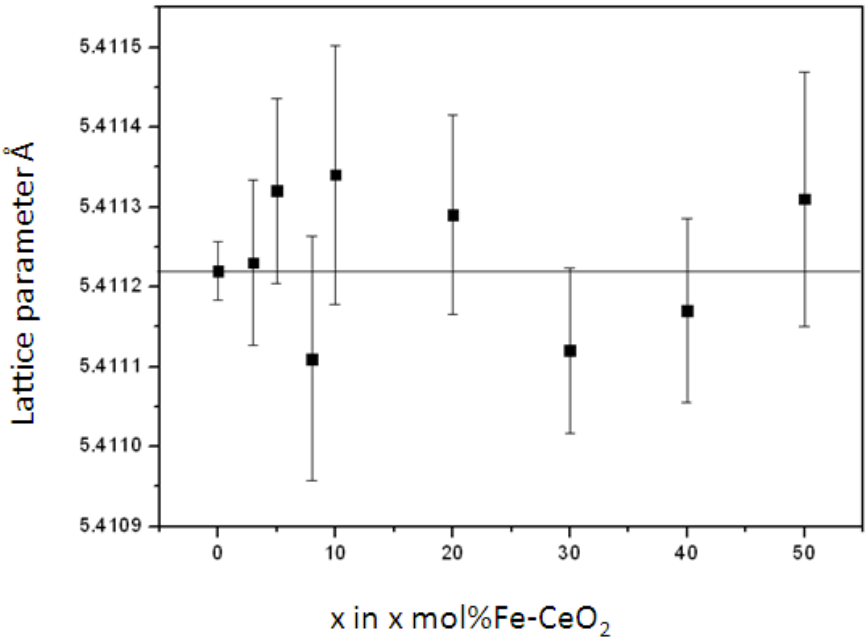

Figure 4-5 Lattice parameter of CeO_2 derived from XRD versus Fe concentration. Within experimental error, the lattice parameter does not show any dependence on Fe content.

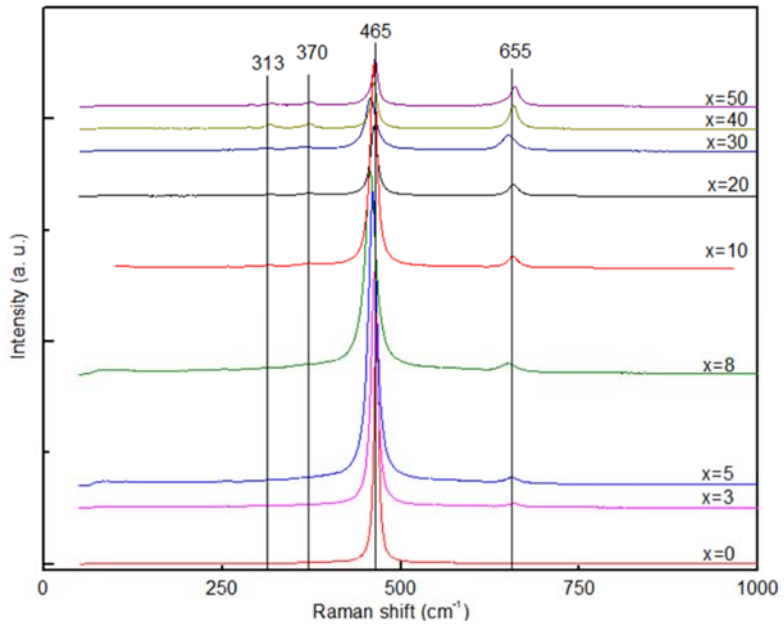

Figure 4-6 Raman spectra of x mol% Mn-CeO_2 (x=3-50). For all compositions containing Mn, a second phase peak corresponding to Mn_3O_4 is observed. Peaks corresponding to Mn_3O_4 are indicated by vertical lines at 313.1, 369.6, 654.8cm^{-1} as well as for ceria at 465 cm^{-1}.

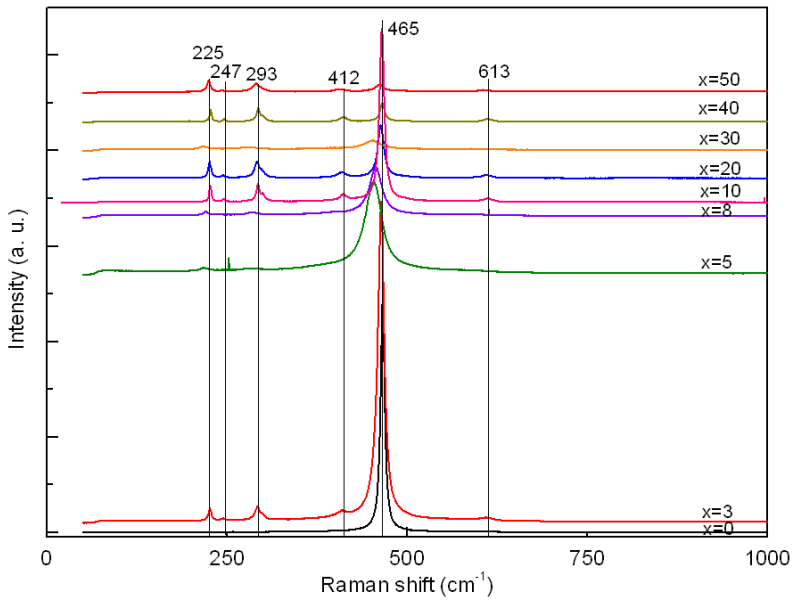

Figure 4-7. Raman spectra of x mol% Fe-CeO_2 (x=3-50). For all compositions containing Fe, a second phase peak corresponding to Fe_2O_3 is observed. Peaks corresponding to Fe_2O_3 and CeO_2 are indicated by 225, 247, 293, 412, and 613 cm^{-1} and 465 cm^{-1}, respectively.

A strong reason for the low solubility of Mn or Fe in CeO_2 is that Mn^{3+} or Fe^{3+} is too small to substitute for Ce^{4+}. Therefore, we considered a novel approach of increasing the Mn or Fe radius through reduction of Mn^{3+} to Mn^{2+} (radius = 0.96 Å) and Fe^{3+} to Fe^{2+} (radius = 0.92 Å), thereby providing a much closer match in Mn to Ce radii. 3 mol% and 10 mol% Mn-CeO_2 and Fe-CeO_2 powders were annealed in flowing humidified H_2 at 1100 °C after the calcination process at 650 °C in air. Mn_3O_4 was reduced to MnO, as shown in Figure 4-8, with Mn oxide still existing as a second

phase. The lattice parameter of 20 mol% Mn-CeO_2, which reduced in 0.2% H_2 at 800 °C, was calculated and shown in Figure 4-4. The change of lattice parameter is very small indicating that the solubility limit of Mn in CeO_2 was not changed by the reduction. An interesting result was obtained, instead of forming Fe doped CeO_2, a perovskite $CeFeO_3$ phase was observed by XRD, as shown in Figure 4-9, and in agreement with (*22, 23*). Upon heat treatment at 1200 °C in air, the MnO and $CeFeO_3$ phase converted back to the Mn_3O_4 and Fe_2O_3. The observed phase changes for the above temperature condition is thus sufficient to form additional phases, and therefore phase formation (i.e. single phase Mn doped ceria) is not expected to be limited by slow cation diffusion.

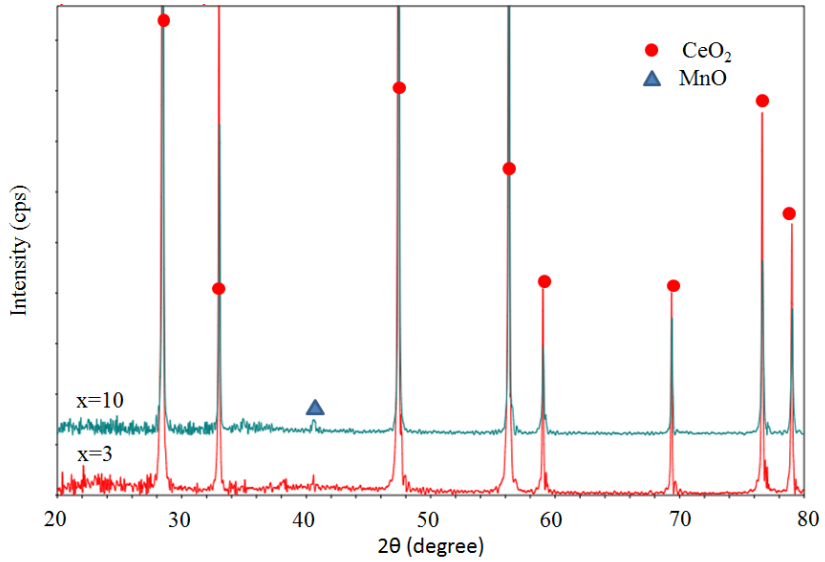

Figure 4-8 XRD patterns for 3 mol% and 10 mol% Mn-CeO_2 powders annealed in wet H_2 at 1100°C. A second, MnO [PDF 99-000-2296], phase is clearly observed for 10 mol% Mn-CeO_2

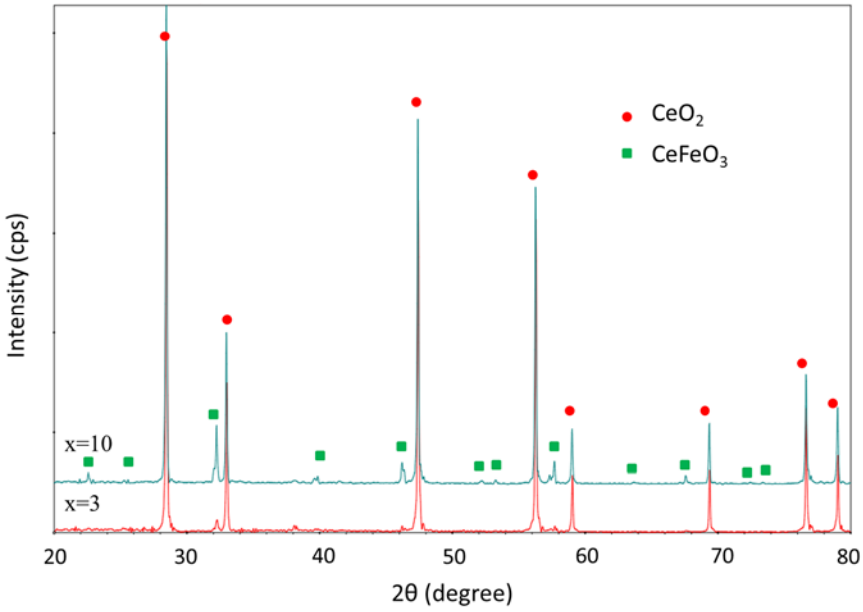

Figure 4-9 XRD patterns for 3 mol% and 10 mol% Fe-CeO_2 powders annealed in wet H_2 at 1100 ℃. A second, $CeFeO_3$ [PDF 00-022-0166 (RDB)], phase is clearly observed for both compositions.

Kim (*24*) argues that the solubility limit of a solute depends on the elastic energy, which is introduced in the lattice due to differences in ionic radius. By co-doping with a larger dopant, La, the

difference between dopant and cerium may be reduced and thus increase the solubility of Mn. Figure 4-10 shows that lattice parameters of .La-CeO2 (*25*) compare with 10 mol% Mn-La-doped CeO_2.

The lattice parameters of x mol% La-CeO_2 were calculated according to Equation 4-1(*26*).

$$a = \frac{4}{\sqrt{3}}[xr_{La^{3+}} + (1-x)r_{Ce^{4+}} + (1-0.25x)r_{O^{2-}} + 0.25xr_{V_O}] \times 0.9971 \qquad 4\text{-}1$$

The radii of La^{3+}, Ce^{4+}, O^{2-}, and oxygen vacancy in eight fold coordination are 1.16 Å, 0.97 Å, 1.38 Å, and 1.164 Å, respectively (*26*).

The lattice parameters of Mn-La co-doped CeO_2 are obviously smaller than La-CeO_2, indicating that some amount of the smaller Mn dopant is in solution.

To calculate the concentration of Mn in the solution of x mol% La 10 mol% Mn CeO_2, Equation 4-1 was modified as:

$$a = \frac{4}{\sqrt{3}}[xr_{La^{3+}} + yr_{Mn^{3+}} + (1-x-y)r_{Ce^{4+}} + (1-0.25(x+y))r_{O^{2-}} + 0.25(x+y)r_{V_O}] \times 0.9971 \qquad 4\text{-}2$$

The results are shown in Table 4-3. For 10 mol% Mn-CeO_2, the solubility limit of Mn is increased by co-doping La and reaches an apparent maximum in solubility at 10 mol% La.

On the other hand, Zr was also co-doped in Mn-CeO_2. Zr is known to induce a contraction in the CeO_2 lattice (*27*). The solubility limit of Mn in CeO_2 is not increased by co-doping Zr given that the lattice parameter nearly did not change (Figure 4-11), indicating that for an increased solubility of the small Mn cation, a larger dopant in ceria is needed.

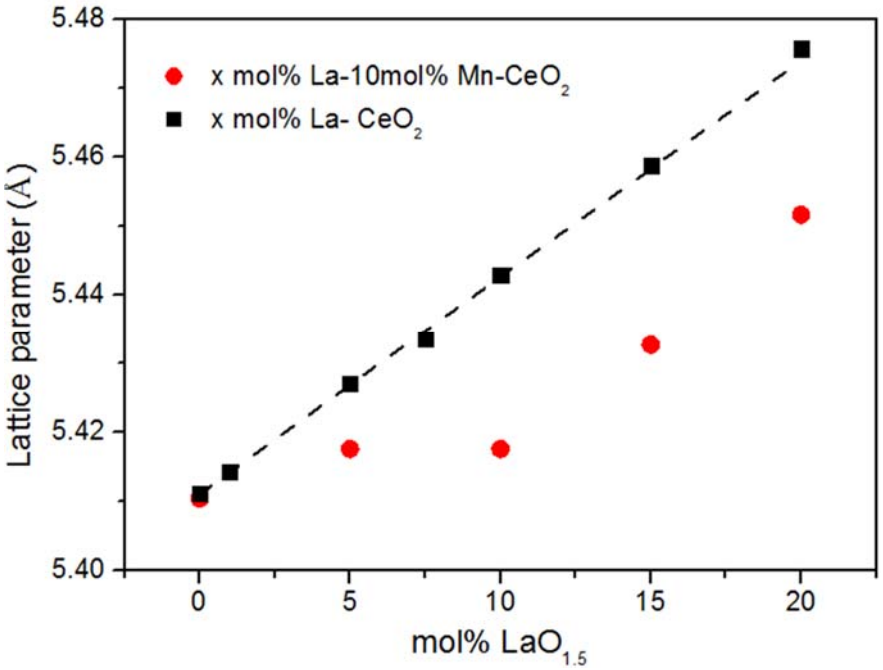

Figure 4-10 Lattice paramter of xmol% La-10 mol% Mn-CeO_2 and xmol% La-CeO_2 (obtained from (*25*)) versus La concentration

Table 4-3 Estimated Mn solubility in CeO_2 calculated from lattice parameter (Eq. 4-2) with different amount of co-doped La.

La mol%	Mn mol%
5	1.1
10	2.9
15	2.9
20	2.6

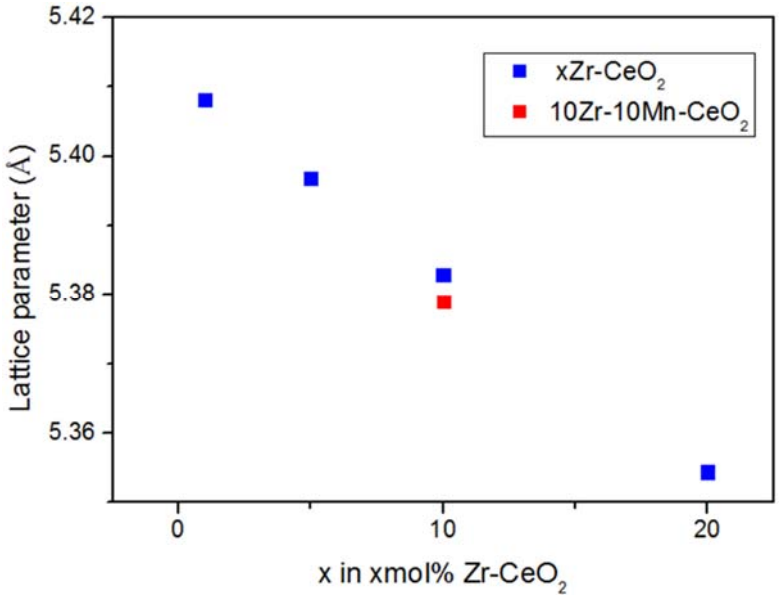

Figure 4-11 Lattice parameter of x mol% Zr-CeO_2 and versus Zr concentration (*28*) (red square:10 mol%Zr-10 mol% Mn-CeO_2)

4.2.2 SEM EDX

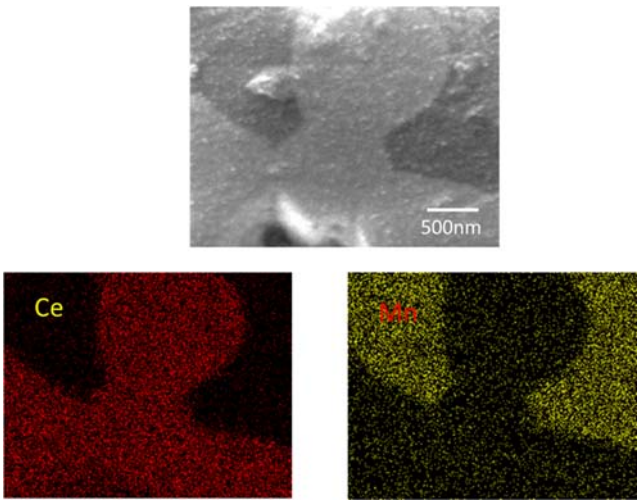

Figure 4-12 SEM and EDX image of 20%Mn-CeO_2 (upper figure: SEM, under figures: EDX, Ce: red, Mn: yellow)

Figure 4-12 shows SEM and EDX images of the as sintered 20%Mn-CeO_2 pellet (i.e. cooled from high temperature in air). Clearly, two separate phases are observed and are assigned based on EDX results to CeO_2 phase and Mn oxide phase as indicated in the figure.

4.2.3 TGA

20 mol% Mn-CeO_2 was measured by TGA. Assuming Mn is all 3+ in air (consistent with the predicted phase diagram in Fig. 4-13) and the sample is a mixture of *a* mol of $Ce_{1-x}Mn_xO_{2-0.5x}$ and *b* mol of $MnO_{1.5}$, the total mass can be expressed by:

$$m_{sample} = a((1-x)\,M_{Ce}+xM_{Mn}+(2-0.5x)M_O)+b(M_{Mn}+1.5M_O) \quad 4\text{-}3$$

where M_{Ce}, M_{Mn} and M_O are atomic weight of Ce, Mn and O. The cation ratio of Ce and Mn is 4:1, so:

$$\frac{a(1-x)}{ax+b} = \frac{4}{1} \quad 4\text{-}4$$

The mass change measured upon reduction of $MnO_{1.5}$ from air to 0.2% H_2 at 800 °C can be predicted. This mass loss is much greater than the reduction of ceria, according to reference (*29*), for a similar pO_2 step, $\Delta\delta$ in pure $CeO_{2-\delta}$ is about 0.002. The mass change for the phase change of Mn oxide, viz. from $MnO_{1.5}$ to MnO, was separately confirmed without the presence of ceria as shown by Figure 4-13. Then mass loss can be expressed as:

$$m_{\text{loss from air to 0.2\% H2}} = 0.5bM_O. \quad 4\text{-}5$$

Combining Equation 4-3, 4-4 and 4-5, x (the fraction of Mn in solution) is calculated to be 0.074, 0.071, and 0.08 for three 20 mol% Mn-CeO_2 samples prepared independently. The above calculation assumes the Mn in solution of ceria is not changing valence. This result is clearly in contradiction to the above XRD and Raman measurements.

Turning to the change in mass measured in very reducing conditions, using the δ at 800 °C and 900 °C in 0.2% H_2 as a reference point, $\Delta\delta$ of $Ce_{1-x}Mn_xO_{2-0.5x-\delta}$ is calculated and compared with undoped and Gd and Y doped CeO_2 (interpolated from the literature) as shown for two temperatures in Figure 4-15 and Figure 4-16. The measured $\Delta\delta$ of $Ce_{1-x}Mn_xO_{2-0.5x-\delta}$ is very similar to the Y and Gd doped and undoped CeO_2. First, the similar change in δ indicates that no more of the second phase MnO is changing valence significantly, consistent with the phase diagram. Additionally, the Mn that may be in solution with ceria may change valence in this region. Indeed, there is a slightly larger non-stoichiometry in very reducing conditions for the $Ce_{1-x}Mn_xO_{2-0.5x-\delta}$ which may arise from reduced Mn, though at present, these results are inconclusive.

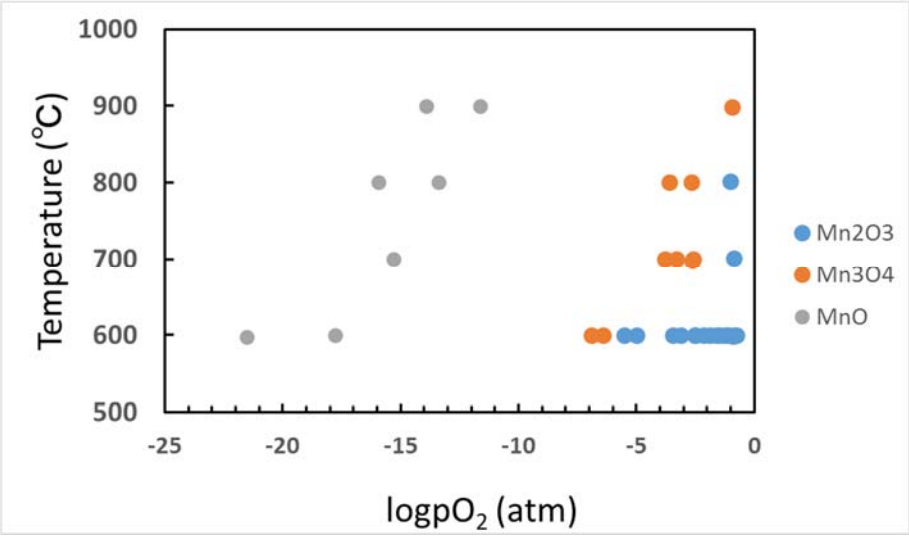

Figure 4-13 Phase diagram of Mn oxide

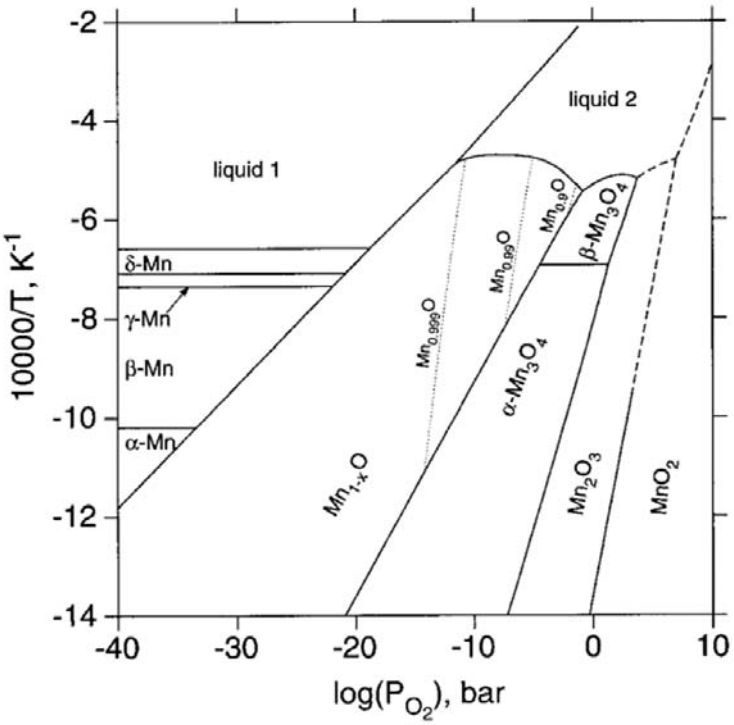

Figure 4-14 Calculated phase diagram of the Mn-O system (obtained from (*30*))

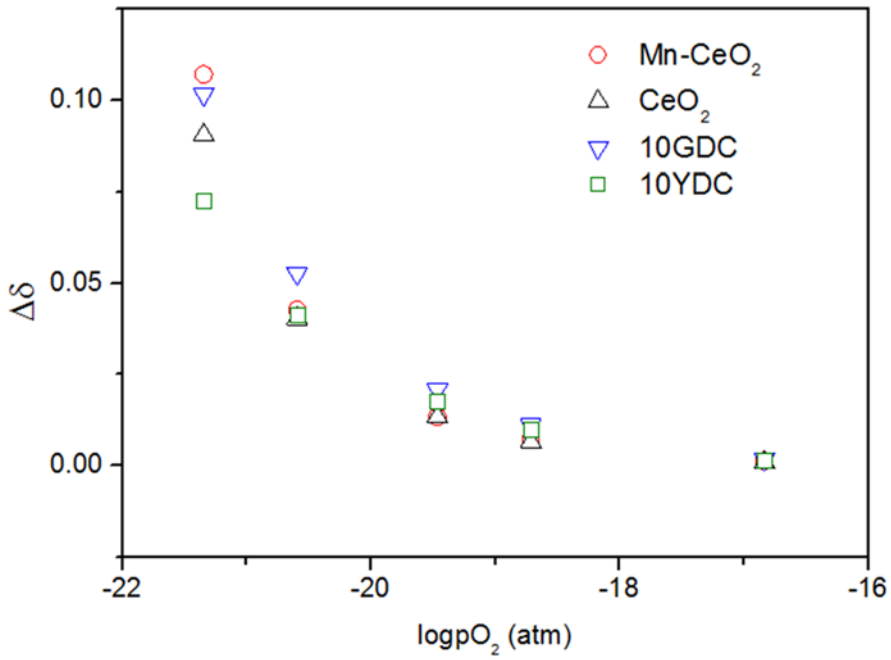

Figure 4-15 Δδ of $Ce_{1-x}Mn_xO_{2-0.5x-\delta}$ as a function of pO_2 at 800 °C for Mn-CeO_2, CeO_2 (*29*), 10GDC (*31*), 10YDC (*32*)(reference point: 0.2%H_2, logpO_2=-15.9)

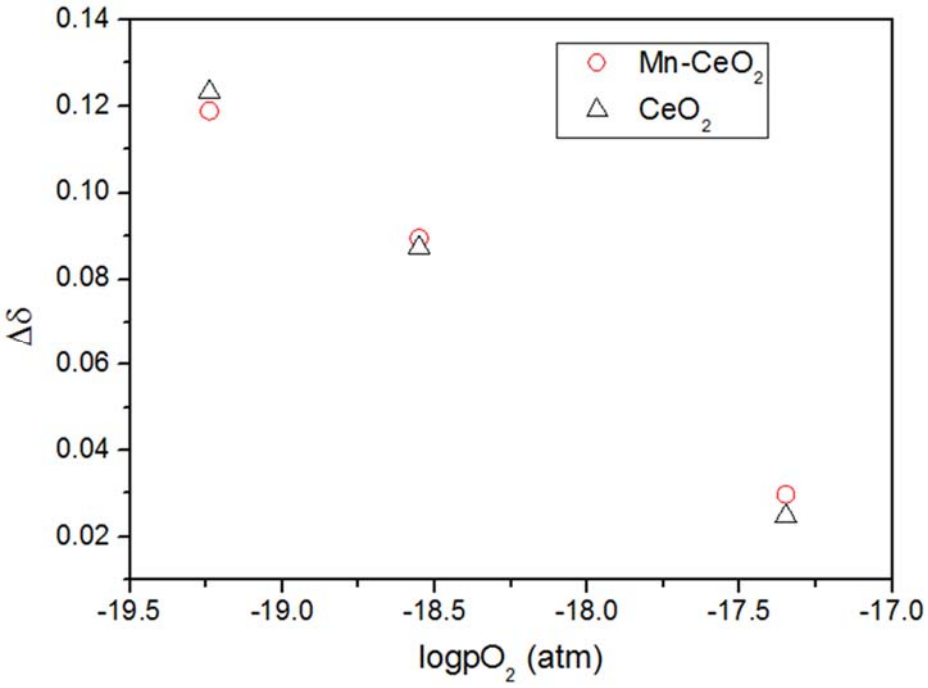

Figure 4-16 Δδ of $Ce_{1-x}Mn_xO_{2-0.5x-\delta}$ as a function of pO_2 at 900 °C for Mn-CeO_2, CeO_2 (*29*), (reference point: 0.2%H_2, logpO_2=-16.7)

4.2.4 Conductivity

By the same method for 20ECO, conductivity of 20 mol% Mn-CeO_2 was measured as a function of pO_2 and temperature, and the results are shown in Figure 4-18. The Impedance spectra of 20 mol%

Mn-CeO_2 at 750 °C in air is shown in Figure 4-17, the high frequency arc was used to calculate the bulk conductivity discussed here. There is a slope change from high T to low T. At low temperature low pO_2 region, the slope is expected to be close to -1/4 because the vacancy concentration, which is largely generated by acceptors (e.g. impurities or Mn dopant, assuming no change Mn valence), is constant. Therefore, $[\mathrm{Mn}'_{\mathrm{Ce}}] \approx 2[\mathrm{V}_{\mathrm{O}}^{\bullet\bullet}] \approx$ const. By substituting Equation 4-7, 8 into Equation 4-6, one can find Equation 4-9, the activation energy is equal to $-\frac{H_{m,e}}{kT} - \frac{H_r}{2kT}$ Assuming that $H_{m,e}$ of 20 mol% Mn-CeO_2 is the same as for ceria (0.4 eV) (*33*) a reduction enthalpy of 4.5 eV is obtained by fitting the lower three temperatures, which is almost the same with GDC (4.5 eV) (*34*). At high temperature, because the concentration of dopant is so small, that we can ignore this reaction, and the slope is close to -1/6 just like pure ceria, $n = 2[V_O^{\cdot\cdot}]$, then one finds Equation 4-10, the activation energy is equal to $-\frac{H_{m,e}}{kT} - \frac{H_r}{3kT}$. The reduction enthalpy from fitting the highest three temperatures, is 5.07 eV which is slightly higher than pure ceria (4.7 eV) (*33*). The Arrhenius plot of conductivity in air is shown in Figure 4-20.

Turning to the high pO_2 case (air) a change in slope of the Arrhenius plot in Figure 4-19 is observed from low T to high T. At high T, the conductivity is almost the same with undoped ceria data from literature. From the slope at low T, we can calculate the migration enthalpy for vacancy migration assuming the conductivity is dominated by oxygen vacancies whose concentration is fixed by acceptor dopant (e.g. Mn^{3+}). The migration energy for vacancies is found to be about 1.1 eV. As shown in Figure 4-20, activation energy is higher for dopants with a large radius mismatch with ceria (as also discussed in the introduction). Therefore, the larger activation energy for vacancy migration in Mn-CeO_2 found here is expected. Furthermore, using the activation energy as an indicator of dopant concentration in solution, examination of Figure 4-20 shows that the high activation energy corresponds to either a very small dopant concentration (e.g. less than 0.1% for Yb), or a very large dopant concentration in solution. Since, at high temperature, conductivity approached that of undoped ceria, we expect that the dopant in solution corresponds with the former case, i.e. a low solubility of Mn, in agreement with the above XRD and Raman studies.

Table 4-4 Definition of electronic conductivity σ_e, electronic mobility μ_e, equilibrium constant K_R (similar equations and their discussion can be found chapter 3)

$\sigma_e = q\mu_e n$	4-6
$K_R = [\mathrm{V}_{\mathrm{O}}^{\cdot\cdot}] \cdot n^2 \cdot \mathrm{pO}_2^{1/2} = K_0 \exp\frac{-H_{\mathrm{r}}}{kT}$	4-7
$\mu_e = \frac{\mu_{o,e}}{T}\exp(-\frac{H_{m,e}}{kT})$	4-8

$\ln \sigma_n T = \ln C + (-\frac{Hr}{3k} - \frac{H_{m,n}}{k}) \cdot \frac{1}{T}$	4-9
$\ln \sigma_n T = \ln C + (-\frac{Hr}{2k} - \frac{H_{m,n}}{k}) \cdot \frac{1}{T}$	4-10

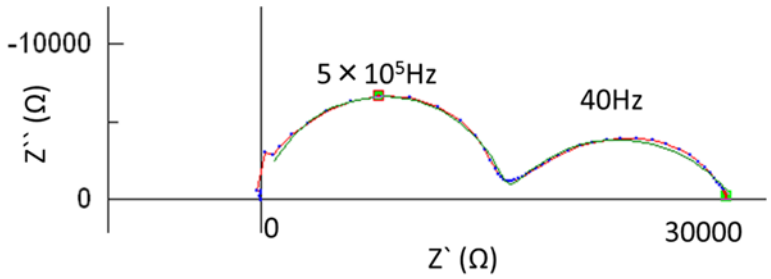

Figure 4-17 Impedance spectra of 20 mol% Mn-CeO_2 at 750 °C in air.

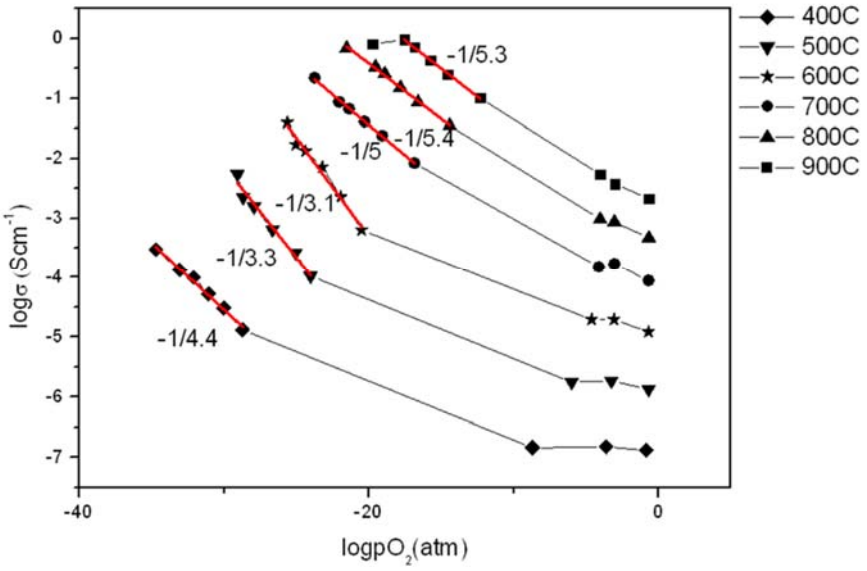

Figure 4-18 Electrical conductivity of 20 mol% Mn-CeO_2 as a function of pO_2

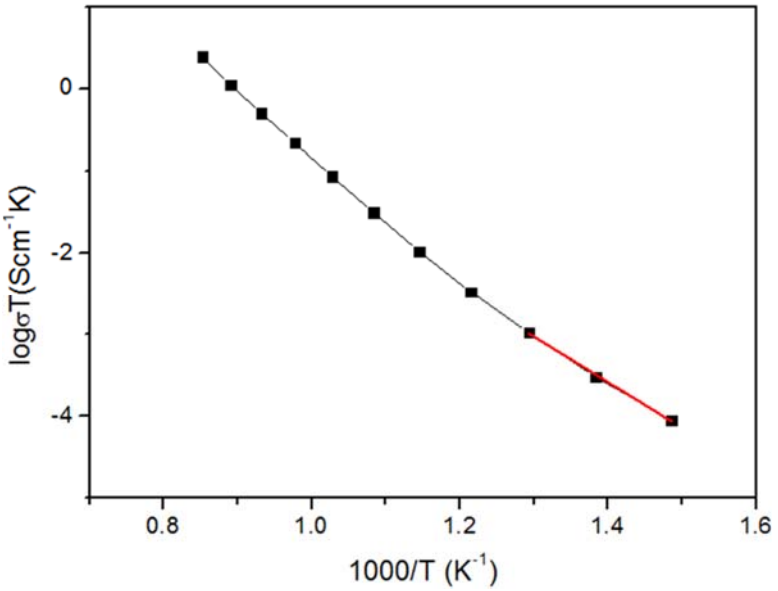

Figure 4-19 Electrical conductivity of 20 mol% Mn-CeO_2 as a function of temperature in air.

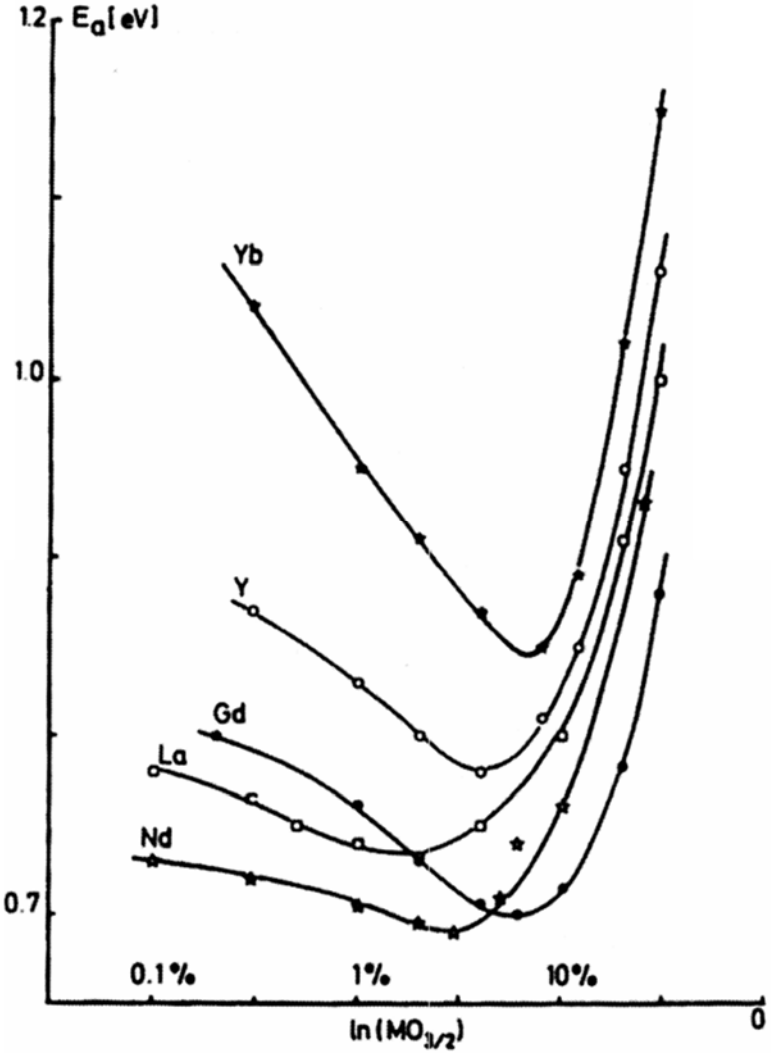

Figure 4-20 Activation energy versus composition for the different dopants (obtained from (*35*))

4.3 Conclusion

x mol% Mn-CeO_2 and x mol% Fe-CeO_2 (x=3-50) powders were synthesized by the Pechini method. Raman spectroscopy and lattice parameter analysis revealed that the solubility limit of Mn or Fe in CeO_2 is lower than 3 mol% for the present preparation conditions. The low solubility limit was rationalized in terms of the much smaller ionic radius of Mn or Fe versus Ce. As a consequence, an approach to increase the Mn or Fe radii size through an anneal in reducing conditions (humidified H_2 at 1100 °C) was attempted. In this case, the MnO and $CeFeO_3$ phase was observed by XRD, thereby indicating difficulty in obtaining Mn or Fe doped CeO_2 under reducing conditions, as well. In order to increase the solubility limit of Mn in CeO_2, La or Zr was co-doped into Mn-CeO_2. By calculating the change of lattice parameter, for 10 mol% Mn-CeO_2, the Mn solubility was estimated to increase to 2.9 mol% with 10 mol% La dopant. Mass change in 20 mol%Mn-CeO_2 powder as a function of pO_2 and temperature was measured using TGA. Based on the mass change from air to 0.2% H_2 expected for reduction of Mn oxide, the concentration of Mn in the ceria solution was calculated to be ~7.5 mol% for the three samples prepared independently which is in contradiction to the above XRD and Raman measurements. Conductivity of 20 mol%-CeO_2 was measured by impedance spectroscopy. 20 mol%Mn-CeO_2 showed a pure ceria like pO_2 dependence at higher temperature and a doped ceria like one at lower temperature. Additionally, the reduction enthalpy derived from conductivity agreed with that for pure or acceptor doped ceria. The activation energy calculated from Arrhenius plot of conductivity is 1.1 eV. From the activation energy data versus composition for the different dopants (Figure 4-20), the Mn solubility is estimated to be about 0.1~1mol%, in agreement with XRD and Raman results. The low solubility of Mn and Fe in ceria indicates that suggested improvements in SOFC performance with this material are not related to enhanced bulk MIEC behavior of doped ceria. Instead, further studies should examine the role of Mn and Fe on other factors, such as surface chemistry or catalytic activity.

Reference

1. S. B. Adler, Factors governing oxygen reduction in solid oxide fuel cell cathodes. *Chem. Rev.* **104**, 4791-4843 (2004).
2. K. Z. Li, H. Wang, Y. G. Wei, D. X. Yan, Transformation of methane into synthesis gas using the redox property of Ce-Fe mixed oxides: Effect of calcination temperature. *Int. J. Hydrog. Energy* **36**, 3471-3482 (2011).
3. P. Singh, M. S. Hegde, Sonochemical synthesis of $Ce_{1-x}Fe_xO_{2-\delta}$ (0 <= x <= 0.45) and Ce0.65Fe0.33Pd0.02O2-delta nanocrystallites: oxygen storage material, CO oxidation and water gas shift catalyst. *Dalton Trans.* **39**, 10768-10780 (2010).
4. F. J. Perez-Alonso, M. L. Granados, M. Ojeda, P. Terreros, S. Rojas, T. Herranz, J. L. G. Fierro, M. Gracia, J. R. Gancedo, Chemical structures of coprecipitated Fe-Ce mixed oxides. *Chem. Mat.* **17**, 2329-2339 (2005).
5. H. Lv, D. J. Yang, X. M. Pan, J. S. Zheng, C. M. Zhang, W. Zhou, J. X. Ma, K. A. Hu, Performance of Ce/Fe oxide anodes for SOFC operating on methane fuel. *Mater. Res. Bull.* **44**, 1244-1248 (2009).
6. T. H. Shin, S. Ida, T. Ishihara, Doped CeO(2)-LaFeO(3) Composite Oxide as an Active Anode for Direct Hydrocarbon-Type Solid Oxide Fuel Cells. *J. Am. Chem. Soc.* **133**, 19399-19407 (2011).
7. J. A. Perez-Omil, J. J. Delgado, W. Ouahbi, A. B. Hungria, N. Browning, M. A. Cauqui, J. M. Rodriguez-Izquierdo, J. J. Calvino, Electron Microscopy Investigations of Nanostructured Ce/Mn Oxides for Catalytic Wet Oxidation. *J. Phys. Chem. C* **114**, 8981-8991 (2010).
8. M. Machida, M. Uto, D. Kurogi, T. Kijima, MnO_x-CeO_2 binary oxides for catalytic NO_x sorption at low temperatures. Sorptive removal of NO_x. *Chem. Mat.* **12**, 3158-3164 (2000).
9. D. Delimaris, T. Ioannides, VOC oxidation over MnO_x-CeO_2 catalysts prepared by a combustion method. *Appl. Catal. B-Environ.* **84**, 303-312 (2008).
10. G. S. Li, R. L. Smith, H. Inomata, Synthesis of nanoscale $Ce_{1-x}Fe_xO_2$ solid solutions via a low-temperature approach. *J. Am. Chem. Soc.* **123**, 11091-11092 (2001).
11. P. Singh, M. S. Hegde, Controlled synthesis of nanocrystalline CeO(2) and Ce(1-x)M(x)O(2-delta) (M = Zr, Y, Ti, Pr and Fe) solid solutions by the hydrothermal method: Structure and oxygen storage capacity. *J. Solid State Chem.* **181**, 3248-3256 (2008).
12. H. Lv, H. Y. Tu, B. Y. Zhao, Y. J. Wu, K. A. Hu, Synthesis and electrochemical behavior of $Ce_{1-x}Fe_xO_{2-\delta}$ as a possible SOFC anode materials. *Solid State Ion.* **177**, 3467-3472 (2007).
13. G. Zhou, P. R. Shah, R. J. Gorte, A study of cerium-manganese mixed oxides for oxidation catalysis. *Catal. Lett.* **120**, 191-197 (2008).
14. L. W. Jia, M. Q. Shen, J. J. Hao, T. Rao, J. Wang, Dynamic oxygen storage and release over $Mn_{0.1}Ce_{0.9}O_x$ and $Mn_{0.1}Ce_{0.6}Zr_{0.3}O_x$ complex compounds and structural characterization. *J. Alloy. Compd.* **454**, 321-326 (2008).
15. C. Y. Kang, H. Kusaba, H. Yahiro, K. Sasaki, Y. Teraoka, Preparation, characterization and electrical property of Mn-doped ceria-based oxides. *Solid State Ion.* **177**, 1799-1802 (2006).
16. T. S. Zhang, P. Hing, H. T. Huang, J. Kilner, The effect of Fe doping on the sintering behavior of commercial CeO2 powder. *J. Mater. Process. Technol.* **113**, 463-468 (2001).
17. M. Shi, Y. D. Xu, A. P. Liu, N. Liu, C. Wang, P. Majewski, F. Aldinger, Synthesis and

characterization of Sr- and Mg-doped Lanthanum gallate electrolyte materials prepared via the Pechini method. *Mater. Chem. Phys.* **114**, 43-46 (2009).

18. J. R. McBride, K. C. Hass, B. D. Poindexter, W. H. Weber, Raman and X-ray Studies of $Ce_{1-x}Re_xO_{2-y}$, where Re=La, Pr, Nd, Eu, Gd, and Tb. *J. Appl. Phys.* **76**, 2435-2441 (1994).
19. W. J. Hong, S. Iwamoto, S. Hosokawa, K. Wada, H. Kanai, M. Inoue, Effect of Mn content on physical properties of CeO_x-MnO_y support and BaO-CeO_x-MnO_y catalysts for direct NO decomposition. *J. Catal.* **277**, 208-216 (2011).
20. D. L. A. deFaria, S. V. Silva, M. T. deOliveira, Raman microspectroscopy of some iron oxides and oxyhydroxides. *J. Raman Spectrosc.* **28**, 873-878 (1997).
21. R. D. Shannon, Revised effective ionic-radii and systematic studies of interatomic distances in halides and chalcogenides. *Acta Crystallogr. Sect. A* **32**, 751-767 (1976).
22. Y. D. Tretyakov, V. V. Sorokin, A. R. Kaul, A. P. Erastova, Phase-equilibria and thermodynamics of coexisting phases in rare-earth element iron-oxygen systems .1. Cerium-iron-oxygen system. *J. Solid State Chem.* **18**, 253-261 (1976).
23. K. Kitayama, K. Nojiri, T. Sugihara, T. Katsura, PHASE-EQUILIBRIA IN THE CE-O AND CE-FE-O SYSTEMS. *J. Solid State Chem.* **56**, 1-11 (1985).
24. D. J. Kim, Lattice-Parameters, Ionic Conductivities, and Solubility Limits in Fluorite-Structure $Hf^{-4+}O_2$, $Zr^{-4+}O_2$, $Ce^{-4+}O_2$, $Th^{-4+}O_2$, $V^{-4+}O_2$ Oxide Solid-Solutions. *Journal of the American Ceramic Society* **72**, 1415-1421 (1989).
25. C. M. Hamm, L. Alff, B. Albert, Synthesis of Microcrystalline Ce_2O_3 and Formation of Solid Solutions between Cerium and Lanthanum Oxides. *Z Anorg Allg Chem* **640**, 1050-1053 (2014).
26. S. J. Hong, A. V. Virkar, Lattice-Parameters and Densities of Rare-Earth-Oxide Doped Ceria Electrolytes. *Journal of the American Ceramic Society* **78**, 433-439 (1995).
27. D. Marrocchelli, S. R. Bishop, H. L. Tuller, B. Yildiz, Understanding Chemical Expansion in Non-Stoichiometric Oxides: Ceria and Zirconia Case Studies. *Adv Funct Mater* **22**, 1958-1965 (2012).
28. M. Kuhn, S. R. Bishop, J. L. M. Rupp, H. L. Tuller, Structural characterization and oxygen nonstoichiometry of ceria-zirconia ($Ce_{1-x}Zr_xO_{2-\delta}$) solid solutions. *Acta Mater.* **61**, 4277-4288 (2013).
29. R. J. Panlener, R. N. Blumenthal, J. E. Garnier, Thermodynamic Study of Nonstoichiometric Cerium Dioxide. *J. Phys. Chem. Solids* **36**, 1213-1222 (1975).
30. A. N. Grundy, B. Hallstedt, L. J. Gauckler, Assessment of the Mn-O system. *J Phase Equilib* **24**, 21-39 (2003).
31. S. R. Bishop, K. L. Duncan, E. D. Wachsman, Defect equilibria and chemical expansion in non-stoichiometric undoped and gadolinium-doped cerium oxide. *Electrochimica Acta* **54**, 1436-1443 (2009).
32. T. Otake, H. Yugami, K. Yashiro, Y. Nigara, T. Kawada, J. Mizusaki, Nonstoichiometry of $Ce_{1-x}Y_xO_{2-0.5x-\delta}$ (X=0.1, 0.2). *Solid State Ion.* **161**, 181-186 (2003).
33. H. L. Tuller, A. S. Nowick, Small polaron electron-transport in reduced CeO_2 single-crystals. *J. Phys. Chem. Solids* **38**, 859-867 (1977).
34. K. Eguchi, T. Setoguchi, T. Inoue, H. Arai, Electrical-Properties of Ceria-Based Oxides and Their Application to Solid Oxide Fuel-Cells. *Solid State Ion.* **52**, 165-172 (1992).
35. J. Faber, C. Geoffroy, A. Roux, A. Sylvestre, P. Abelard, A Systematic Investigation of the Dc-Electrical Conductivity of Rare-Earth Doped Ceria. *Appl Phys a-Mater* **49**, 225-232

(1989).

Chapter 5 Oxygen exchange rate of Pr-CeO_2 by OTR measurement

5.1 Introduction

As mentioned in the introduction, solid oxide fuel cells (SOFCs) convert a variety of energy sources (e.g., diesel, propane, natural gas, and biomass) to electricity with very high efficiencies.(*1-3*) Impurities in the operating environment (e.g. in feed gases or in the cell materials) are well known to contribute to long-term degradation in performance of SOFCs, therefore, in part, hindering widespread SOFC commercialization. For example, Si based phases (siliceous material) have been found to block the active sites to oxygen exchange at the gas/solid interface on yttria-stabilized zirconia (YSZ),(*4-6*) Gd doped ceria (GDC),(*7*) (La,Sr)(Co,Fe)$O_{3-\delta}$ (LSCF),(*8-10*) and (La,Sr)$CoO_{3-\delta}$ (LSC)(*11*) electrode materials. In larger quantities, siliceous material can also cover the interface between electrode and electrolyte, thereby reducing the highly active triple phase boundary length between gas and NiO/YSZ(*12-15*) and LSM/YSZ(*16-18*) composite electrodes. Si is ubiquitous in ceramics processing and testing; for example, it can come from furnace refractories during high temperature sintering,(*19*) or even from the silicone grease used in the apparatus to establish input gas mixtures for fuel cell test assemblies.(*4*) While past researchers have spent significant effort and cost to reduce siliceous impurities through clean processing(*20, 21*), in this work, we take a more commercially viable approach to dealing with Si by developing Si impurity tolerant electrodes.

Due to the presence of simultaneous oxide ion and electron conduction, mixed ionic and electronic conductors (MIECs) exhibit oxygen exchange over their entire surface and are thus intensely studied, and used, as SOFC electrodes. $Pr_xCe_{1-x}O_{2-\delta}$ (PCO) is an MIEC which has an oxygen exchange coefficient similar to some of the top performing SOFC electrodes, e.g. LSC and LSCF at ~600 °C in cathode conditions.(*22*) Additionally, ceria based materials have been shown to exhibit good catalytic activity for SOFC anode reactions and heterogeneous catalysis.(*23, 24*) Previously, our group developed a new, *in situ* optical transmission technique to study the oxygen content in PCO thin films via optically active defect centers.(*25*) Upon a step increase in oxygen partial pressure (pO_2) at elevated temperatures (e.g. 600 - 900 °C), oxygen fills an oxygen vacancy and Pr^{3+} is consequently oxidized to Pr^{4+} as shown by Equation 1, written in the Kröger-Vink notation.(*26, 27*)

$$2\,Pr'_{Ce} + V_O^{\bullet\bullet} + \frac{1}{2}O_2 \rightarrow 2Pr_{Ce}^{\times} + O_O^{\times} \qquad 5\text{-}1$$

where $V_O^{\bullet\bullet}$, $O_O^{\times}$, Pr'_{Ce}, and $Pr_{Ce}^{\times}$ denote an oxygen vacancy, oxide ion, Pr^{3+}, and Pr^{4+}, respectively. Electrons can be excited from the valence band into the empty Pr^{4+} levels, resulting in a reddish coloration, and a consequent decrease in light transmission through the film with oxidation as more Pr^{4+} is formed.(*25*) By following the change in optical transmission with time upon a step change in pO_2, i.e. optical transmission relaxation (OTR), the oxygen exchange kinetics can be evaluated. Since OTR is an *in situ* technique that probes oxygen exchange on the bare surface of materials, it has

advantages over the more common, *ex situ* isotopic exchange technique, as well as the area specific resistance (ASR) measurement technique that typically requires surface contact with metallic, and potentially catalytic and partially surface blocking, current collecting electrodes.(*22, 28-31*). Previously we showed the presence of a large buildup of impurities (e.g., Si) on the surface of PCO films, which was correlated to reduced oxygen exchange kinetics using the OTR technique.(*32, 33*) In the present work, OTR is used in combination with deposition of second phase oxides, using pulsed laser deposition (PLD), on the surface of PCO to systematically identify materials that will improve the redox kinetics of aged films (degraded by the presence of impurities). Previously, others have found that La may getter Si impurities at grain boundaries of (GDC);(*34*) additionally, early studies have shown that La added to the surface of GDC improved its oxygen exchange rate by >10 x which may arise from a possible cleaning effect.(*35*) The present work builds substantially on this latter earlier finding by systematically identifying other oxide surface treatments that dramatically enhance redox kinetics after aging of PCO films and further aiding in establishing the mechanism for enhancement. Additionally, by simply integrating La into the PCO electrode in a solid solution, a more impurity-tolerant electrode amenable to industrial processing is demonstrated with positive initial results.

5.2 Results and Discussion

5.2.1 XRD and film morphology of PCO

All films exhibited peaks consistent with the fluorite phase of PCO, with highly (111) oriented texture on Al_2O_3 (0001), MgO (100) and SiO_2 (110) substrates and (110) on YSZ (110) substrates (Figure 5-1). The film thicknesses, as determined from SEM (Figure 5-2, Figure 5-7), ranged from about 200 to 330 nm. Since the film thickness is much less than the ratio of diffusivity to surface exchange rate coefficient (e.g. $D/k \cong 3.56 \times 10^3$ μm at 670 °C), the redox process is limited by surface oxygen exchange (and not bulk diffusion), as previously described.(*22*)

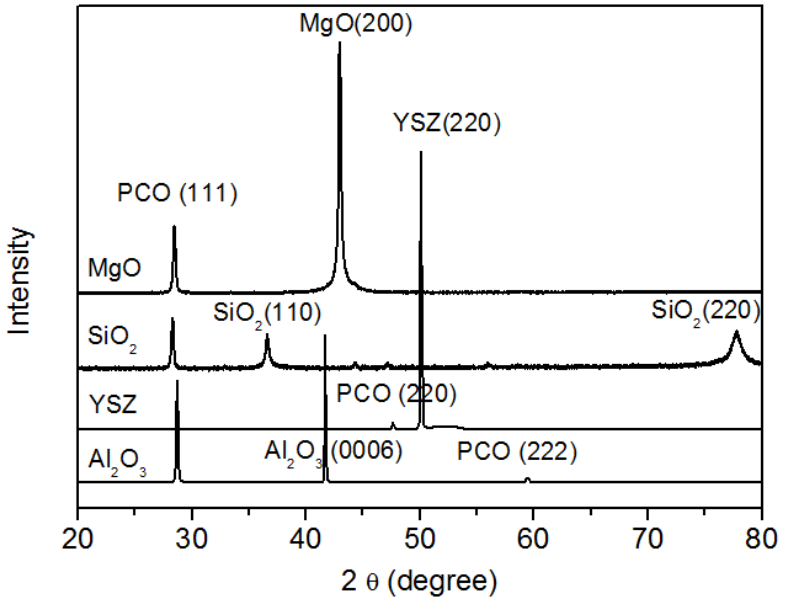

Figure 5-1 XRD patterns of PCO films on Al_2O_3, YSZ, SiO_2 and MgO substrates.

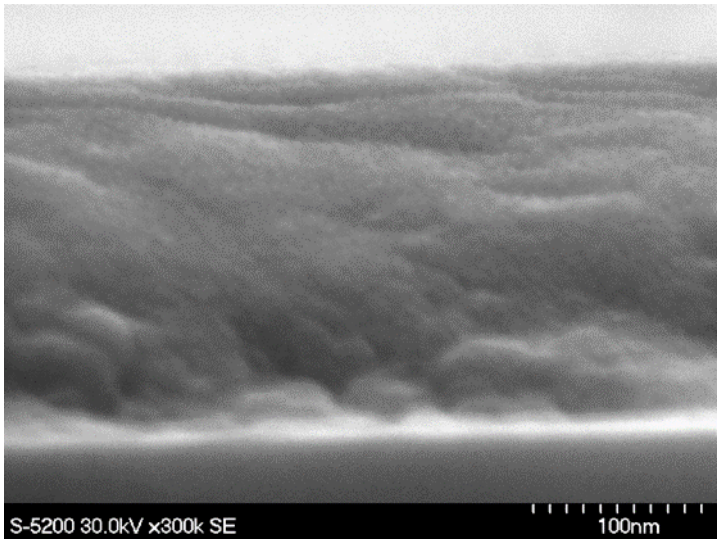

Figure 5-2 SEM image of the cross-section of a PCO film on Al_2O_3 substrate. The film is ~215 nm thick.

5.2.2 OTR measurements of fresh and aged PCO thin films

The OTR profiles following a step change in oxygen partial pressure (pO_2) from 4% O_2 to 21% O_2 at 600 °C for fresh and aged (114 hours aging at 600 ºC) films are shown in Figure 5-3. The decrease in transmitted intensity corresponds to an increase in the concentration of optically absorbing Pr^{4+} centers (*25*) and therefore an increase in oxygen content (Equation 5-1) as described in the introduction. It is noted that upon exposure to the opposite step change in pO_2, this behavior is nearly completely reproducible. Clearly, aging decreases the rate of oxidation dramatically in these films. From the following equation (previously shown to describe the rate of oxygen exchange during OTR of PCO thin films),(*36*) time constants (τ) were extracted for quantitative comparison of the data.

$$\frac{\ln I_t - \ln I_0}{\ln I_f - \ln I_0} = 1 - \exp\left(-\frac{t}{\tau}\right) \qquad 5\text{-}2$$

where I_t , I_0 , and I_f are the transmitted light intensity at a given time (t), initial time, and final time, respectively. The natural log of intensity is used due to the logarithmic dependence of light absorption on Pr^{4+} concentration.(*25*) In a semi-log plot of the OTR data following the above equation, a straight line is observed from which the slope yields τ as shown elsewhere.(*36, 37*) It is noted here that the chemical surface exchange coefficient (k_{chem}), describing the rate of oxygen uptake or release across the gas/solid phase interface, is given by $k_{chem} = L/\tau$, where L is the film thickness. Since τ changes by orders of magnitude during aging, but the film thickness varies by less than 50% between different films, the error associated with differences in L is ignored and discussion is limited to interpreting changes in τ. Unless otherwise indicated, τ is reported for an oxygen partial pressure change from 4% O_2 to 21% O_2 at 600 °C. For a thickness of 250 nm, the $\tau \approx 30$ seconds for the fresh PCO film in Figure 5-3 corresponds to a $k_{chem} \sim 8 \times 10^{-7}$ cms^{-1}. After aging for 114 hours, $\tau \approx 1200$ seconds, over 40 times greater.

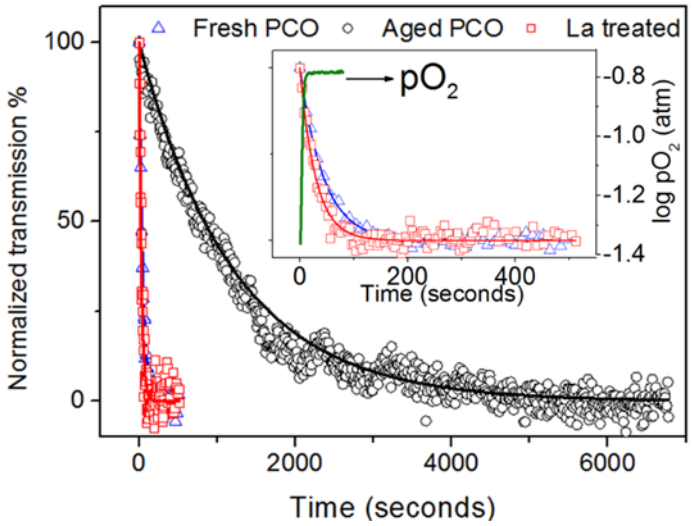

Figure 5-3 OTR curve for a PCO film measured at 600 ºC following a pO_2 step from 4% O_2 to 21% O_2. The solid lines represent fits of **Equation 2** to the data. The inset, a magnification of the data, also shows the rapid change of pO_2 as compared to relaxation times.

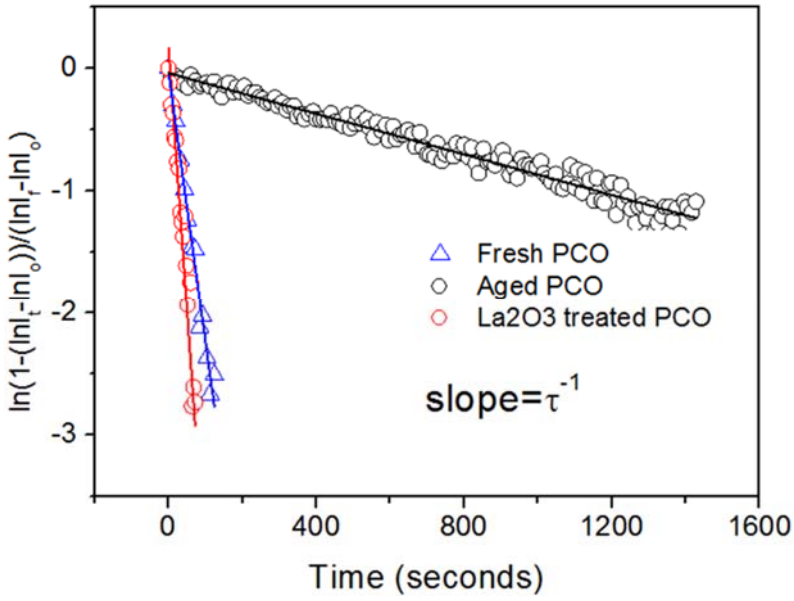

Figure 5-4 Method for extracting time constant from relaxation data in Figure 5-3.

After aging the PCO film for 60 hours, a significant amount of Si was identified at the film surface using XPS as shown in Figure 5-5, which is consistent with our prior finding of accumulation of K, Na, Si, and Ca impurities at the surface of another aged PCO film measured by secondary ion mass spectrometry.(*32*) As described in the introduction, the presence of Si in these oxidizing atmospheres indicates the existence of a siliceous phase, which is likely blocking active oxygen exchange sites on PCO. To further confirm the impact of siliceous impurities on oxygen exchange kinetics, Si was intentionally deposited using PLD from a Si target on a fresh PCO surface, followed by OTR measurements in oxidizing conditions and confirmed by XPS as also shown in Figure 5-5. With intentionally deposited siliceous phase, τ increased by >370 times, from 30 seconds (fresh film) to ~11,200 seconds, clearly demonstrating the negative impact of siliceous phase.

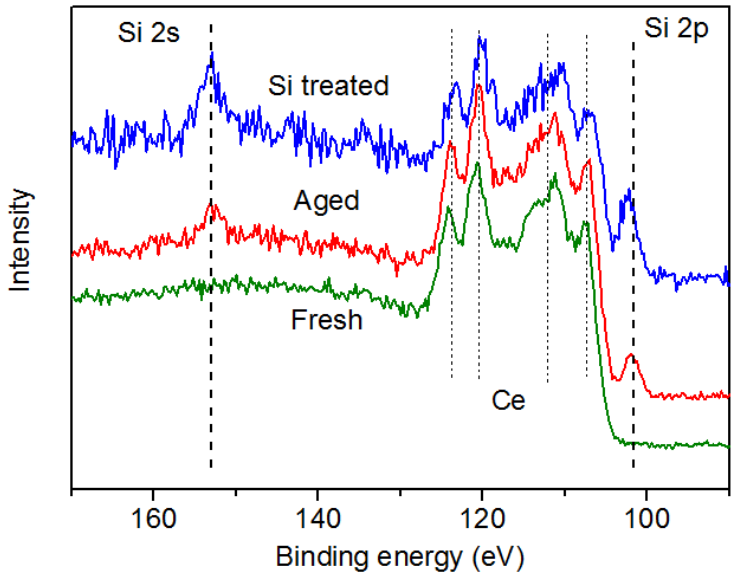

Figure 5-5 XPS spectra of PCO films showing the presence of Si in aged and Si treated films.

In order to identify the source of impurities, systematic studies varying the potential sources of impurities were undertaken. Three potential sources for impurities were considered: (1) gas transport from the measurement chamber, (2) gas transport or bulk diffusion from the substrate, and (3) bulk diffusion from the interior of the PCO film. Films deposited on four different substrates and with two different PCO targets of varying precursor purity were examined for sources (2) and (3), respectively. In Figure 5-6 all of these films show significant degradation of oxygen exchange kinetics with no obvious dependence on sources (2) or (3). Additionally, Si was not observed on the surface of a PCO film that was aged in the PLD chamber under vacuum ($1x10^{-5}$ Pa) at 700 °C for 40 hours immediately after deposition (see Figure 5-5), further indicating that Si impurities were not introduced to a significant extent during deposition. These results indicate that Si impurities likely originate from the experimental setup, (1), during OTR measurements. In fact, a trend of decreasing degradation rate with the order at which different films were measured (also shown in Figure 5-6) indicates that impurities may have been present in the reactor tube from the start of the first measurements, and over time become depleted, unless more are unintentionally introduced later (e.g. as furnace insulation particles). It is worth mentioning that though impurity source (1) seems to dominate degradation, sources (2) and (3) may still contain many impurities that could influence degradation in a cleaner testing environment.

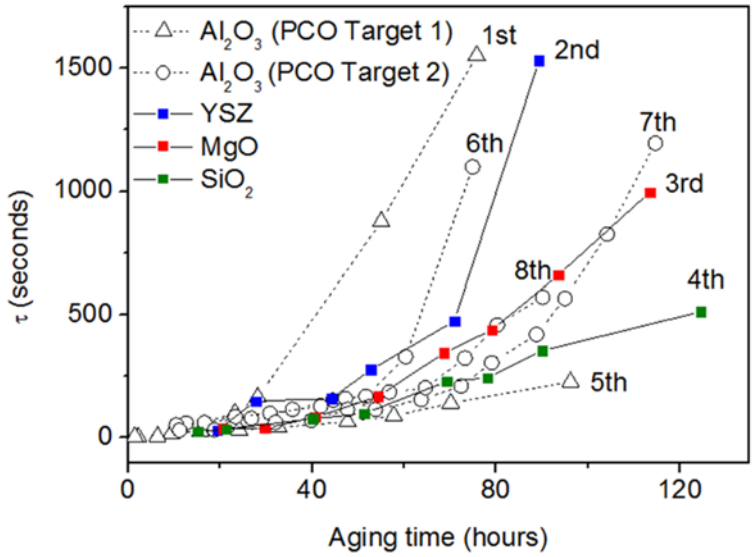

Figure 5-6 Plot of τ versus aging time for PCO films deposited identically on different substrates or using different targets. No clear trend in degradation rate (increase in τ with time) is observed with target or substrate choice. Numbers indicate the order at which the measurements were taken.

5.2.3 Dramatic recovery of oxygen exchange kinetics with La oxide deposition on aged PCO films

As discussed in the introduction and results above, 1) impurities play a key role in degradation of SOFC electrodes and should be dealt with in a commercially viable manner, and 2) La oxide has previously been suggested to interact with impurities at interfaces to improve ion transport.(*34, 35*) We now turn to demonstrating a second phase treatment with La that assists in overcoming impurity induced degradation. La oxide was deposited by PLD at room temperature on an aged PCO thin film and, as shown in Figure 5-3, the oxidation kinetics fully recovered to the initial, "fresh" PCO film performance. Even on the film with intentionally deposited Si (not shown), τ was reduced from over 11,200 s to 13 s, nearly 3 orders of magnitude improvement. In fact, the measured oxidation times begin to approach the limit of time taken to change pO_2 in the test setup (see Figure 5-3 inset), and therefore may be even faster than reported here.

After deposition, the La oxide layer is about 5 nm thick as shown by the cross-sectional TEM image in Figure 5-7**a**. Dark grey areas in the La oxide layer suggest porosity for gas diffusion to the PCO film. During initial measurements, a critical amount of La oxide (~100 laser shots in the PLD, as compared to 2 and 10) was necessary to achieve the recovered kinetics. In several circumstances, La oxide treated PCO films were found to age again during OTR measurements, and further depositions of La oxide recovered kinetics. Figure 5-7**b** shows the cross section of an aged film treated with La oxide then aged again and treated with La oxide multiple times and finally aged to very poor redox kinetics. A ~20 nm La oxide layer and a particle on the surface (particles were observed in many locations on the film with, e.g., an optical microscope after multiple treatments/aging) are observed. Si was detected as the major impurity in the La oxide layer and the surface particle by EDS, as shown by Table 5-1. The critical amount of La oxide required to facilitate recovered kinetics and the accumulation of Si in the La-containing areas both indicate that Si and La are interacting. From Table 5-1, the existence of Pr and Ce in region 2 likely arises from partial EDS measurement of the PCO film in addition to the La oxide film. It is worth mentioning that the ratio of Pr to Ce in this

region is approximately equal to what is expected for the intended $Pr_{0.1}Ce_{0.9}O_{2-\delta}$ composition. The presence of Na and Al on the film surface (Table 5-1) is also not surprising, as furnace insulation often contains these elements as well as Si and providing further evidence that impurities are largely introduced during the OTR measurement.

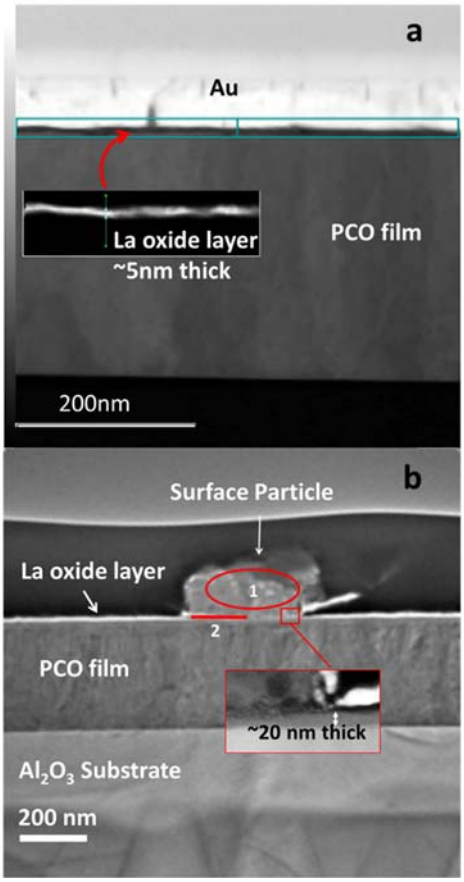

Figure 5-7 STEM image of (a) an aged PCO film treated with La oxide and measured once by OTR with no further aging and (b) an aged PCO film repeatedly aged and treated with La oxide, and ultimately aged to very poor redox kinetics.

Table 5-1 EDS element analysis of areas 1 and 2 shown in Figure 5-7b

Element	Na K	Al K	Si K	La L	Ce L	Pr L
Area 1 atomic %	0.5±0.018	1.9±0.016	6.1±0.016	90.9±0.009	0.6±0.012	0
Area 2 atomic %	0.6±0.02	2±0.019	14.8±0.019	67.6±0.014	13.3±0.015	1.7±0.014

To study the possibility of a reaction between La and Si oxides, the O 1s energy level, which is sensitive to bonding environment, of an aged PCO film treated with La oxide and aged again was examined with XPS, as shown by Figure 5-8. The backgrounds of the spectra were subtracted using Shirley's method, and for illustrative purposes, the spectra were fitted using a nonlinear least squares method with two or three Gaussian-Lorentzian shaped peaks of equal full width half maximum. For the fresh PCO film (Figure 5-8a), two peaks are observed, which have previously been assigned to oxygen bound to Ce (IV) and Ce(III) at low and high binding energies, respectively.(*38, 39*) After

aging (Figure 5-8b), a third peak appears, intermediate between the first two. As shown by Figure 5-5, after aging, Si was found on the PCO film surface, and therefore this peak is likely from oxygen bound to Si and Ce (Si-O-Ce), as previously identified for ceria by others.(*40-42*) The high energy peak also shifts slightly and the intensity ratio between it and the low energy peak changes, indicating that the high energy peak may represent oxygen bound to Si as suggested previously.(*40-42*) This behavior is more clearly observed in the intentionally Si treated sample (Figure 5-8c), where the high energy peak becomes much larger and the low energy peak (Ce(IV)-O) decreases as the PCO film is covered by siliceous phase. After the La oxide treatment (Figure 5-8d**)**, the intermediate peak is now by far the largest of all three peaks, and, for previous studies on the interface between La and Si oxides, has been assigned to oxygen bound to both La and Si (La-O-Si), with the high energy peak previously assigned to La-O-H.(*43-45*) In the present case, this result indicates that there is a significant reaction between the Si and La, possibly forming a lanthanum silicate compound. Though the temperature for reaction here is low (600 ^{o}C), the short diffusion lengths of the thin film layers of Si and La oxides likely facilitate reaction with La oxide. Indeed, previous researchers have also observed the formation of a La-silicate layer formed between La oxide and Si at temperatures of 200 - 400 ^{o}C.(*43, 44*)

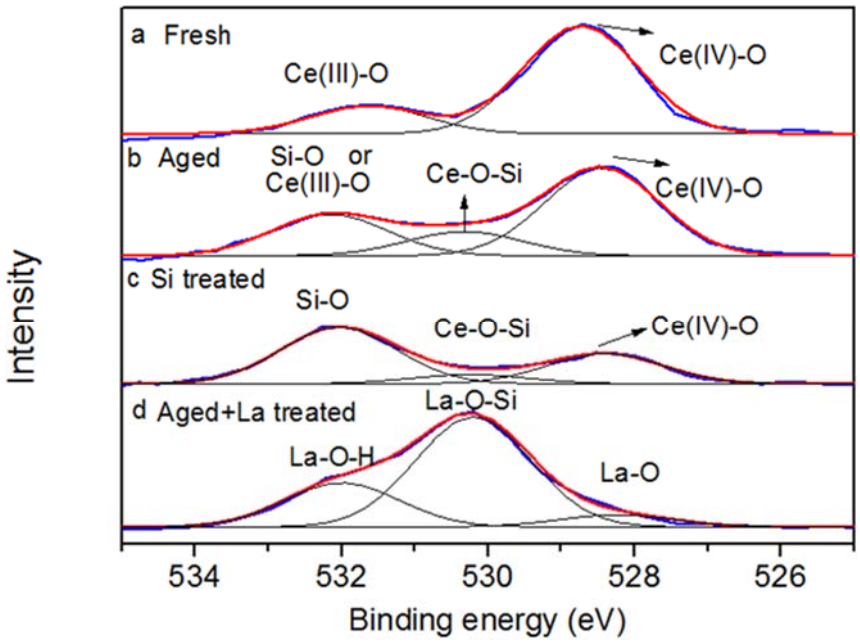

Figure 5-8 O 1s XPS spectra of (a) a fresh PCO film (b) an aged PCO film (c) an Si treated PCO film (d) a La oxide-treated aged PCO film. A peak corresponding to La-O-Si bonding indicates a reaction between La and Si. Blue lines show the original spectra, black lines show Gaussian-Lorentzian peaks and red lines represent the summation of peaks.

Figure 5-9 shows the time constant of fresh PCO film and La oxide or Sm oxide treated PCO film at 300~600 ^{o}C . There is a clear temperature dependence of τ for the as prepared PCO film indicating oxygen exchange is faster at higher temperature. At lower temperature, oxygen exchange kinetics of the fresh PCO film is much slower than the one of treated films. The temperature dependence of τ for the as prepared PCO film could not be observed clearly due to the system limit. The interval of two measurements can only be set as short as 4 seconds, so data points are not enough to derive a precise result when the surface exchange finished in a very short time (e.g. 20 seconds). Even though, a significant improvement of surface oxygen exchange kinetics for the La_2O_3 treated films can be

observed at lower temperature (e.g. a factor of 50 at 450 ^{o}C). It indicates that Sm_2O_3 and La_2O_3 has a good catalytic effect on the surface of the PCO film.

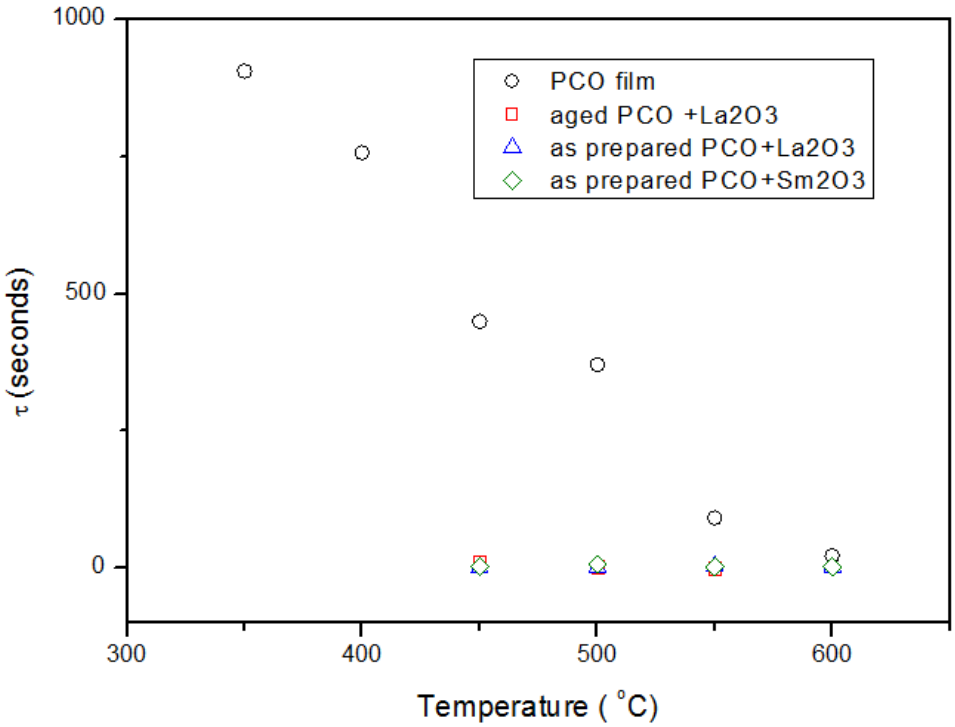

Figure 5-9 Plot of time constant versus different temperatures for as prepared and La_2O_3, Sm_2O_3 treated PCO films.

5.2.4 Long term measurement of La oxide treated PCO film

As shown in Figure 5-10, the degradation rate of the oxygen exchange kinetics is much slower than the original films. Except the one on YSZ substrate, it seems there are no further degradation after 60 hours aging.

Figure 5-11 shows the degradation rate for as-prepared PCO film treated with La oxide is much faster than the aged one.

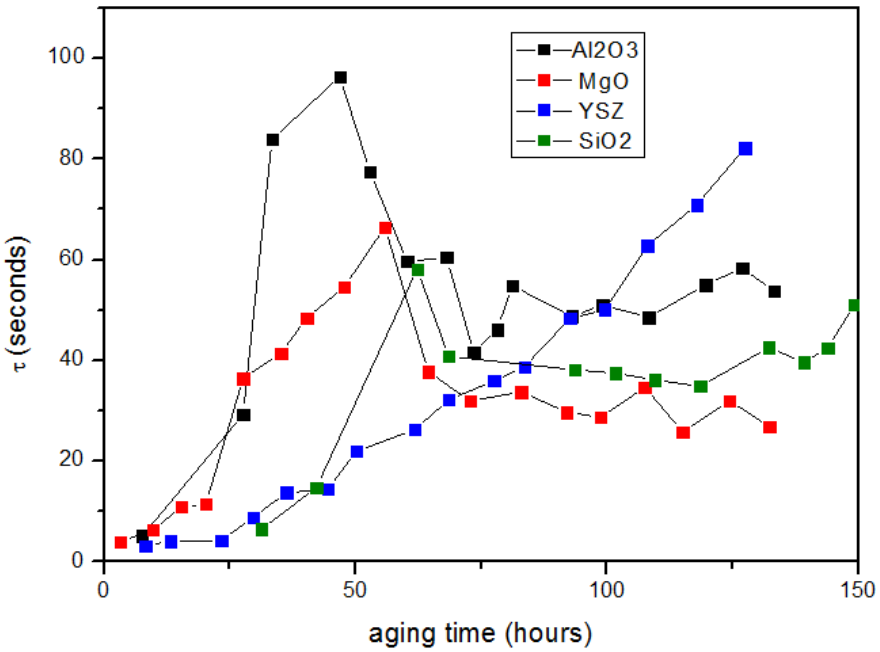

Figure 5-10 Plot of time constant versus aging time for aged films treated with La_2O_3 on sapphire, YSZ, MgO and quartz substrates

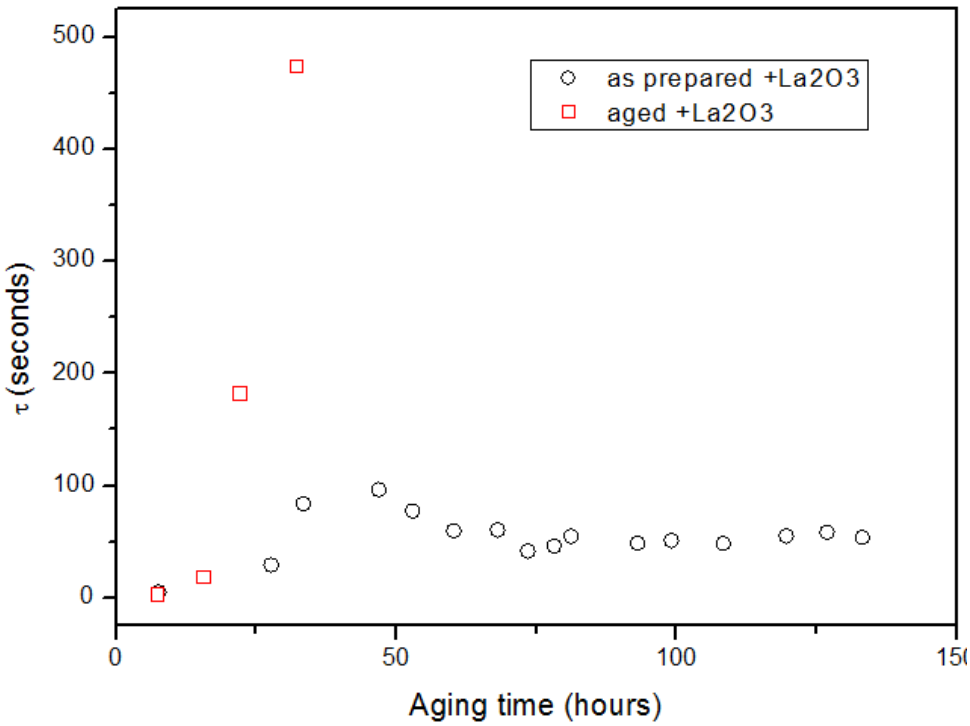

Figure 5-11 Plot of time constant versus aging time for as prepared and aged films treated with La_2O_3

5.2.5 Improved electrode performance with other oxide treatments

In order to further validate the La-Si reaction mechanism as well as explore the potential for other oxides to improve oxygen exchange, PCO films were also treated with other oxides. As shown in Figure 5-12, Sm was the only other material tested that led to an improvement in redox kinetics of an

aged PCO film. Like La, Sm may also form a silicate, as has previously been observed after annealing a Sm_2O_3 film on a Si substrate at 800 °C.(*46*) On the other hand, both Nb and Al oxides, in addition to Si, degrade redox kinetics of a fresh PCO film and, along with Ti and Zn oxides, do not aid in recovering redox kinetics after aging.

Interestingly, the La oxide treatment can recover the oxygen exchange kinetics of PCO treated with all the examined oxides, except Zn. Indeed, others have found the formation of a La-Ti oxide after calcining La_2O_3-TiO_2 at 500 °C (*47*) and La-Al oxide after reaction of an ALD film at 450 °C.(*48*) Under the present conditions, La oxide may not react sufficiently with Zn.

Finally, to test whether the La treatment universally improves oxygen exchange kinetics (e.g., by a catalytic mechanism), La oxide was also deposited on an aged $SrTi_{0.65}Fe_{0.35}O_{3-\delta}$ thin film cathode, where Sr segregation to the film surface is known to degrade redox kinetics.(*49, 50*) In this case, OTR probes the time dependent change in oxidation state of Fe during redox.(*51*) No recovery of redox kinetics was observed in the aged STF film, further confirming that rather than act as a catalyst, La is primarily interacting with Si impurities.

The mechanism of improved redox kinetics with La treatment (and Sm) is therefore believed to originate in their reaction with a dense siliceous phase to form another, porous phase, for example through a volumetric phase change accompanied by cracking, that allows gas to penetrate to the PCO film below. With further aging, the impurity film densifies, but can be "re-charged" by further addition of La. In an attempt to demonstrate the utility of this finding in a more amenable processing route for industry, La was added to the PCO target as the solid solution $La_{0.1}Pr_{0.1}Ce_{0.8}O_{1.95-\delta}$ (LPCO). Initial studies found that the aging rate of this composition was suppressed over that of PCO measured at similar times and under similar conditions by OTR. In one case, aging of redox kinetics was not found over several days for LPCO, though further work is needed to repeatedly verify these findings.

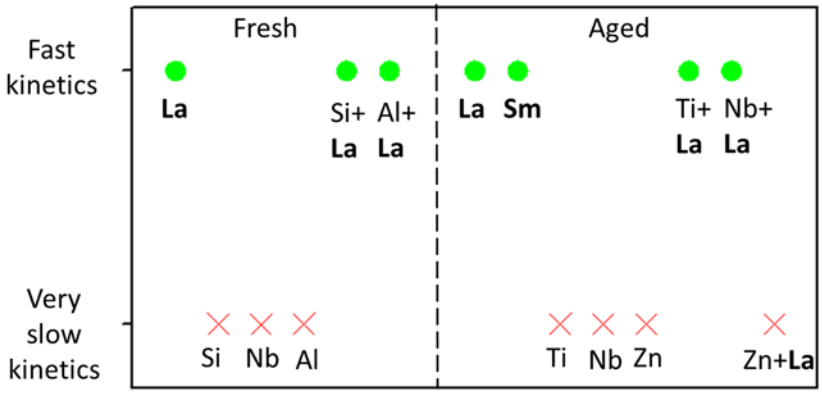

Figure 5-12 Redox kinetics on PCO films with different PLD oxide treatments (Fast kinetics: $\tau < 30$ s, very slow kinetics: $\tau > 1000$ s). "Aged" denotes deposition of the oxide on a PCO film aged to very slow kinetics.

Figure 5-13 shows Sm_2O_3, Gd_2O_3 and Pt can also recover τ of an aged PCO film to less than 5 seconds. However, Sm_2O_3 and Gd_{2O3} treated ones were degraded again at an even faster rate than an original PCO film. It is possible that La_2O_3 has an ability to getter the impurities and prevent them from diffusing, but Sm_2O_3 and Gd_2O_3 cannot. On the other hand, Pt treated film shows a very fast oxygen exchange kinetics and seems no degradation after ~100 hours aging. Apparently, Pt could not react with any element at 600 °C, so the improvement may be due to the good catalytic effect of Pt.

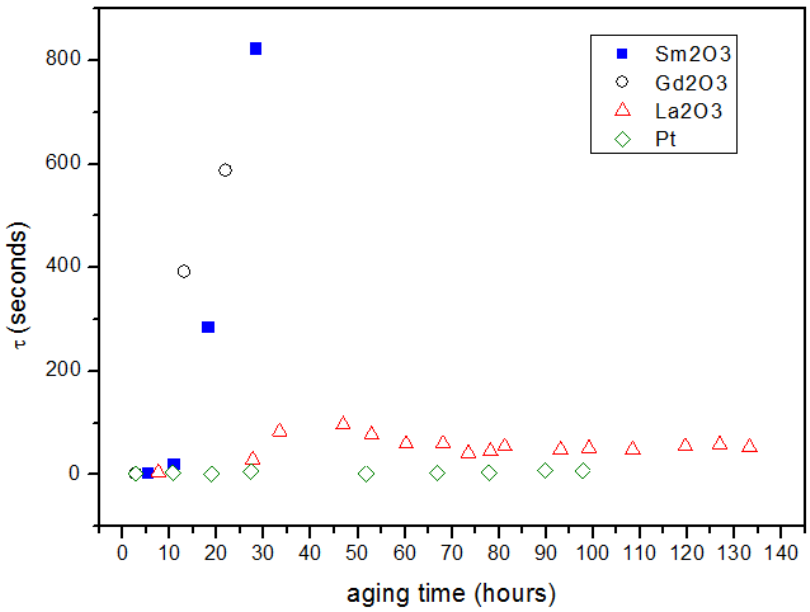

Figure 5-13 Plot of time constant versus aging time for aged films treated with Sm_2O_3, Gd_2O_3, La_2O_3 and Pt.

For the Al_2O_3 treated PCO film, the first τ is ~70 seconds which is about 10 times higher than the one of a PCO film, and the degradation rate is apparently higher than an original PCO film. It indicates that Al_2O_3 can block the active sites of oxygen exchange and also diffuse on the surface to accelerate the degradation rate. This film was removed from the sample chamber and 200 shots of La_2O_3 were deposited on the film surface. τ was recovered to less than 10 seconds and increased with time in a slower rate than the Al_2O_3 treated one. It also agrees with the fact that La_2O_3 can not only have a catalytic effect, but also somehow getters impurities and prevents their diffusion.

300 shots of Nb_2O_5 were deposited on an as-prepared and an aged PCO film, resulting in no improvement of the optical relaxation rate. An aged PCO were also treated with Nb_2O_5, the oxygen exchange rate was too slow to measure. This film was also treated with La_2O_3, and τ was also recovered to less than 10 seconds and increased with time at a slower rate. TiO_2 treatment shows a similar result as Nb_2O_5, τ was changed to 29850 seconds (8.29 hours) after TiO_2 treatment and La_2O_3 treatment, τ recovered to 75 seconds.

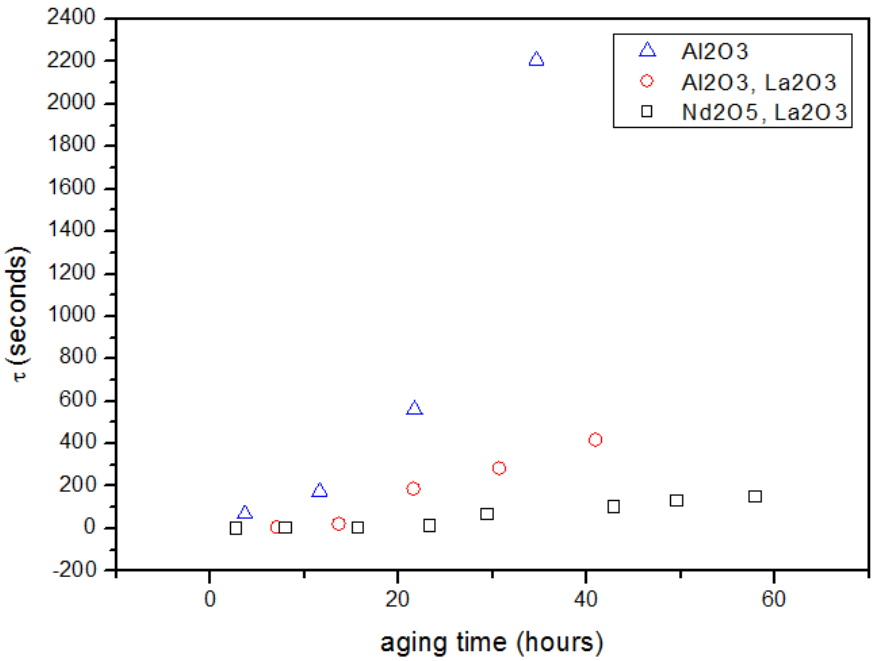

Figure 5-14 Plot of time constant versus aging time for treated PCO films: triangle: 10 shots of Al_2O_3 on an as prepared PCO film, circle: 200 shots of La_2O_3 on the Al_2O_3 treated and aged PCO film, square: 300 shots of Nb_2O_5 on an aged PCO film and La_2O_3 treated.

5.2.6 Incorporation of La into PCO film

PCO targets with La (PLCO) or Sm (PSCO) in solid solution, confirmed by XRD (not shown) with PCO were fabricated. As shown in Figure 5-15, in one PLCO case, τ did not increase over the course of the measurement, indicating the potential for La to continuously keep the PCO surface clean. However, additional measurements on PLCO and PSCO showed a degradation in τ over time which may be the result of different impurity levels in the different testing environments. Further work is needed to confirm the advantage of long term resistance to τ degradation with La and Sm PCO solid solutions.

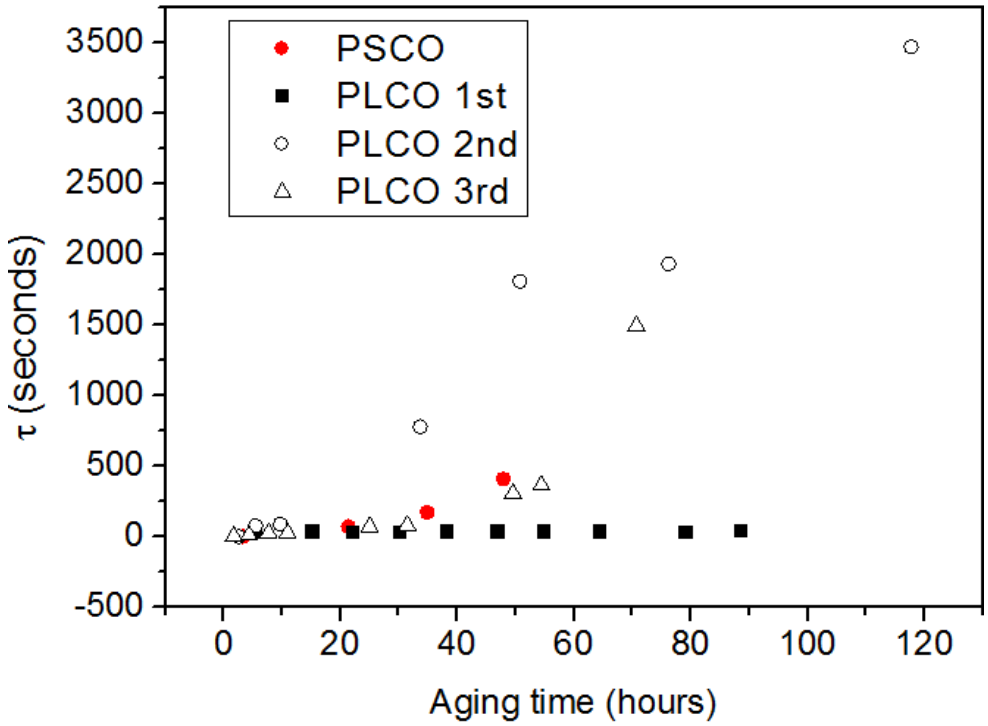

Figure 5-15 Plot of τ versus aging time for $Pr_{0.1}Sm_{0.1}Ce_{0.8}O_{1.95-\delta}$ and $Pr_{0.1}La_{0.1}Ce_{0.8}O_{1.95-\delta}$.

5.3 Conclusion

A > 40 times increase in the time constant for oxygen exchange kinetics during ~5 days of aging was found in PCO thin films using the oxygen transmission relaxation method (OTR). The degradation in kinetics was identified to arise from accumulation of a siliceous phase on the PCO film surface. From a systematic examination of impurity sources, Si is likely introduced primarily during the OTR measurement (e.g. from the quartz tube or furnace insulation) rather than through target purity, processing, or substrate (though these other sources may still have impurities present). Deposition of La oxide or Sm oxide on the aged film surface was found to fully recover oxygen exchange kinetics in aged films and a film intentionally coated with siliceous phase. Surface treatments with other oxides (Nb, Al, Ti, and Zn) were not found to recover oxygen exchange kinetics. La and Sm likely react with Si to form a porous silicate layer allowing gas transfer to the PCO surface, whereas other studied materials are unlikely to form silicates. La oxide was also deposited on aged $SrTi_{0.65}Fe_{0.35}O_{3-\delta}$, prone to degradation via Sr segregation (as opposed to siliceous phases), and no improvement was found, further indicating La reacts with Si and is not leading to a significant catalytic effect. Finally, La was added to PCO in solid solution, and initial measurements found suppressed aging of redox kinetics.

Reference

1. B. C. H. Steele, A. Heinzel, Materials for fuel-cell technologies. *Nature* **414**, 345-352 (2001).
2. E. D. Wachsman, K. T. Lee, Lowering the Temperature of Solid Oxide Fuel Cells. *Science* **334**, 935-939 (2011).
3. E. Wachsman, T. Ishihara, J. Kilner, Low-temperature solid-oxide fuel cells. *Mrs Bull* **39**, 773-779 (2014).
4. M. de Ridder, A. G. J. Vervoort, R. G. van Welzenis, H. H. Brongersma, The limiting factor for oxygen exchange at the surface of fuel cell electrolytes. *Solid State Ion.* **156**, 255-262 (2003).
5. J. L. Hertz, A. Rothschild, H. L. Tuller, Highly enhanced electrochemical performance of silicon-free platinum-yttria stabilized zirconia interfaces. *J Electroceram* **22**, 428-435 (2009).
6. E. Mutoro, N. Baumann, J. Janek, Janus-Faced SiO2: Activation and Passivation in the Electrode System Platinum/Yttria-Stabilized Zirconia. *J. Phys. Chem. Lett.* **1**, 2322-2326 (2010).
7. J. M. Bae, B. C. H. Steele, Properties of $La_{0.6}Sr_{0.4}Co_{0.2}Fe_{0.8}O_{3-\delta}$(LSCF) double layer cathodes on gadolinium-doped cerium oxide (CGO) electrolytes - I. Role of SiO_2. *Solid State Ion.* **106**, 247-253 (1998).
8. E. Bucher, W. Sitte, F. Klauser, E. Bertel, Oxygen exchange kinetics of $La_{0.58}Sr_{0.4}Co_{0.2}Fe_{0.8}O_3$ at 600 degrees C in dry and humid atmospheres. *Solid State Ion.* **191**, 61-67 (2011).
9. E. Bucher, C. Gspan, F. Hofer, W. Sitte, Post-test analysis of silicon poisoning and phase decomposition in the SOFC cathode material $La_{0.58}Sr_{0.4}Co_{0.2}Fe_{0.8}O_{3-\delta}$ by transmission electron microscopy. *Solid State Ion.* **230**, 7-11 (2013).
10. M. M. Viitanen, R. G. von Welzenis, H. H. Brongersma, F. P. F. van Berkel, Silica poisoning of oxygen membranes. *Solid State Ion.* **150**, 223-228 (2002).
11. E. Bucher, W. Sitte, F. Klauser, E. Bertel, Impact of humid atmospheres on oxygen exchange properties, surface-near elemental composition, and surface morphology of $La(0.6)Sr(0.4)CoO_{3-\delta}$. *Solid State Ion.* **208**, 43-51 (2012).
12. S. D. Ebbesen, C. Graves, A. Hauch, S. H. Jensen, M. Mogensen, Poisoning of Solid Oxide Electrolysis Cells by Impurities. *Journal of the Electrochemical Society* **157**, B1419-B1429 (2010).
13. A. Hauch, S. H. Jensen, J. B. Bilde-Sorensen, M. Mogensen, Silica segregation in the Ni/YSZ electrode. *Journal of the Electrochemical Society* **154**, A619-A626 (2007).
14. K. V. Jensen, R. Wallenberg, I. Chorkendorff, M. Mogensen, Effect of impurities on structural and electrochemical properties of the Ni-YSZ interface. *Solid State Ion.* **160**, 27-37 (2003).
15. Y. L. Liu, C. G. Jiao, Microstructure degradation of an anode/electrolyte interface in SOFC studied by transmission electron microscopy. *Solid State Ion.* **176**, 435-442 (2005).
16. J. A. Schuler, Z. Wuillemin, A. Hessler-Wyser, J. Van Herle, Glass-Forming Exogenous Silicon Contamination in Solid Oxide Fuel Cell Cathodes. *Electrochem. Solid State Lett.* **14**,

B20-B22 (2011).
17. A. Hagen, Y. L. Liu, R. Barfod, P. V. Hendriksen, Assessment of the cathode contribution to the degradation of anode-supported solid oxide fuel cells. *Journal of the Electrochemical Society* **155**, B1047-B1052 (2008).
18. M. Backhaus-Ricoult, SOFC - A playground for solid state chemistry. *Solid State Sci* **10**, 670-688 (2008).
19. http://www.zircarceramics.com/.
20. T. Andersen, K. V. Hansen, I. Chorkendorff, M. Mogensen, Strontium zirconate as silicon and aluminum scavenger in yttria stabilized zirconia. *Solid State Ion.* **190**, 82-87 (2011).
21. L. Ge, R. F. Li, S. C. He, H. Chen, L. C. Guo, Enhanced grain-boundary conduction in polycrystalline Ce0.8Gd0.2O1.9 by zinc oxide doping: Scavenging of resistive impurities. *Journal of Power Sources* **230**, 161-168 (2013).
22. D. Chen, S. R. Bishop, H. L. Tuller, Praseodymium-cerium oxide thin film cathodes: Study of oxygen reduction reaction kinetics. *J Electroceram* **28**, 62-69 (2012).
23. W. C. Chueh, Y. Hao, W. Jung, S. M. Haile, High electrochemical activity of the oxide phase in model ceria-Pt and ceria-Ni composite anodes. *Nat Mater* **11**, 155-161 (2012).
24. S. P. Jiang, S. H. Chan, A review of anode materials development in solid oxide fuel cells. *J. Mater. Sci.* **39**, 4405-4439 (2004).
25. J. J. Kim, S. R. Bishop, N. J. Thompson, D. Chen, H. L. Tuller, Investigation of Nonstoichiometry in Oxide Thin Films by Simultaneous in Situ Optical Absorption and Chemical Capacitance Measurements: Pr-Doped Ceria, a Case Study. *Chem. Mat.* **26**, 1374-1379 (2014).
26. S. R. Bishop, T. S. Stefanik, H. L. Tuller, Electrical conductivity and defect equilibria of $Pr_{0.1}Ce_{0.9}O_{2-\delta}$. *Phys Chem Chem Phys* **13**, 10165-10173 (2011).
27. H. L. Tuller, S. R. Bishop, Point Defects in Oxides: Tailoring Materials Through Defect Engineering. *Annu Rev Mater Res* **41**, 369-398 (2011).
28. W. Jung, H. L. Tuller, A New Model Describing Solid Oxide Fuel Cell Cathode Kinetics: Model Thin Film SrTi1-xFexO3-d Mixed Conducting Oxides-a Case Study. *Adv Energy Mater* **1**, 1184-1191 (2011).
29. T. Barakat, J. C. Rooke, E. Genty, R. Cousin, S. Siffert, B. L. Su, Gold catalysts in environmental remediation and water-gas shift technologies. *Energ Environ Sci* **6**, 371-391 (2013).
30. R. E. Krebs, *The history and use of our earth's chemical elements : a reference guide*. (Greenwood Press, Westport, Conn., ed. 2nd, 2006), pp. xxv, 422 p.
31. R. J. Chater, S. Carter, J. A. Kilner, B. C. H. Steele, Development of a Novel Sims Technique for Oxygen Self-Diffusion and Surface Exchange Coefficient Measurements in Oxides of High Diffusivity. *Solid State Ion.* **53**, 859-867 (1992).
32. Sean R. Bishop, John Druce, Jae Jin Kim, John A. Kilner, H. L. Tuller, Observation of surface impurities in $Pr_{0.1}Ce_{0.9}O_{2-\delta}$ thin films following optical absorption relaxation measurements. *ECS Transactions* **50**, 35-38 (2013).
33. S. R. Bishop, J. Druce, J. Kilner, T. Ishihara, K. Sasaki, Compensation for oxygen exchange rate limiting impurities on a $Pr_{0.1}Ce_{0.9}O_{2-\delta}$ SOFC electrode materia. *ECS Transactions* **57**, (2013).
34. D. Ivanova, A. Kovalevsky, V. V. Kharton, F. M. B. Marques, Silica-scavenging effects in ceria-based solid electrolytes. *Bol Soc Esp Ceram V* **47**, 201-206 (2008).

35. J. Druce, J. A. Kilner, Improvement of Oxygen Surface Exchange Kinetics for CGO with Surface Treatment. *Journal of The Electrochemical Society* **161**, F99-F104 (2014).
36. J. J. Kim, S. R. Bishop, N. J. Thompson, H. L. Tuller, Investigation of Redox Kinetics by Simultaneous In Situ Optical Absorption Relaxation and Electrode Impedance Measurements: Pr Doped Ceria Thin Films. *ECS Transactions* **57**, 1979-1984 (2013).
37. S. R. Bishop, J. J. Kim, N. Thompson, H. L. Tuller, Probing redox kinetics in Pr doped ceria mixed ionic electronic conducting thin films by in-situ optical absorption measurements *ECS Transactions* **45**, 491-495 (2012).
38. C. Anandan, P. Bera, XPS studies on the interaction of CeO_2 with silicon in magnetron sputtered CeO_2 thin films on Si and Si_3N_4 substrates. *Appl Surf Sci* **283**, 297-303 (2013).
39. E. J. Preisler, O. J. Marsh, R. A. Beach, T. C. McGill, Stability of cerium oxide on silicon studied by x-ray photoelectron spectroscopy. *J Vac Sci Technol B* **19**, 1611-1618 (2001).
40. T. Skala, V. Matolin, Photoemission study of cerium silicate model systems. *Appl Surf Sci* **265**, 817-822 (2013).
41. B. Hirschauer, M. Gothelid, E. Janin, H. Lu, U. O. Karlsson, CeO_2 on Si(111) 7 X 7 and Si(111)-H 1 X 1, an interface study by high-resolution photoelectron spectroscopy. *Appl Surf Sci* **148**, 164-170 (1999).
42. M. Vorokhta, I. Matolinova, M. Dubau, S. Haviar, I. Khalakhan, K. Sevcikova, T. Mori, H. Yoshikawa, V. Matolin, HAXPES study of CeO_x thin film-silicon oxide interface. *Appl Surf Sci* **303**, 46-53 (2014).
43. H. Yamada, T. Shimizu, A. Kurokawa, K. Ishii, E. Suzuki, MOCVD of high-dielectric-constant lanthanum oxide thin films. *Journal of the Electrochemical Society* **150**, G429-G435 (2003).
44. B. Lee, T. J. Park, A. Hande, M. J. Kim, R. M. Wallace, J. Kim, X. Liu, J. H. Yi, H. Li, M. Rousseau, D. Shenai, J. Suydam, Electrical properties of atomic-layer-deposited La_2O_3 films using a novel La formamidinate precursor and ozone. *Microelectron Eng* **86**, 1658-1661 (2009).
45. W. Y. Howng, R. J. Thorn, Investigation of the Electronic-Structure of $La_{1-x}(M_{2+})xCrO_3$, Cr2o3 and La_2O_3 by X-Ray Photoelectron-Spectroscopy. *J. Phys. Chem. Solids* **41**, 75-81 (1980).
46. M. H. Wu, C. H. Cheng, C. S. Lai, T. M. Pan, Structural properties and sensing performance of high-k Sm_2O_3 membrane-based electrolyte-insulator-semiconductor for pH and urea detection. *Sensor Actuat B-Chem* **138**, 221-227 (2009).
47. B. M. Reddy, P. M. Sreekanth, E. P. Reddy, Y. Yamada, Q. A. Xu, H. Sakurai, T. Kobayashi, Surface characterization of La_2O_3-TiO_2 and V_2O_5/La_2O_3-TiO_2 catalysts. *J. Phys. Chem. B* **106**, 5695-5700 (2002).
48. D. Tahir, E. H. Choi, Y. J. Cho, S. K. Oh, H. J. Kang, H. Jin, S. Heo, J. G. Chung, J. C. Lee, S. Tougaard, Electronic and optical properties of La-aluminate dielectric thin films on Si (100). *Surf Interface Anal* **42**, 1566-1569 (2010).
49. W. Jung, H. L. Tuller, Investigation of surface Sr segregation in model thin film solid oxide fuel cell perovskite electrodes. *Energ Environ Sci* **5**, 5370-5378 (2012).
50. Y. Chen, W. Jung, Z. H. Cai, J. J. Kim, H. L. Tuller, B. Yildiz, Impact of Sr segregation on the electronic structure and oxygen reduction activity of $SrTi_{1-x}Fe_xO_3$ surfaces. *Energ Environ Sci* **5**, 7979-7988 (2012).
51. R. Waser, T. Bieger, J. Maier, Determination of Acceptor Concentrations and Energy-Levels

in Oxides Using an Optoelectrochemical Technique. *Solid State Commun* **76**, 1077-1081 (1990).

Chapter 6 Conclusions

In this thesis, multivalent elements (Eu, Mn, Fe, Pr) doped ceria were investigated to develop new MIEC electrode materials for IT or LT-SOFCs.

For Eu-CeO_2, the microstructure and conductivity of grain and grain boundary of 20 mol% Eu-doped ceria ($Ce_{0.8}Eu_{0.2}O_{2-\delta}$) were determined. The conductivity results demonstrate that over the studied pO_2 range Eu has a similar effect on electrical properties as Gd or Sm acceptor dopants in ceria, namely, that Eu shows no evidence for multivalent behavior, rather it appears to be a fixed valent dopant in the fluorite structured ceria, in contrast to prior studies finding multivalency of Eu in perovskite oxides under similar conditions. Based on bulk properties, Eu-CeO_2 is not expected to be a better MIEC electrode material for IT-SOFCs, than, for example, Gd-CeO_2, though the role of Eu on oxygen surface exchange rate has not been explored yet.

For Mn or Fe-CeO_2, Raman spectroscopy and lattice parameter analysis revealed that the solubility limit of Mn or Fe in CeO_2 is lower than 3 mol% for the present preparation conditions and it was not increased by annealing in reducing conditions (humidified H_2 at 1100 °C). Electrical Conductivity of 20mol%Mn-CeO_2 was measured and it is similar with pure ceria. Activation energy calculated from Arrhenius plot of conductivity at lower temperature is 1.1 eV. According the activation energy data versus composition for the different dopants, the Mn solubility can be estimated to be about 0.1~1mol% which also in agreement with XRD and Raman results. Since the solubility of Mn or Fe is low, the reason of for good performance of Mn-Fe-CeO_2 as an anode may be related to high catalytic activity.

On the other hand, by co-doping La, the solubility of Mn was increased and it reaches maximum of 2.9 mol% by doping 10 mol% La into 10 mol% Mn-CeO_2. La, Mn-CeO2 is thus potential MIEC electrode material and need further investigation.

For Pr-CeO_2, which has been reported has good MIEC property and oxygen exchange rate as a cathode material, the durability of oxygen exchange rate is measured by using the opitcal transmission relaxation method (OTR). A significant degradation in kinetics was found during the aging and identified to arise from accumulation of a siliceous phase on the PCO film surface. Deposition of La oxide or Sm oxide on the aged film surface was found to fully recover oxygen exchange kinetics in aged films and a film intentionally coated with siliceous phase. Surface treatments with other oxides (Nb, Al, Ti, and Zn) were not found to recover oxygen exchange kinetics. For (La, Pr)-CeO_2, due to the significant difference in results of three independent measurements, further work is needed to find out the function of La in solution. Long term durability of La treated and La doped PCO film is still need further investigation.

Chapter 7 Future plan

For Mn-CeO_2, TGA results showed a higher solubility limit of Mn than XRD and Raman and conductivity measurements. A TGA measurement on a mixture of CeO_2 and Mn oxide needs to be perform to confirm the accuracy of measurement on Mn-CeO_2. Since Mn solubility in CeO_2 was increased by La doping, (Mn, La)-CeO_2 has the possibility to be an MIEC material, thus it is worth further electrical conductivity investigations.

For OTR measurement of PCO, we found, in some cases reduced long term aging for $La_{0.1}Pr_{0.1}Ce_{0.8}O_{1.95-\delta}$ (LPCO), and the possible catalyst mechanism of La treatment on oxygen exchange kinetics has not been quantified. For the future work, first Si impurity affect need to be quantified by calculating the Si content in air or flow the gas through water or put certain amount of impurity in the reaction chamber. Then, long term measurement of La treated aged PCO film and LPCO need to be confirmed for reproducibility.

This surface treatment analysis may also be extended to cathode materials. For example, Cr poisoning in electrodes is a significant problem for SOFCS. One can determine the Cr affect on oxygen exchange rate of PCO, and deposit, for example, La oxide to find out if it can recover oxygen exchange rate from the Cr poison. Furthermore, we can measure OTR on other materials (i.e. LSCF) and determine the oxygen exchange coefficient on cathode materials.

.

Acknowledgements

I would like to thank my advisor Prof. Sasaki for accepting me into his group and offer me great scientific and financial support. I offer my sincerest gratitude to my supervisor, Prof. S. R. Bishop, who has supported me thoughout my thesis with his patience and knowledge. I could not wish for a better or friendlier supervisor,

I would like to thank professors and fellow group members who teaching me experimental skills and assisted me on my research over the years, especially, S. Taniguchi, N. H. Perry, M. Nishihara, T. Daio, T. Kawabata, T. Oshima, S. Noda, X. Shen, B. Thomas, J. Liu.

I thank Hyodo in Ishihara group helping me with Raman, PLD.

I thank Fukuoka Metal Enterprise Co. Ltd for scholarship support for all eleven years.

I would also like to thank my family for the support they provided me through my entire life and in particular.